ABSTRACT

UNDERSTANDING THE ROLE OF MAGNETIC FIELD EVOLUTION IN THE INITIATION AND DEVELOPMENT OF SOLAR ERUPTIONS

by
Nian Liu

This dissertation aims to understand the initiation and evolution of solar eruptions. The essential science questions to answer include: What is the role of magnetohydrodynamic (MHD) instabilities and magnetic reconnection in triggering and driving eruptions? What are the role of Kink Instability (KI) and Torus Instability (TI) in determining the successful and failed eruptions? What is the thermal behavior of flare precursors in the initiation stage of solar eruptions? Finally, how does the corona magnetic field respond to the flare eruptions? The dissertation mainly includes the following studies.

First, this dissertation presents a multi-instrument study of the two precursor brightenings prior to the M6.5 flare with a focus on their thermal behavior in terms of time variations of temperature (T), electron number density (n), and emission measure (EM). This study quantitatively describes the differences in the thermal parameters at the precursor phase, measured by different instruments operating at different wavelength regimes and for different emission mechanisms. The precursor brightenings in the passbands of Hard X-rays (HXR), extreme ultraviolet (EUV), microwave (MW), and Hα are found to occur within a strong magnetic field region (1200 G) around the flaring polarity inversion line (PIL). Such a small energy release in the lower atmosphere may be related to the onset of the main flare.

Second, a statistical analysis of torus instability (TI) and kink instability (KI) in solar eruptions is presented, in order to improve our understanding of the likelihood of a CME based on the observed TI parameter decay index and KI parameter twist number. It is found that TI plays an important role in distinguishing between

ejective and confined flares, while KI is much less influential. However, TI is not a necessary condition for eruption. Some magnetic flux ropes (MFRs) in the TI-stable regime still manage to break through the strong strapping field and evolve into CMEs. It, therefore, implies that an additional driving mechanism, such as magnetic reconnection, may be involved in eruptions.

Third, a study of the magnetic field evolution of the X5.4 flare with two magnetic field extrapolation methods: Non-linear-force-free field (NLFFF) and Non-force-free field (Non-FFF) extrapolations are included in this dissertation. It is found that this flare is most likely triggered by the tether-cutting reconnection and the subsequent DAI. Clear 3D back-reactions of increasing horizontal magnetic field (B_h) and decreasing inclination angle (Φ) of the magnetic field from the photosphere are presented in both NLFFF and Non-FFF. The back-reaction of the increasing downward Lorentz force (F_z) acting on the photosphere produced by the Non-FFF result spatially correlates with the flare initiating location in the DAI analysis.

Last but not least, a study of analyzing the magnetic field structure of the sunspot light bridges in AR 12371 during the M6.5 flare is included in this dissertation. Analysis of the 3D NLFFF model shows a low-lying 3D magnetic canopy as well as a 3D current system. The most substantial difference between the LBs and umbrae is found in the overall magnetic topology in that the field lines emanating from the two LBs are more twisted than that from the neighboring umbrae.

At the end, this dissertation briefly introduces the SolarDB, a cyberinfrastructure built for flare studies and photospheric vector magnetic field reconstruction taking advantage of machine learning (ML)/ deep learning (DL) tools, and future work about the MHD simulation for solar eruptions.

UNDERSTANDING THE ROLE OF MAGNETIC FIELD EVOLUTION IN THE INITIATION AND DEVELOPMENT OF SOLAR ERUPTIONS

by
Nian Liu

A Dissertation
Submitted to the Faculty of
New Jersey Institute of Technology and
Rutgers, The State University of New Jersey – Newark
in Partial Fulfillment of the Requirements for the Degree of
Doctor of Philosophy in Applied Physics

Department of Physics, NJIT
Department of Physics, Rutgers-Newark

August 2022

APPROVAL PAGE

UNDERSTANDING THE ROLE OF MAGNETIC FIELD EVOLUTION IN THE INITIATION AND DEVELOPMENT OF SOLAR ERUPTIONS

Nian Liu

Dr. Haimin Wang, Dissertation Co-advisor   Date
Distinguished Professor of Physics, NJIT

Dr. Ju Jing, Dissertation Co-advisor   Date
Research Professor of Physics, NJIT

Dr. Alexander G. Kosovichev, Committee Member   Date
Professor of Physics, NJIT

Dr. Jason T. L. Wang, Committee Member   Date
Professor of Computer Science, NJIT

Dr. Neepa Maitra, Committee Member   Date
Professor of Physics, Rutgers-Newark

BIOGRAPHICAL SKETCH

Author: Nian Liu

Degree: Doctor of Philosophy

Date: August 2022

Undergraduate and Graduate Education:

- Doctor of Philosophy in Applied Physics,
  New Jersey Institute of Technology, Newark, NJ, 2022

- Bachelor of Science in Geophysics,
  University of Science and Technology of China, 2016

Major: Applied Physics

Presentations and Publications:

N. Liu, J. Jing, Y. Xu and H. Wang, "Multi-instrument Comparative Study of Temperature, Number Density and Emission Measure during the Precursor Phase of a Solar Flare," *The Astrophysical Journal*, Volume 930, Number 2, Pages 154, 13 May 2022.

J. Jing, C. Liu, J. Lee, H. Ji, N. Liu, Y. Xu, and H. Wang, "Statistical Analysis of Torus and Kink Instabilities in Solar Eruptions," *The Astrophysical Journal*, Volume 864, Number 2, Pages 138, 10 September 2018.

N. Liu, J. Jing, Q. Hu and H. Wang, "The Initiation and Back-reaction of the X5.4 Flare on March 7, 2012," *The Astrophysical Journal*, under review.

H. Jiang, Q. Li, Z. Hu, N. Liu, Y. Abduallah, J. Jing, G. Zhang, Y. Xu, W. Hsu, J. Wang and H. Wang, "Generating Photospheric Vector Magnetograms of Solar Active Regions via Deep Learning," *The Astrophysical Journal*, under review.

J. Jing, N. Liu, J. Lee, Y. Xu, W. Cao and H. Wang, "Characterizing 3D Magnetic Field in Sunspot Light-bridges," *The Astrophysical Journal*, in preparation.

N. Liu, "Magnetic Evolution of the X5.4 Flare on March 7th 2012 and its associated Back-reaction," *The 238th American Astronomical Society Meeting Solar Physics Division* , Virtual, 8 June 2021.

N. Liu, "Multi-instrument Comparative Study of Temperature, Number Density and Emission Measure during the Precursor Phase of a Solar Flare," *The 234th American Astronomical Society Meeting Solar Physics Division* , St. Louis, MO, 9–13 June 2019.

The world is yours, as well as ours, but in the last analysis, it is yours. You young people, full of vigor and vitality, are in the bloom of life, like the Sun at eight or nine in the morning. Our hope is placed on you.

Desheng Li

ACKNOWLEDGMENT

TABLE OF CONTENTS

LIST OF TABLES

LIST OF FIGURES

Figure   **Page**

Figure   **Page**

LIST OF ACRONYMS

AIA	Atmospheric Imaging Assembly
AR	Active Region
BBSO	Big Bear Solar Observatory
CME	Coronal Mass Ejection
CSHKP	Carmichael-Sturrock-Hirayama-Kopp-Pneuman
DAI	Double-Arc Instability
DEM	Diffarential Emission Measure
DL	Deep Learning
EM	Emission Measure
EOVSA	Expanded Owens Valley Solar Array
EUV	Extreme Ultraviolet
GOES	Geostationary Operational Environmental Satellite
GST	Goode Solar Telescope
HMI	Helioseismic and Magnetic Imager
HXR	Hard X-ray
KI	Kink Instability
LB	Light Bridge
LFFF	Linear-force-free Field
LOS	Line-of-sight
MFR	Magnetic Flux Rope
MHD	Magnetohydrodynamics
ML	Machine Learning
MW	Microwave
NLFFF	Non-linear-force-free Field
Non-FFF	Non-force-free Field
NOAA	National Oceanic and Atmospheric Administration

OP	Opposite Polarity
PF	Potential Field
PIL	Polarity Inversion Line
RHESSI	Reuven Ramaty High Energy Solar Spectroscopic Imager
RS	Revered Shear
SDO	Solar Dynamics Observatory
SWPC	Space Weather Prediction Center
SXI	Soft X-ray Imager
SXR	Soft X-ray
TI	Torus Instability
UV	Ultraviolet

CHAPTER 1

INTRODUCTION

A flare is a sudden intense release of the magnetic field energy in the solar atmosphere through radiations and emissions across basically the entire electromagnetic spectrum. The typical magnitude of energy released during a flare is on the order of 10^{27} to 10^{32} ergs[1] per second.

Solar activities like flare eruptions and coronal mass ejections (CME) are the most important influence on space weather. The flare with and without associated CME is called the ejective and the confined flare [89], respectively. Ejective flares could have a much greater influence on the near-earth environment than confined flares. The scope of such influence on earth includes but is not limited to the disruption of electric power systems, the safety of aircraft and satellite operations, stability of telecommunication and navigation systems, etc. Thus, it is important to study under what magnetic field conditions can these solar activities occur and how can we predict such powerful phenomena, i.e., space weather forecasting. However, the initiation mechanism of solar flares and associate CME has been a long-lasting but still not well-understood question in solar physics.

The primary theme in this dissertation is solar flare studies in terms of magnetic field evolution leading and reacting to a solar flare. The standard morphological structure of magnetic fields in solar flares eruptions is the famous Carmichael-Sturrock-Hirayama-Kopp-Pneuman (CSHKP) model [104]. Some of the key features of this model during the impulsive phase include two Hα ribbons on the solar chromosphere, HXR sources on the footpoints and the looptop of the magnetic arcade, and SXR loops connecting the two ribbons. In this model, the reconnection

---

[1]A CGS unit of energy equal to g·cm^2·s^{-2}, 1 erg = 10^{-7} joule

of the magnetic field lines in the solar corona that are usually shown as bright arcades over the polarity inversion line (PIL[2]) is considered to be the fundamental driving mechanism of flare eruption.

Meanwhile, the magnetohydrodynamic (MHD) instabilities are also capable of driving a flare eruption once the magnetic field parameters reach certain critical values in the corresponding MHD instability models. The positive feedback between magnetic field reconnection and MHD instabilities results in continuous energy released from the magnetic field, i.e., initiating a flare.

However, there are still many unsolved questions regarding the magnetic field reconnection configurations and relationships between different MHD instabilities. Besides, many interesting observations during flare eruptions like precursors and light bridges are also important to investigate.

Based on its peak flux of soft X-rays (SXR) measured by the Geostationary Operational Environmental Satellite (GOES), from strongest to weakest, flares are classified as X, M, C, B, and A class. Solar flares usually happen in the NOAA SWPC[3] Active Region (AR) which is characterized as a temporary region on the solar photosphere with a strong and complex magnetic field. They often consist of several sunspots and their number is assigned by the SWPC.

The two major flares in this dissertation are the M6.5 flare in NOAA AR 12371 and the X5.4 flare in AR 11429.

Since the solar flare was first discovered[4] in white light in 1859 using a two-meter-long brass telescope [22], the observing method has been greatly developed. The optical emissions from flares can be observed with ground-based telescopes, e.g., the 1.6 m Goode Solar Telescope (GST) at Big Bear Solar Observatory (BBSO); the

---

[2]The location where the vertical magnetic field on the photosphere changes its polarity.
[3]Space Weather Prediction Center of National Oceanic and Atmospheric Administration
[4]Two scientists, Richard C. Carrington and Richard Hodgson, independently witnessed a large flare when they observing sunspots.

4 m Daniel K. Inouye Solar Telescope (DKIST) at Haleakala Observatory. Microwave (MW), also known as radio, emissions could be detected by large-scale antenna arrays, e.g., the Expanded Owens Valley Solar Array (EOVSA) at Owens Valley Radio Observatory (OVRO); the Karl G. Jansky Very Large Array (VLA) located in central New Mexico.

On the other hand, the observation of ultraviolet (UV) and shorter wavelengths depends on the satellite observatories because the earth's atmosphere blocks most of the UV emissions. In this dissertation, we obtain the hard X-rays (HXR) data from the Reuven Ramaty High Energy Solar Spectroscopic Imager (RHESSI), and the UV/extreme ultraviolet (EUV) emission data is mostly obtained from the Solar Dynamics Observatory's (SDO) Atmospheric Imaging Assembly (AIA) in seven EUV passbands (94Å, 131Å, 171Å, 193Å, 211Å, 304Å, 335Å) and two UV passbands (1600Å, 1700Å). The Helioseismic and Magnetic Imager (HMI) is another instrument on board SDO which provide us with a variety of magnetographs on the photosphere.

The introduction of each type of data and their application are presented in the Section 2. The related concepts of flare initiation studies will be introduced in the following subsections.

1.1 Flare Precursors

The flare precursor brightenings, shown as small-scale emissions in various wavelengths including optical, UV/EUV, SXR, HXR, and MW, have been observed prior to many flares and regarded as a result of the localized magnetic reconnection and the subsequent small-scale energy release. [88, 47, 43]

Although the concept of flare precursors was initially introduced almost 60 years ago [15] and precursor brightenings have been observed in many different wavelengths, such small-scale emissions have thus far not been well understood and characterized. For example, some studies attribute B/C-class flares prior to a major

flare to precursors, while for others, any brightness enhancement observed in the vicinity of and prior to the main flare is considered a precursor, regardless of the wavelengths. The time intervals for this kind of precursor observation are very different, ranging from 25 min [44] to 10 hr [110]. Other studies consider very long periodic pulsations [70, 112] and quasi-periodic pulsations [71, 18] during the pre-flare phase to be precursors. Such kind of precursors usually have periods in the unit of minutes.

Despite the growing literature of precursor studies, especially after the new millennium, a comprehensive comparative study of precursors in multi-wavelength is particularly lacking. For the same event, different data sets may come to inconsistent conclusions. For instance, before an X-class flare, a significant precursor was found in the HXR emission but is completely absent in the MW observation [143]. Such a difference and the underlying physics have not been addressed in previous studies. Part of the difference in the results is due to the varying definitions of precursors.

Statistical studies show that more than half of the precursors are visible in MW emissions within 60 minutes before the associated SXR flare emissions reach their maxima [28]. Some changes in magnetic characteristics of sunspot groups may even occur two days before the main flares [1]. Most of the precursors occur within a distance of about 0.1 diameters of the sunspot group from the site of the major flare [43].

Presumably, precursors may be related to two types of small-scale magnetic structures near the magnetic polarity inversion line (PIL) as demonstrated by the magnetohydrodynamics (MHD) simulation by Kusano et al., 2012 [63]. These two types of magnetic structures are reversed-shear (RS) and opposite-polarity (OP), where OP means the azimuthal orientation of the small-scale injected field compared to the large-scale force-free field is 180°, and RS means such orientation is greater than 180° but less than 360°. Both of which have been tested for their applicability by MHD

simulations [7], and observed before major flares. For example, an RS-type magnetic structure was seen before an X-class flare [8]. Taking advantage of the high-resolution observation of the BBSO/GST, a magnetic channel structure[5] is recognized as the OP-type structure and is found to be associated with the precursor brightenings before an M6.5 flare [126].

The study of precursor brightenings of solar flares holds valuable clues concerning the flare triggering and energy release mechanisms. Wang et al., 2017 [126] studied the M6.5 flare using Hα images and photospheric vector magnetograms obtained by the BBSO/GST, and presented the possible relationship between the precursors and the onset of the main flare in terms of the magnetic field structure evolution. On the other hand, it has been observed in multi-wavelength that most of the energy released in the precursor phase is considered to be thermal [6]. In this dissertation, we focus on the thermal behaviors of the two precursors of the M6.5 flare, using multi-wavelength observation, i.e., AIA/EUV, RHESSI/HXR, GOES/SXR, and EOVSA/MW.

1.2   MHD Instabilities

Generally speaking, during the impulsive phase[6] of a flare, the two processes, MHD instabilities, and magnetic reconnection may work simultaneously in triggering and driving the eruption.

MHD instabilities that are commonly thought to trigger solar eruptions and produce coronal mass ejections (CMEs) include MHD helical kink instability (KI, [9, 118]), MHD torus instability (TI, [61]), and a newly developed Double-arc instability (DAI, [56]) which share the same magnetic field morphology of the tether-cutting reconnection [89].

---

[5]A magnetic channel is an elongated alternating structure of positive and negative polarities.
[6]Impulsive phase refers to the first phase of a solar flare, in which X-radiation rises to a maximum in a few seconds or minutes.

1.2.1 Torus Instability

TI occurs when the strapping magnetic field above a magnetic flux rope (MFR) structure decays with height at a sufficiently fast rate, as quantified by decay index:

$$n \equiv -\frac{\partial log(\mathbf{B}_{ext})}{\partial log(h)} \tag{1.1}$$

where $\mathbf{B}_{ext}$ denotes the external strapping field, usually assumed as the horizontal component of the potential field. Numerical analysis shows that the critical threshold of n is n_{crit}=1.5 [9, 61] beyond which the MFR is unstable due to TI.

1.2.2 Kink Instability

The KI, on the other hand, is expected to lead to the deformation of an MFR when the winding number of magnetic field lines around the MFR axis exceeds 1.25 turns [10, 117]. In this dissertation, we applied the methods of Liu et al., 2016 [81], use the twist number T_w as a proxy of the magnetic twist of MFR:

$$T_w = \int_L \frac{\mu_0 J_{||}}{4\pi|B|} dl \tag{1.2}$$

where the $J_{||}$ is the parallel component of current density along the direction of magnetic field.

1.2.3 Double-arc Instability and Tether-cutting Reconnection

The tether-cutting reconnection is a kind of the magnetic field reconnection config-uration which works as the initiation mechanism of solar flares. It is a widely accepted model for solar eruptions proposed by Moore et al., 2001 [89]. Its scenario is characterized by a "sigmoid-to-arcade" and a "four footpoints to two ribbons" evolution [78, 77], i.e., the reconnection of two sheared arcades leads to the formation of a low-lying shorter loop across the magnetic PIL and a longer MFR connecting the two distant ends of a sigmoid. The tether-cutting reconnection below the newly

formed MFR gradually transforms the shear arcade into the MFR, which eventually becomes unstable due to the attenuated stabilizing effect of the overlying magnetic field.

Recently, DAI is proposed by Ishiguro & Kusano [56], which has the same topology as the tether-cutting reconnection, but the long magnetic loop formed by the tether-cutting reconnection has a double-arc shape. Such a double-arc loop implies an additional upward Lorentz force and is, therefore, more susceptible to instability. DAI occurs when a magnetic parameter κ exceeds a threshold on the order of $\kappa_0 = 0.1$, derived from MHD simulations [56]. The value of κ is defined as:

$$\kappa \equiv T_w \frac{\Phi_{rec}}{\Phi_{tot}} \tag{1.3}$$

where Φ_{rec} and Φ_{tot} are the magnetic flux of the double arc loops and total flux of the external strapping field, respectively.

Furthermore, based on this value, Kusano et al., 2020 [64] developed the κ scheme to pinpoint the onset locations of flares by finding out the minimum circle area with $\kappa \leq \kappa_0$ and critical radius ($r_c \leq 1$ Mm) located on the PIL.

The acquisition of the MHD instability parameters relies on the three-dimensional (3D) coronal magnetic field reconstruction. In this dissertation, we apply extrapolation methods with photospheric magnetic field input, under two kinds of assumptions, the nonlinear force-free field (NLFFF) and the non-force-free field (Non-FFF) which will be introduced in Section 2.1.2 and Section 2.1.3.

In this dissertation, we analyze the role of TI and KI in the statistical study of eruptive and confined flares in Section 3.2. In addition, we examine all the three instabilities in the initiation mechanism of the X5.4 flare using the NLFFF extrapolation results in Section 3.3.1. We also calculate the KI parameter, T_w, as one of the magnetic features of the sunspot light bridges during the M6.5 flare in Section 3.4.

1.3 Back-reaction

The concept of back-reaction due to energy release from the coronal fields is introduced by Hudson et al., 2008 [53] and Fisher et al., 2012 [29]. Based on the simple principle that the abrupt force perturbations during eruptions should be balanced by equal and opposite force perturbations acting on the solar photosphere and interior, Fisher et al., 2012 [29] introduced a practical formulation to calculate the Lorentz force change acting on the solar photosphere through photospheric magnetic measurements. The downward Lorentz force change acting on the photospheric layer and the solar interior after the flare is also predicted so that the photospheric magnetic field becomes more horizontal.

Many previous observations have confirmed such a change on the solar photosphere [108, 128, 127, 123, 125, 40, 95, 111, 131, 132, 130, 96]. However, the value of Lorentz force cannot be properly calculated because the observational vector magnetic field can be only obtained on the photosphere as one layer of data in the two-dimensional (2D) area. The calculation of Lorentz force, on the other hand, requires at least two layers of vector magnetic field input.

A fair approximation of the change of the Lorentz force is obtained by the following equations [29].

$$\delta F_r = \frac{1}{8\pi} \int_{A_{ph}} (\delta B_r^2 - \delta B_h^2) \, dA \tag{1.4}$$

and

$$\delta \mathbf{F}_h = -\frac{1}{4\pi} \int_{A_{ph}} \delta(B_r \mathbf{B}_h) \, dA \tag{1.5}$$

where F_r and $\mathbf{F}_h$ are the radial (vertical) and horizontal component of the Lorentz force change, respectively. A_{ph} is the integration area on the photosphere. B_r and $\mathbf{B}_h$ are the radial (vertical) and horizontal component of the vector magnetic field, respectively.

In Section 3.3.2, we applied both NLFFF and Non-FFF extrapolations to validate the back-reaction theory during the X5.4 flare, both on the photosphere and in the corona. Furthermore, the 3D Lorentz force can be directly calculated in the Non-FFF results.

1.4   Light-Bridges

Sunspot light-bridges (LBs) are intriguing narrow structures across the sunspot umbra, even splitting it into two or multiple parts. They are often seen in the decay phase of sunspots, indicating their imminent disintegration [120], but can also be seen in the formation phase of nascent sunspots [34].

Physically, LBs are conceived to be intrusions of field-free hot plasma into an otherwise stable umbral magnetic field from below [94, 21, 69, 109], with a magneto-convective origin [46, 101, 100, 20]. Based on Parker's hypothetical sketch of the magnetic field over umbral dots [94], Leka et al., 1997 [69] proposes a magnetic canopy structure above the LBs, a field-free cusp structure formed by the magnetic field lines on either side of an LB meeting upon the top of the LB and then being forced to converge into a vertical direction. This physical picture is later illustrated in a numerical simulation based on a radiative MHD model [115].

For a long time, our knowledge of the magnetic field of LBs was mainly limited to their basic characteristics, i.e., weaker magnetic field and more horizontal orientation compared to the nearby umbra [11, 76, 103, 69]. It was not until the advent of high-resolution solar telescopes, such as the Swedish 1 m Solar Telescope (SST) and the GST, that we were able to take a closer look at LBs.

High-resolution observations have made great progress in understanding the thermodynamic properties of LBs. They do consist of a chain of convective cells with hot upflows at the center and cold downflows at the edges, similar to the granules in the quiet-Sun [65, 116, 142, 42]. A strong spatial correlation between electric currents

and elevated temperature is found in most regions of the LB spine suggesting that the chromosphere is heated via resistive Ohmic dissipation [85]. Observations also show that LBs are often associated with recurring dynamic phenomena observed in the upper atmosphere, such as chromospheric jets, ejections, and brightenings, which may be the result of small-scale magnetic reconnection in and around the LBs [105, 13, 84, 116, 102, 141, 114, 72].

Apart from the advances in understanding thermodynamic properties of LBs, the fine-scale magnetic structure of LBs has not been well demonstrated so far, especially their three-dimensional (3D) magnetic structures. As an example, the magnetic canopy above LBs is so taken for granted, but surprisingly, there is not that much direct observational evidence for it. The weaker and more horizontal photospheric magnetic field of LBs mentioned above provides, to some extent, evidence of magnetic canopy structure at the visible surface. Jurcak et al., 2006 [60] report for the first time the stratification of magnetic parameters in three atmospheric layers up to 200 km, retrieved from the spectropolarimetric data with the Stokes inversion based on Response functions (SIR) code. Their results show that the weak magnetic field strength of LBs increases with height, while inclination with respect to the local vertical decreases with height, coinciding with the expected variation of magnetic canopy structure in the vertical direction. Later, Lagg et al., 2014 [65] perform a spatially coupled inversion to retrieve depth-dependent stratified atmospheric parameters, and present a tapered magnetic configuration overarching the upflows on a continuum optical depth ($\log\tau$) scale.

To better represent the 3D magnetic field over LBs, it would be preferable to use a geometric height z scale rather than the $\log\tau$ scale delivered by inversions. However, the conversion between these two scales is not straightforward due to many unresolved issues (e.g., magnetic curvature force, optical corrugation, etc.). Felipe et al., 2016 [27] make a great effort to convert the $\log\tau$ retrieved with SIR code to

a geometrical scale assuming hydrostatic equilibrium, neglecting curvature force and taking the Wilson depression into account, and present the resulting 3D magnetic structure of parts of a sunspot. To the best of our knowledge, this is the most visual picture of the magnetic canopy obtained by observation to date.

In this dissertation, instead of retrieving depth-dependent stratification of the magnetic field with the inversion method, we use the NLFFF models extrapolated from the high-resolution photospheric vector magnetograms of GST to investigate the magnetic structure of LBs at geometric heights with unprecedented detail, see Section 3.4.

1.5   SolarDB

SolarDB (http://nature.njit.edu/solardb/) is a comprehensive resource accessible on the Internet for advancing space weather research purposes. It contains databases gathered from ground-based observatories (e.g., Global H-alpha Network (GHN) and BBSO) and satellite missions (e.g., SDO/HMI and SDO/AIA), tools (e.g., Flare Forecasting System), and computing services. These databases and tools play an important role in analyzing adverse space weather effects and predicting extreme space weather events.

The database involved in this dissertation is the SDO/HMI and SDO/AIA data obtained from the Joint Science Operations Center (JSOC, http://jsoc.stanford.edu/). It includes EUV/UV emission and magnetic field information of 129 significant flares and 60 control group flares.

For each flare event, the vector magnetograms are provided in both the CCD coordinates ($hmi.B$ series) and their remapped coordinates by using Lambert Cylindrical Equal-Area (CEA) projection ($hmi.B\_sharp$ series, see Section 2.1.1 for details), from 24 h before and 6 h after the flare. The flare database also consists of line of sight (LOS) magnetograms, continuum images, and AIA images in all 7

EUV wavelengths and 2 UV wavelengths. For each type of data in each event, the magnetograms and images are provided with a uniform field of view (FOV) focusing on the AR in which the corresponding event happened, and a quick look movie is available.

I contribute significantly to building this database by developing a highly integrated IDL program to download and process the data and make images and movies, with a successful application for nearly 200 solar events, and more than 100,000 hours of data in total.

CHAPTER 2

DATA INFORMATION AND PROCESSING

In this chapter, multi-instrument data applied in three case studies (Section 3.1, Section 3.3 and Section 3.4) and one statistical study (Section 3.2) will be summarized and introduced, together with various data processing methods. Each type of data processing technique may be applied in different studies with different data inputs. For better categorization, the three case studies in Section 3.1, Section 3.3, and Section 3.4 are named the Multi-instrument Precursor Study, the Initiation and Back-reaction Study, and the Light-bridges Study, respectively. At the end of each section in this chapter, a table may be included to present the data type and data processing techniques in each involved study.

2.1 Magnetogram

In this dissertation, the magnetograms are mostly obtained from SDO/HMI through JSOC. We also use high spatial-resolution photospheric magnetograms obtained from the Near InfraRed Imaging Spectropolarimeter (NIRIS) of GST.

2.1.1 Data Information

Typically, HMI provides line-of-sight magnetograms and vector magnetograms on the photosphere with a spatial resolution of $0.''5^1$/pixel, and temporal cadence of 720s. For some large and flare productive ARs, high cadence magnetograms[2] of 90 s or 135 s may be available. The data archive of HMI begins from 00:00 UT on May 1st, 2010.

---

[1] An unit of angle to representing distance on the solar surface. 1'' $\sim$ 725,000 Km
[2] High cadence data retrieved on Oct 22, 2020 at http://jsoc.stanford.edu/data/hmi/highcad/

hmi.B_series data is frequently used for it provides full disk vector magnetograms that decomposed into three segments: azimuth, inclination, and field (magnitude). For high cadence data processing, the "disambig" file might be needed.

hmi.B_sharp_series data is similar to *hmi.B_series* but with data FOV categorized by Spaceweather HMI Active Region Patch (SHARP) algorithm instead of full disk. Besides the segments of vector magnetograms, it also contains other useful information like line-of-sight magnetic fields, continuum intensity, Doppler velocity, etc.

hmi.B_sharp_cea_series one of the *hmi.B_sharp* data series, which provide vector magnetograms remapped to a Lambert Cylindrical Equal-Area (CEA) projection and decomposed into B_{radial}, B_ϕ, and B_θ, representing out of photosphere, westward, and southward component of the vector magnetic field. This type of data is the ideal choice for corona magnetic field restructure inputs.

HMI Active Region Patch (HARP) number[3] is required to download the SHARP data.

GST/NIRIS, equipped with the new infrared detector and the improved Fabry-Perot filter system [80], provides high spatial-resolution photospheric vector magnetograms and continuum images with a pixel scale of $\sim 0.''08$.

NIRIS data is employed to present fine magnetic field structures in the Light-bridges Study. Considering the NIRIS data can be only obtained within a rather small FOV compared to HMI magnetograms, an embedding technique is applied to implant the high-resolution NIRIS images into the HMI images with larger FOV, in the process of coronal magnetic field reconstruction.

---

[3]HARP number to NOAA AR number relation can be found here: http://jsoc.stanford.edu/doc/data/hmi/harpnum_to_noaa/all_harps_with_noaa_ars.txt

2.1.2 Non-linear Force-free Field (NLFFF)

In this dissertation, the NLFFF extrapolation was performed with the weighted optimization method which minimizes a volume integral of both Lorentz force and field divergence [135].

The result of this approach is the solution of vector magnetic fields satisfying the following equations:

$$\mathbf{j} \times \mathbf{B} = \mathbf{0} \tag{2.1}$$

$$\nabla \times \mathbf{B} = \alpha\mathbf{B} \tag{2.2}$$

$$\nabla \cdot \mathbf{B} = 0 \tag{2.3}$$

Equation (2.1) represents the force-free condition, where $\mathbf{j}$ and $\mathbf{B}$ are current density and magnetic field vector. Equation (2.2) represents the non-linear condition, where α is the torsion coefficient that varies according to the position. Equation (2.3) represents the solenoidal condition.

The purpose of minimizing the volume integral of both Lorentz force and field divergence is achieved by minimizing the following quantity within the 3D extrapolated volume.

$$L = \int_V w(x, y, z)[B^{-2}|(\nabla \times \mathbf{B}) \times \mathbf{B}|^2 + |\nabla \cdot \mathbf{B}|^2]dV \tag{2.4}$$

The difference between this **weighted** method from the standard optimization method [133] is that it includes a weighting function $w(x, y, z)$ in the solution of the minimization condition. The value of the weighting function varies from 1 at the bottom boundary containing the vector magnetic field input, to 0 at other boundaries in the computational box. The advantage of this method is, unlike the un-weighted method, it can reconstruct the coronal magnetic field from the bottom boundary data alone, without estimating the side boundary. If the coefficient α in Equation 2.2

remains a constant, the resulting extrapolation yields a much simpler situation called the linear force-free field (LFFF).

The NLFFF extrapolation is only applicable to low plasma β^4 regions where the force-free assumption is justified. A step called preprocessing [137] is used to remove the net force and torque while smoothing the observed photospheric magnetic field. In this way, the NLFFF model can reproduce magnetic fields well in the near-surface region at the expense of spatial resolution.

2.1.3   Non-force-free Field (Non-FFF)

Due to the force-freeness nature of the NLFFF model, it can not be used to examine the 3D distribution of the Lorentz force. Thus, the non-FFF model is applied in the initiation and back-reaction study (see Section 3.3), which allow us to calculate the Lorentz force by its definition (Equation 2.8) in the corona instead of estimating it using photospheric magnetograms (Equation 1.4, 1.5).

The non-FFF extrapolation technique numerically decomposes the coronal magnetic field into three vector components [51, 48]: one potential field (PF, current-free) component and two distinct linear force-free field (LFFF) components

$$\mathbf{B} = \mathbf{B}_1 + \mathbf{B}_2 + \mathbf{B}_p \tag{2.5}$$

with $\nabla \times \mathbf{B}_i = \alpha_i \mathbf{B}_i$, $i = 1,2$, and $\alpha_1 \neq \alpha_2 \neq 0$.

In this case, the summation of these three components is not force-free ($\nabla \times \mathbf{B} \times \mathbf{B} \neq 0$), even though each component itself is force-free. This approach requires two layers of vector magnetic field on the solar surface as inputs. Hu et al., 2008 [49] improved this method by adding a coefficient constant in the potential field term as $c\mathbf{B}_p$ where $c \in [-1, 1]$ with $\mathbf{B}_p$ known so that only one layer of input is required.

---

[4]Plasma parameter β: the ratio of the plasma pressure to the magnetic pressure.

However, it still has limitations on real magnetograph measurements for $c\mathbf{B}_p$ is only a special potential field proportional to the potential field obtained from the input photospheric magnetogram. Therefore, Hu et al., 2010 [50] further improved the algorithm by substituting a corrector sub-field $\mathbf{B}_p = \sum \mathbf{B}_p^{(k)}$, $k = 1, 2, 3...$, through an iteration approach, taking advantage of the fact that the summation of a series of potential fields remains potential. With this approach, only a one-layer photospheric vector magnetogram is used as input without pre-processing.

Obviously, the Non-FFF method provides access to Lorentz force information in the 3D region. According to Hu et al., 2010 [50], the Non-FFF results indicate that the non-vanishing Lorentz force mainly exists in the low corona. In an example in Hu et al., 2010 [50], the Lorentz force decreased to 10% of its photospheric value at the height of ~ 2 Mm.

2.1.4 Magnetic Field Parameters

With the 3D magnetic field data cube produced by NLFFF and Non-FFF extrapolations, a variety of magnetic field parameters are able to be calculated in the 3D region.

Decay index n and Twist number T_w

Two of the most important magnetic parameters related to MHD instabilities, TI and KI, in multiple studies in this dissertation are the decay index (n) and the twist number (T_w), for which expressions are shown in Equations 1.1 and 1.2, respectively. We use the code developed by Liu et al., 2016 [81] to calculate the T_w, defined by the Equation (1.2) [12].

DAI parameter κ

Equation 1.3 shows the theoretical expression of the κ in DAI analysis. However, it is difficult to derive the Φ_{rec} using observational data. Therefore, in the Initiation and Back-reaction Study (see Section 3.3.1), we follow the approach in Muhamad et al., 2018 [90] to calculate the estimated κ value with a critical twist number of T_c, under the assumption that the double-arc loop is formed by reconnection between twisted lines with T_w exceeding the critical threshold (T_c):

$$\kappa_{Tc} = \frac{\int_{\frac{T_w}{T_c} > 1} |T_w| d\phi}{\Phi_{tot}} \tag{2.6}$$

where $d\phi = |B_r| dS$, T_c is the threshold twist number value of the applied field lines in the formula.

To estimate Φ_{tot}, we first select the magnetic field at $|B_z| > 300G$ (indicated by the contours in Figure 3.13e) and extrapolate the field lines from the negative polarity field closer to the MFR. We then include in the calculation the extrapolated field lines that satisfy the following conditions, 1) the other end of the field line lies within the selected field of positive polarity shown by the white contour in Figure 3.13e) the top of the field line exceeds the top of the MFR (~ 10 Mm), and 3) the connecting segment at each end of the field line spans the MFR. This approach is similar to that method used by Muhamad et al., 2017 [91] in their paper, but with more conditions for selecting the field lines.

Current density J

$$\mathbf{J} = \frac{c}{4\pi} \nabla \times \mathbf{B} \tag{2.7}$$

where c is the speed of light, $\mathbf{B}$ is the vector magnetic field.

Lorentz force F

Non-FFF model allows us to calculate the Lorentz force. According to Fisher et al., 2012 [29], the relation of the Lorentz force acting on the solar atmosphere and the solar interior/photosphere, are in the exact same magnitude, but in opposite directions from each other, i.e.,

$$\mathbf{F} = -\frac{1}{4\pi} \int_V (\nabla \times \mathbf{B}) \times \mathbf{B} \, dV \tag{2.8}$$

Magnetic shear angle S

The angle between the magnetic field and the local potential vector field.

$$S = \cos^{-1}\left(\frac{\vec{\mathbf{B}} \cdot \vec{\mathbf{B}}_p}{B \cdot B_p}\right) \tag{2.9}$$

where $\mathbf{B}$ and $\mathbf{B}_p$ are the magnetic field vector and the local potential field vector, respectively.

Magnetic field inclination angle Φ

The angle between the magnetic field and the solar surface plane.

$$\Phi = arctan\left(\frac{B_z}{B_h}\right) \tag{2.10}$$

where B_z and B_h are the vertical and horizontal components of the magnetic field, respectively.

Magnetic free energy E_{free}

$$E_{free} = \int_V \frac{B^2}{8\pi} \, dV - \int_V \frac{B_p^2}{8\pi} \, dV \tag{2.11}$$

where B and B_p are the magnitudes of magnetic field and the local potential field, respectively.

2.1.5 Summary

The following table summarizes the magnetic field data types, extrapolation methods, and magnetic field parameters involved in each study.

Table 2.1 Magnetograms and Methods

Fig	Source	Res	Size	Methods	Parameters
3.1-3.5	HMI	1"	$L_x \times L_y \times 200"$ ^{a}	NLFFF, PF	n, T_w
3.7	HMI	0".5	$420" \times 224" \times 224"$	NLFFF	B_{tot}
3.12	HMI	1"	$400" \times 400" \times 400"$	NLFFF, Non-FFF	B_x, B_y, B_z
3.13	HMI	1"	$200" \times 200" \times 200"$	NLFFF	$|J|$, n, T_w, κ_{T_c}
3.14	HMI	0".5	$200" \times 200" \times 200"$	NLFFF	T_w
3.15	HMI	1"	$200" \times 200" \times 200"$	NLFFF, Non-FFF	B_h
3.16	HMI	1"	$200" \times 200" \times 200"$	Non-FFF	F_z
3.17	HMI	1"	$200" \times 200" \times 200"$	NLFFF, Non-FFF	F_z, B_h, Φ
3.18-3.20	NIRIS	0".078	$50" \times 50" \times 130"$	NLFFF	S, B_h, Φ
3.21-3.22	NIRIS	0".2	$102" \times 102" \times 102"$	NLFFF	T_w

---

^{a}The L_x and L_y of the 3D computational domain vary from case to case according to ARs's size to cover not only the major portion of ARs but also the plage regions surrounding the ARs in 38 events in the statistical study.

2.2 Ultraviolet(UV)/Extreme Ultraviolet (EUV)

The UV/EUV emission data is mainly obtained from the SDO/AIA through JSOC. There are seven EUV channels and two UV channels that image the different regions of the solar atmosphere with different typical temperatures of the hot plasma from several thousand Kelvin to 20 MK[5]. Table 2.2 summarize the AIA EUV/UV channels and their operation regions and typical temperatures.

Table 2.2 SDO/AIA EUV/UV Spectral Information

Wavelength (Å)	Primary role, ion(s)	Region of the Sun's atmosphere	Temperature (log T[K])
94	Fe xviii	Flaring regions	6.8
131	Fe xx, xxiii	Flaring regions	7.0, 7.2
171	Fe ix	Quiet corona	5.8
193	Fe xii, xxiv	Corona and hot flare plasma	6.1, 7.3
211	Fe xiv	Active region corona	6.3
304	He ii	Chromosphere	4.7
335	Fe xvi	Active region corona	6.4
1600	Continuum, C iv	Upper photosphere	5.0
1700	Continuum	Photosphere	3.7

2.2.1 EUV/UV Image

The AIA emission images in different channels show energetic particle distribution that strongly correlates to magnetic field morphology during a flare. Because the main source of EUV emissions during a flare is thermal bremsstrahlung [16, 52] and high energy thermal electrons are mostly distributed along the magnetic field lines in the corona [104]. Thus, AIA images could be used as the perfect reference to test

---

[5]Million Kelvin

the results of 3D magnetic field extrapolation models. Furthermore, by observing the AIA movies in multi-wavelength, we can picture the overall situation of a flare in terms of its energy release process and magnetic field evolution.

In the Initiation and Back-reaction Study, we test the fidelity of the NLFFF and Non-FFF extrapolation by comparing the visualized 3D magnetic field with AIA/EUV 193Å images before and after the flare, see Figure 3.12. The region of focus of the 193Å channel is both corona and the hot flare plasma structures that could show the magnetic field lines with high-temperature signature, which is helpful to identify the highly twisted MFR before the flare. Similar observations may be also captured by the channel 131Å, 171Å, or 211Å.

On the other hand, AIA/EUV 304Å channel mostly focuses on the solar chromosphere. It provides more thermal structures close to the solar surface. In Figure 3.13 and 3.14, the brightenings displayed on EUV 304Å images at the beginning of the X5.4 flare clearly show the MFRs footpoints of the tether-cutting reconnection. Practically speaking, we used those brightening areas on AIA 304Å images as the guidance location when finding the highly twisted MFRs. Furthermore, the EUV 304Å movie clearly shows the evolution of how flare ribbons formed from four separate MFR footpoints (see more detail in Section 3.3.1).

Two UV channels (1600Å, and 1700Å) focused on the solar photosphere region could have similar observations with EUV 304Å.

2.2.2   DEM Analysis

Among seven EUV channels of AIA, six of them are in different states of ionized Fe atom, see Table 2.2. They map the temperature structure of the solar corona from 1 MK to above the 20 MK range. The DEM analysis is a technique to produce the differential emission measure at different temperature levels using AIA/EUV emission maps.

In the multi-instrument precursor study, since most of the energy released in the precursor phase is considered to be thermal [6], we performed the DEM analysis for the two precursors prior to the M6.5 flare, using level 1.5 data of AIA/EUV passbands, i.e., 94, 131, 171, 193, 211, and 335Å. Using the sparse inversion method of Cheung et al., 2015 [19], the DEM solutions were obtained in the course of the precursors (17–18 UT) at a cadence of 48 s. DEM maps were obtained from inversion on a pixel-by-pixel basis on a temperature grid with log T = 5.7, 5.8, 5.9 ... 7.6, 7.7 [58] with the spatial resolution of 0".6 per pixel.

Three thermal parameters are calculated using the DEM analysis results: temperature (T), number density (n), and the emission measure (EM). To compare with the GOES and RHESSI results in this study, the EM is defined as the volume-integrated total emission measure in the units of cm^{-3}.

At each pixel i, T and EM are calculated as:

$$\mathrm{T}_i = \frac{\sum_t \mathrm{T}_{t,i} \cdot \mathrm{DEM}_{t,i}}{\sum_t \mathrm{DEM}_{t,i}} \tag{2.12}$$

$$\mathrm{EM}_i = A_i \cdot \sum_t \mathrm{DEM}_{t,i} \tag{2.13}$$

where subscripts t and i represent each temperature grid and each pixel, respectively, and A_i is the area of the spatial sampling.

At each pixel i, n is defined as:

$$n_i = \sqrt{\frac{\sum_t \mathrm{DEM}_{t,i}}{\mathrm{L}}} \tag{2.14}$$

where L is the length of plasma along the line of sight that contributes to the emission over the brightening strip. The brightening strip is a slender area that displays clear emissions in multiwavelengths, including AIA EUV and Hα, during the precursor phase.

Since L is not accessible from observation, the value of L is represented by the emission width (D). We assume that the emissions are isotropic, thus the cross-sectional width of the plasma measured in the x–y plane could represent the plasma length along the line of sight (i.e., $L \sim D$). The detailed steps are as follows.

At each time, we performed 1D Gaussian fittings to the temperature distribution along a series of cross-sectional cuts (the red lines in each panel of Figure 3.7 constitute one example). The Gaussian FWHM for each fitting is a simple representation of the cross-sectional width of the plasma, and its average, weighted by its fitted peak DEM value, was defined as D, which was used to estimate the length of the plasma along the line of sight. It was found in this case that the value of D lies in a range of 5"–10". AIA DEM uncertainties are estimated using the data-to-noise ratio[6], where the uncertainty of length of the plasma (L) is estimated as σ in the Gaussian fitting.

2.3   Soft and Hard X-rays

The SXR and HXR emissions and images are frequently used in flare studies. In the CSHKP model [104], HXR emission is mostly coming from the footpoints and the looptop of the magnetic arcade, while SXR loops connect HXR sources. In this dissertation, GOES/SXR profiles are presented to show the time evolution of precursors (Fig 3.6) and flares (Fig 3.15-3.17). The SXR and HXR imaging and HXR spectra analysis is applied in the Multi-instrument Precorsor Study and presented in the following subsections.

2.3.1   GOES and RHESSI Imaging

In the Multi-instrument Precursor Study, the SXR images are obtained from GOES 15 Solar X-ray Imager (SXI, [45]; [97]) at the peak times of the two precursors of the M6.5 flare (Fig 3.7).

---

[6]https://www.lmsal.com/~cheung/AIA/tutorial_dem/sparse_exercise1.pro

The HXR imaging technique is applied with RHESSI [74, 75] measurements of photon flux in HXR produced by high energy electrons via bremsstrahlung. The best pixel resolution of RHESSI synthesis maps is about 2.3" [73]. In principle, a two-second time interval (half rotation of the rotational modulation collimators carried on RHESSI) provides enough Fourier components for image reconstruction. This can be changed according to the photon count rate in practice.

In the Multi-instrument Precursor Study, Fig 3.6 and 3.7, the CLEAN algorithm [55] was used in the HXR imaging with front detectors 3-8. The total FOV was set to 128" × 128", with a pixel size of 1".

2.3.2 Spectra Analysis (GOSE & OSPEX)

GOSE GUI In the Multi-instrument Precursor Study, the time profiles of T and EM computed from GOES SXR measurements can be directly obtained from the GOSE GUI. The essential ideas underlying the computation have been described by Thomas et al., 1985 [113], (see Equations 1-8).

The X-ray values, B_i, depend on EM and detector responses, b_i:

$$B_i = \text{EM} \cdot b_i(\text{T}) \tag{2.15}$$

(i=4 denotes the 0.5 to 4 Å detector and i=8 the 1 to 8 Å detector). Briefly speaking, assuming the entire plasma volume to be isothermal, the temperature equals to the theoretical value which could produce the same ratio of response of two detectors:

$$R(\text{T}) = B_4/B_8 = b_4(\text{T})/b_8(\text{T}) \tag{2.16}$$

The ratio R is only a function of T. Then the EM could be calculated simultaneously by taking X-ray flux measurements and detector's response ratio into account for a certain temperature:

$$\text{EM} = B_4/b_4(\text{T}) = B_8/b_8(\text{T}) \tag{2.17}$$

These formulae were updated by White et al., 2005 [134] in order to modify temperature measurements in hot flare ($\sim$ 35 MK) condition. The advantage of this method is that only a simple analytic curve fitting is required, and hence the uncertainties are small in a vast temperature range (within 2% of temperature and 5% of EM between 5 and 30 million degrees, in accordance with the expressions to determine T and EM from GOES measurements [113]). The disadvantage, on the other hand, is that its accuracy will be diminished if more than one AR is present on the solar disk.

In fact, there were four ARs on the solar disk during the M6.5 precursor period. AR 12371 is the only AR near the center of the solar disk, while the other three were very close to the west limb. Except for this flare, no other flares have been found within 10 hours before and after this one, according to NOAA SWPC's report. Therefore, we assume that the flare emission in AR 12371 is dominant in the GOES SXR measurements.

OSPEX GUI In the Multi-instrument Precursor Study, we chose an empirically binning code (#14) provided by the RHESSI GUI to perform HXR spectra analysis to produce T and EM profiles.

The spectral resolution varies at different energy ranges, from 1 keV resolution at 3 keV level to 5 keV resolution at 5 MeV level. The spectra in different time intervals can be fitted with various emission models.

In this study, the HXR spectra are fitted using the Variable Thermal Model (vth) and the 2nd version of Thick Target Bremsstrahlung with Independent Normalization Model ($thick2\_vnorm$). Meanwhile, $albedo$ is included for correcting for albedo and $pileup\_mod$ is also applied to add pileup effects to the models.

The background of HXR spectral fitting was selected carefully. For energy ranges of 6-25 keV, we took the background before the first precursor and considered

it to be constant during the flare. However, for energy ranges greater than 25 keV, the HXR emissions of precursors are not so significant compared to the fluctuation of the background. The emissions due to the precursors usually appear as several clear but transient spikes in the HXR flux profile, and they should be separated from the changing background. In this case, the background time was selected during the whole flaring time except for the spikes, and the interpolated count rates were used as the background.

The physical parameters, such as EM and T, of the thermal components, are obtained from the vth model. The uncertainties of RHESSI are estimated using Chi-square (χ^2) test in spectra fittings.

In the process of fitting the HXR spectrum, we noticed that the thermal component (vth) dominates under 20 keV in the vast majority of the fitting time intervals, specifically, in almost all cases of the first precursor and more than half cases of the second precursor. During the precursor phase, however, the maximum flux counts of the non-thermal component continuously increased, and finally, the non-thermal emission peaked at 17:58UT [126], which is 15 minutes after the second precursor. Two examples of the fitting results of RHESSI photon counts and normalized residuals are shown in Figure 2.1.

2.4   Microwave

In this dissertation, the MW data comes from the expanded Owens Valley Solar Array (EOVSA; [35, 54, 37]). EOVSA is a solar-dedicated MW imaging array operating in the frequency range of 1-18 GHz.

2.4.1   Emission Mechanism and Spectrum Fitting

In the Multi-instrument Precursor Study, the sequential spectral fit [36] is performed by combining gyrosynchrotron emission and free-free emission which are responsible for the lower and higher frequencies, respectively.
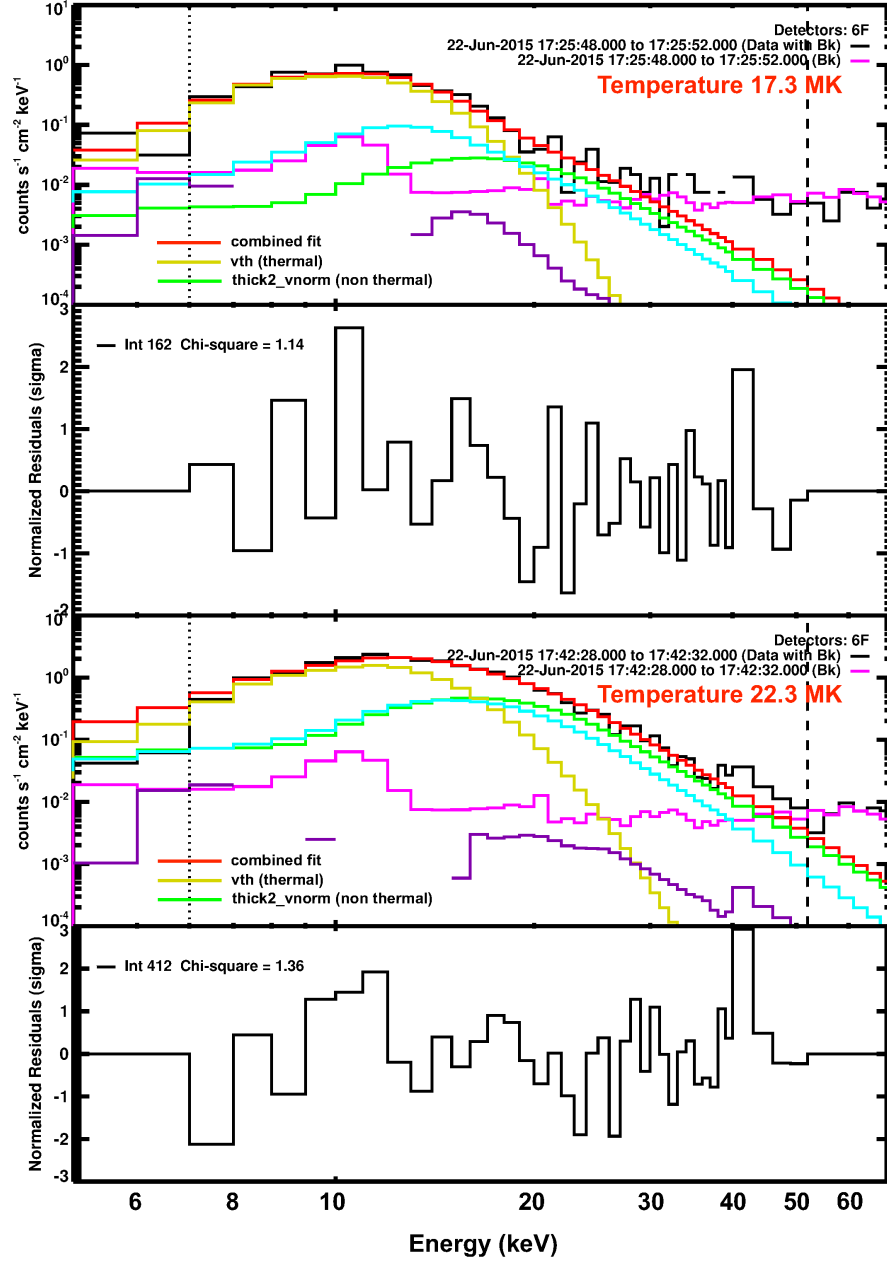
Figure 2.1 Spectral fitting results of RHESSI HXR in photon counts (black) and normalized residuals at two precursor peak times. The yellow, green and red lines in each panel show the modeling results of Variable Thermal Modes (*vth*), Non-thermal Modes (*thick2_vnorm*), and combined fitting results, respectively. The pink lines indicate the background values. The dashed lines mark the energy ranges during the fittings. The cyan and purple lines show the *albedo* and *pileup_mod* corrections, respectively.

The fast gyrosynchrotron codes [31, 32, 36] were applied to quantitatively define the gyrosynchrotron source function, which is designed for both isotropic and anisotropic electron distributions. The uncertainties are estimated using Chi-square (χ^2) test in spectra fittings.

An important assumption of uniform emission source is made to perform the sequential spectral fit. Although the broadband MW spectrum during the main flare indicates the source is spatially non-uniformed, at the precursor phase, the spectral line was fitted with a quasi-uniform source because reasonably narrow spectra are observed during the precursor phase [126]. The size of the emission source is estimated as the depth of 10" and area of 10"×30", based on the observation of the GST Hα image.

By performing such a fitting for a thermal source, three free thermal parameters including n, T, and magnetic field strength (B) are derived [93]. As a follow-up study to Wang et al., 2017 [126], the Multi-instrument Precursor Study uses the same EOVSA MW data analysis results. The detailed methodology is described in Fleishman et al., 2015 [33].

2.4.2   Thermal Condition Determination

In the Multi-instrument Precursor Study, we use the same MW analysis results as in Wang et al., 2017 [126] which conclude that MW emission is quasi-thermal. According to Livadiotis et al., 2012 [83] and Fleishman et al., 2015 [33], 1.5< κ <2.5: non-thermal region; 2.5< κ <20: near thermal equilibrium region, and κ >20, thermal region. In this study, the index of κ distribution during the two precursor periods is mainly in the near thermal equilibrium region. Therefore, the MW of the precursors is considered to be quasi-thermal.

2.5 Observation from the BBSO

The BBSO is equipped with a high-order adaptive optics (AO)-corrected GST with multiple post-focus instrumentations, and an H-alpha full-disk imager which is one of the six institutes of the Global H-Alpha Network, i.e., GHN.

2.5.1 High Resolution Images

The BBSO/GST provides exceptionally high-resolution observations of the Sun in multi wavelengths. It consists of a broadband filter imager (BFI); visible imaging spectrometer (VIS); near-infrared imaging spectropolarimeter (NIRIS); fast-imaging solar spectrograph (FISS); and a cryogenic infrared spectrograph (Cyra).

The following Table 2.3 summarize the different high-resolution GST data applied in each figure/study.

Table 2.3 GST High Resolution Data

Fig	Instrument	Passbands (Å)	FOV(")	Res ("/pixel)
3.6, 3.7	VIS	Hα	70	0.034
3.18	BFI	TiO (7057)	70	0.034
3.19, 3.20	NIRIS	Fe I, He I	85	0.083

2.5.2 Full Disk Hα

The BBSO full-disk Hα images are produced by the Hα full-disk patrol telescope with a 10 cm aperture refractor. The image was taken from local time of $\sim$ 9 AM (16:00 UT) in the morning to 3 PM (22:00 UT) with a cadence of $\sim$ 30 minutes on an observing day.

The detector size is 2048 $\times$ 2048 pixel, 12-bit, for a spatial scale of about 1"/pixel. There are two types of images: "fl" and "fr". "fl" means the full disk image

with dark area subtracted and corrected by the flat-field taken at around the local noon time. "fr" means the full disk image with limb darkening subtracted, which caused by the low emission intensity in the limb area.

The full-disk Hα images are applied in the cooperative study of generating photospheric vector magnetograms of solar active regions via deep learning. Please see Section 3.5.2 for detailed information.

CHAPTER 3

RESEARCH PROJECTS

3.1 Statistical Study: KI and TI in Solar Eruptions

The motivation of this study is to observationally test the laboratory result of Myers et al., 2015 [92], which is the Sun-like line-tied MFRs reveal four distinct eruption regimes which are readily distinguished by the TI and KI parameters. Figure 2 in Myers et al., 2015 [92] shows the four regimes MFRs are either eruptive, stable, failed kink (i.e., torus-stable MFRs that exceed the kink threshold fail to erupt), or failed torus (i.e., kink-stable MFRs that exceed the torus threshold fail to erupt).

In this study, we present the TI vs. KI parameter diagram, established from a statistical study using solar observations together with the coronal field extrapolation techniques. The goal of this study is to improve our understanding of the requirements for a solar eruption: what the trigger/driver mechanisms might be, and what, if any, onset criteria must be reached.

3.1.1 Sample Selection

We examined NOAA GOES soft X-ray (SXR) flare reports to search for major flares (stronger than GOES class M5 in general) that occurred within 45° of the disk center over a seven-year period from January 2011 to December 2017. Due to the small sample size of confined flares, we relaxed the SXR class requirement from M5 to M4 for confined flares. To avoid the over-representation of a certain flare-productive AR, at most two flares per AR were included in the samples, the one of the greatest SXR magnitude, and the one nearest to the disk center.

For each flare, its CME association was determined by reference to the *LASCO* CME catalog [39]. We regarded a flare as ejective if the following criteria are fulfilled: (1) the CME onset time at $R_\odot$ extrapolated backward from the CME heigh-time

profile reasonably agrees with the flare onset time; and (2) the position angle of the CME agrees with the quadrant on the Sun in which the flare occurred. When a flare-CME association is identified, we also refer to the *LASCO* CME catalog for the CME kinetic energy and use it as a CME parameter [122]. We then excluded those ejective flares from the samples if their associated CMEs are neither halo nor partial-halo, because the other types (for example, a jet-type) of CMEs may not be compatible with an MFR topology. We regarded a flare as confined if there are no CMEs in temporal and spatial proximity as described above.

The sample selection requirements led us to a total of 38 flares (26 ejective and 12 confined) from 27 different ARs. The properties of the flares can be found in the Appendix. The NLFFF (see Section 2.1.2) extrapolations were performed to calculate these magnetic field parameters.

3.1.2 Results

Figure 3.3 shows the scatter diagram of TI parameters n vs. KI parameters T_w for the 38 flares. The black symbols represent the confined flares and the rest, ejective flares. For ejective flares, the color is assigned according to the associated CME's kinetic energy. At a glance, our result does not clearly show the four distinct eruption regimes found in the laboratory experiment (Figure 2 in Myers et al., 2015). It is partly due to the fact that the confined and ejective flares are not clearly distinguished in terms of T_w. Instead, we see the clustering of the confined CMEless flares in the lower part of the diagram ($0.2 \lesssim \mathrm{n} \lesssim 0.7$), while the ejective flares spread out over most of the n range ($0.2 \lesssim \mathrm{n} \lesssim 1.6$). Note that the 12 flares with $n \gtrsim 0.8$ are all ejective, in which sense we can regard this as a sufficient condition for CME. However, not all flares of $n \lesssim 0.8$ are confined. Only 12 out of the 26 flares with $n \lesssim 0.8$ are confined and the rest 14 flares are ejective. Thus the criterion, $n > n_{\mathrm{crit}} \simeq 0.8$ found here is not a necessary condition for CME. Note also that this value of $n_{\mathrm{crit}} \simeq 0.8$ found
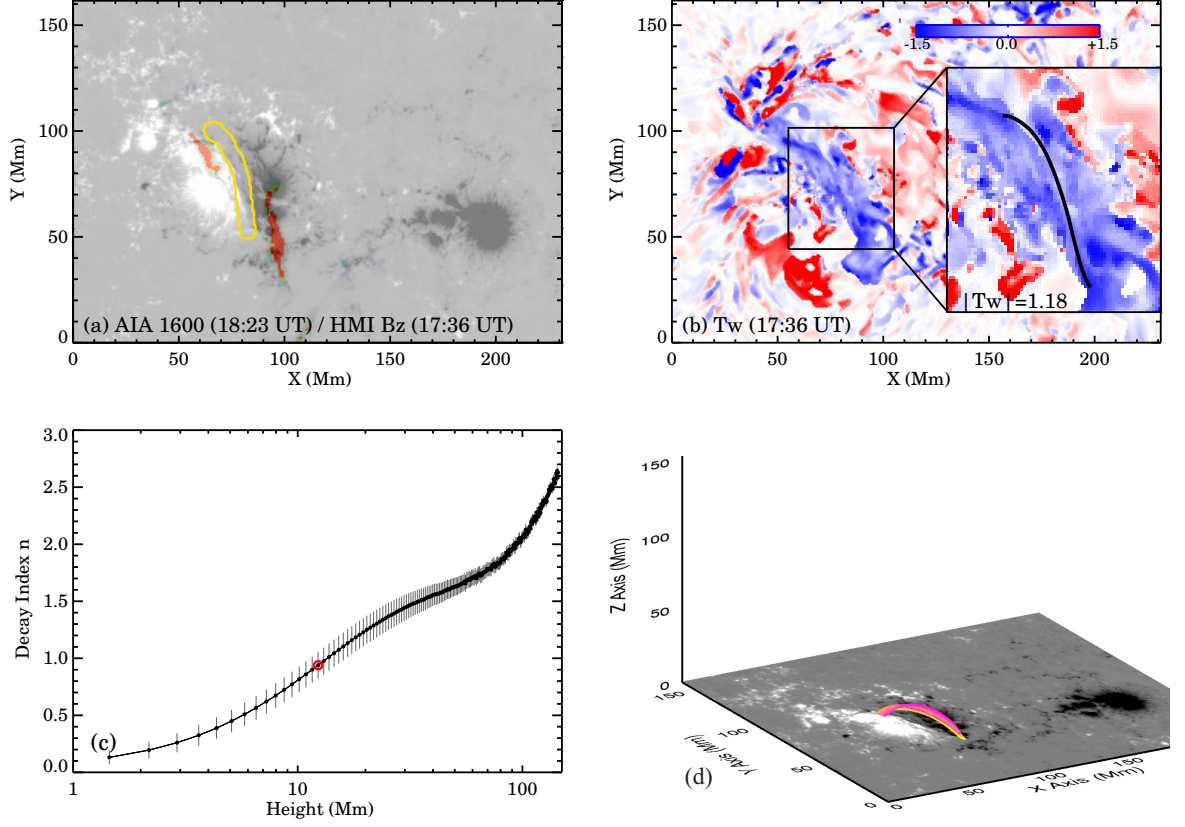
Figure 3.1 The magnetic field of the eruptive M6.5 flare (SOL2015-06-22T18:23) of AR 12371. (a) A blend of an AIA UV 1600Å image at the flare peak time with the pre-flare HMI vector magnetogram B_z, superimposed with the yellow contours of the flaring polarity inversion line (FPIL) mask. Both AIA and HMI maps are de-rotated to a reference pre-flare time (17:36 UT in this case) and re-mapped with the CEA projection. (b) The twist number T_w map derived from the NLFF field, scaled between $-/+1.5$ (blue/red). The rectangle enclosing the flaring core region is zoomed in and displayed in the inset. The superimposed black line shows a representative field line of the MFR, whose $|T_w|$ is annotated. (c) The height profile of decay index n above the FPIL region derived from the potential field model. The error bars indicate $\pm 1\sigma$ spread, evaluated from 908 profiles in FPIL region in this case. The red circle marks the data point at h_{apex}. (d) a 3D perspective of the MFR extrapolated from the NLFFF.
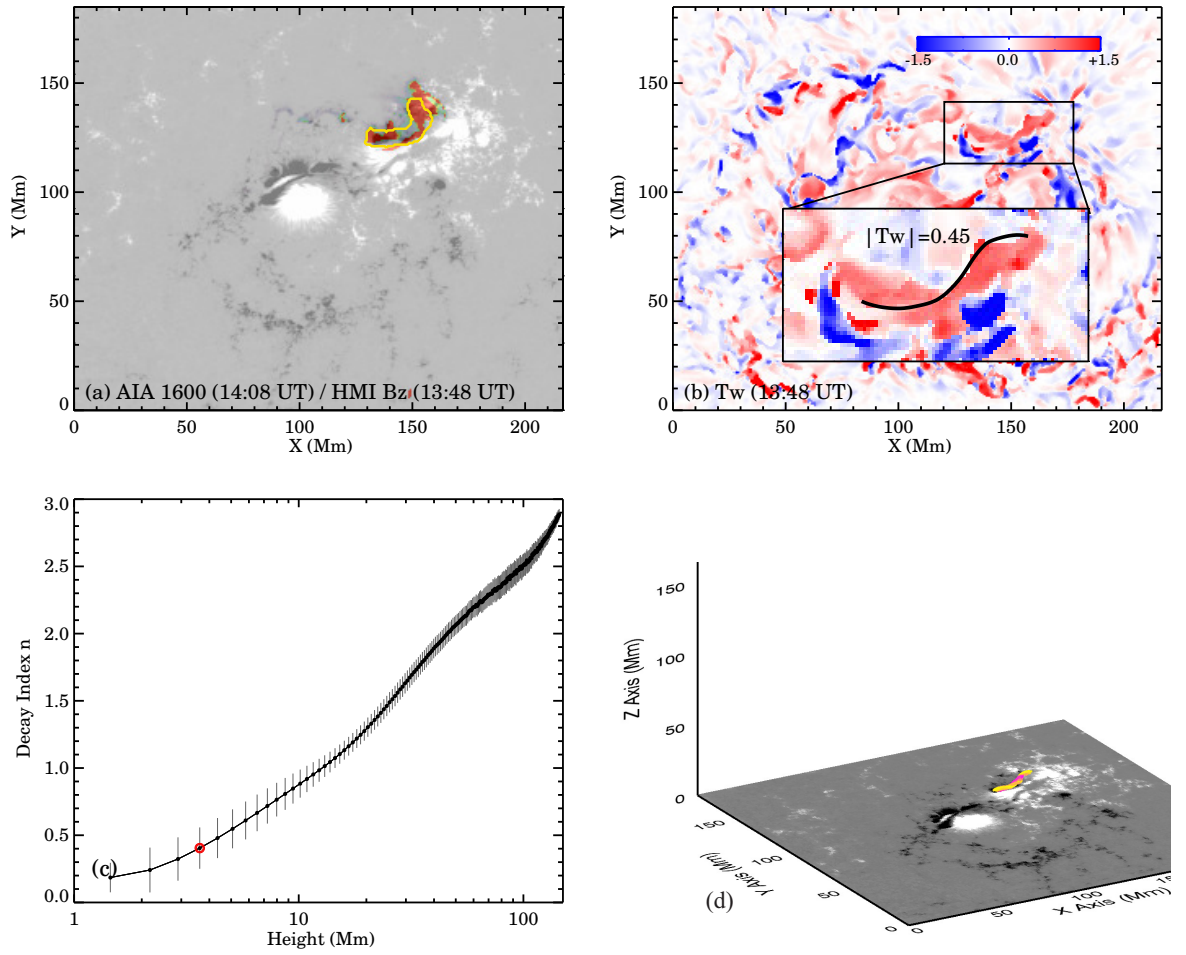
Figure 3.2 The magnetic field of the confined M4.2 flare (SOL2015-03-12T14:08) of AR 12297. Same layout as Figure 3.1
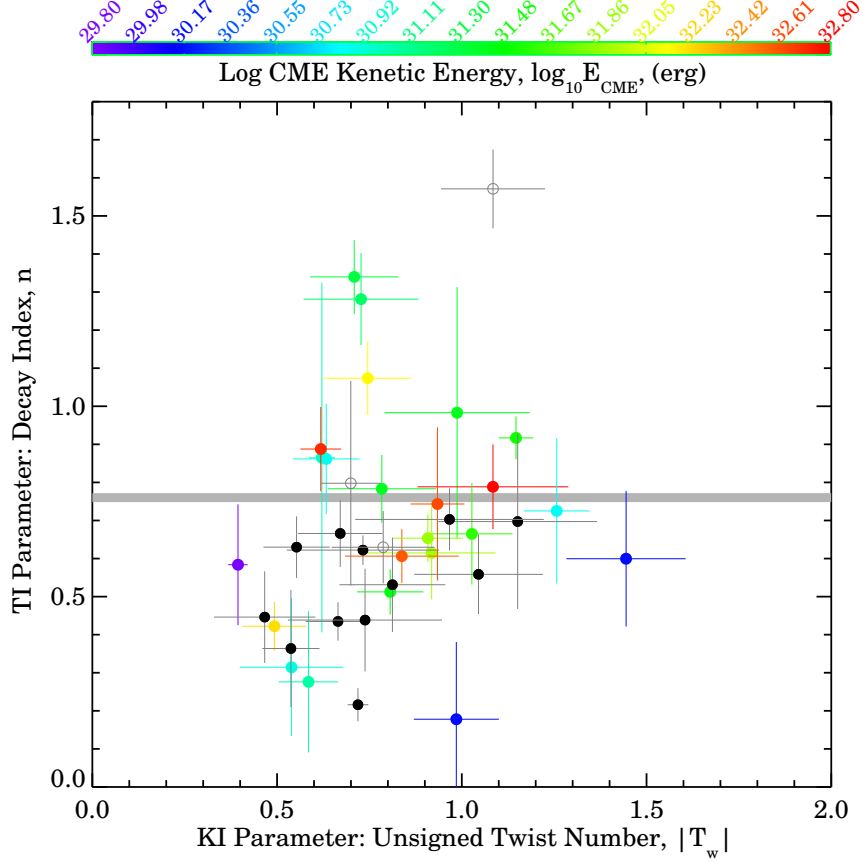
Figure 3.3 Scatter diagram of TI pararameter n vs. KI parameter $|T_w|$. Black and colored symbols correspond to the confined and ejective flares, respectively. For ejective flares, the color is assigned according to the associated CME's kinetic energy, indicated by the color code. Three uncolored hollow symbols represent the three ejective flares in the absence of E_{CME} information. The error bars indicate $\pm 1\sigma$ spread. The horizontal grey line is drawn to illustrate $n_{\mathrm{crit}} \simeq 0.8$.

here is much lower than those typically cited in other solar studies ($n_{\mathrm{crit}} \simeq 1.1 - 1.3$ in Demoulin et al., 2010 [24], for instance), although it agrees well with the critical decay index found in the laboratory experiment performed by Myers et al., 2015 [92]. We presume that the difference arises from the fact that the decay indices were often evaluated for large loops (typically in the height range of $42 - 105$ Mm) in the previous solar studies whereas the MFRs with lower heights are included in the present statistical study. Based on the experimentally measured TI vs. KI parameter diagram, Myers et al., 2015 [92] reports a previously unknown instability regime −− failed torus. The "failed torus" events occur when the guide magnetic field interacts

with electric currents in the MFR to produce a dynamic tension force that brakes the ascension in the torus-unstable region. Our limited samples, however, do not show the presence of this regime. Instead, all the MFRs that exceed a certain torus threshold, $\sim$0.7 in our cases, are developing into CMEs. Presumably, the dynamic tension force in solar cases is too weak to halt eruptions.

The top panels of Figure 3.4 show the histograms of $|T_w|$, n, and E_{free} for both ejective and confined flares. To investigate the MFR geometry as a possible factor for the eruptiveness, we also compared the histograms of h_{apex}, distance d between the MFR footpoints, and h_{apex}/d for ejective and confined flares in the bottom panels of Figure 3.4. For a quantitative comparison between the ejective and confined samples, we performed the Student's t-test to determine the t-statistic (t; a ratio of the difference between two groups to the difference within the groups) and its significance (α; the probability that the results occurred by random chance) for each of the parameters. Briefly speaking, the larger the t-statistic, the more difference there is between the two groups; The lower the significance, the more confident one can replicate the results. As one might expect, the most appreciable segregation between the two groups is in the histograms of n with t=2.337 and α=0.025. That is, the null hypothesis (i.e., there is no difference in mean n between the ejective and confined flares) can be rejected at the 100(1-α)%= 97.5% level of confidence. By comparison, the role of T_w in distinguishing between ejective and confined groups is questionable (t=0.995 and α=0.32). Based on this result, we conclude that the TI rather than the KI plays a more important role in differentiating between the ejective and the confined flares.

To illustrate the relationship between the MFR geometry and the strapping effect, Figure 3.5 shows the scatter diagrams of (a) h_{apex} vs. d, (b) n vs. d, (c) n vs. h_{apex}, and (d) n vs. h_{apex}/d. The linear Pearson correlation coefficient (CC) and the probability of obtaining a certain CC by chance (P_{CC}) are given in each panel. We see
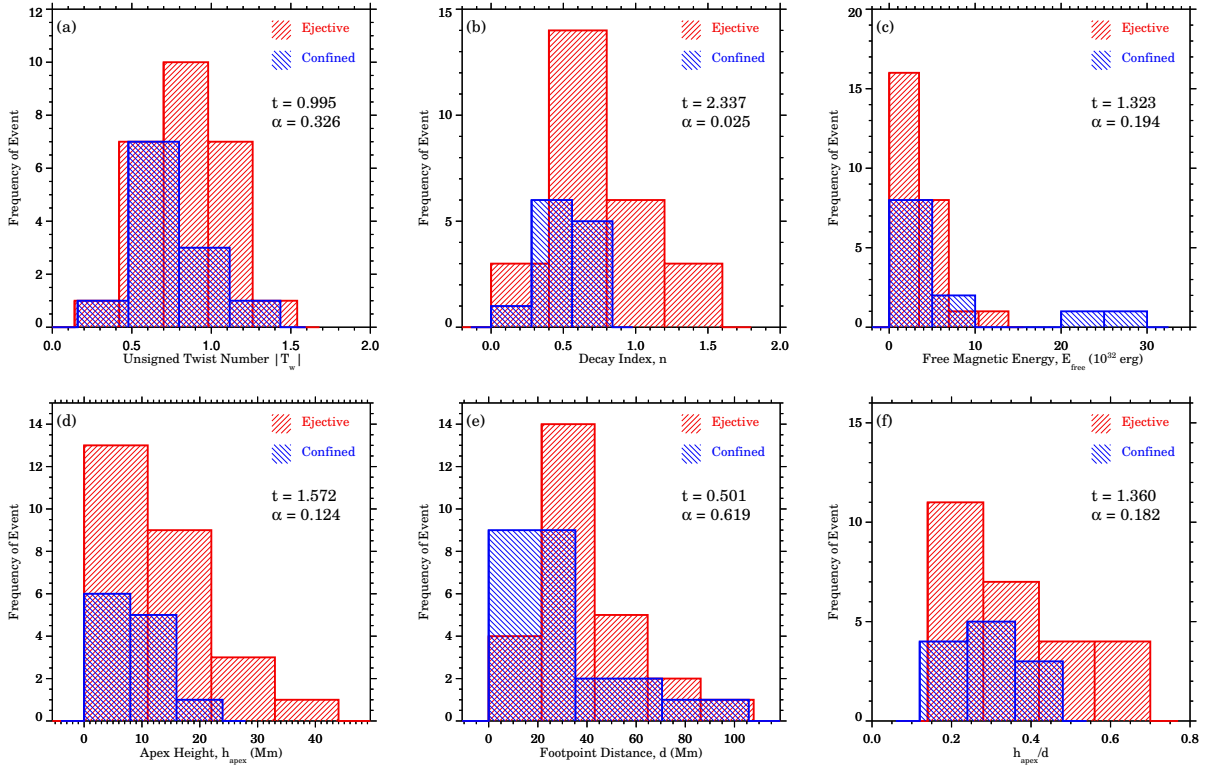
Figure 3.4 Histograms of (a) $|T_w|$, (b) n, (c) E_{free}, (d) h_{apex}, (e)d, and (f)h_{apex}/d. Red/Blue represents ejective/confined flares. Student's t-statistic (t) and its significance (α) are shown in each panel.

a moderate positive linear correlation between h_{apex} and d with a CC of 0.62 (Figure 3.5a). The linear fit to these two data pairs is $h_{\mathrm{apex}} = 2.65 + 0.26 \times d$, suggesting that MFRs in our solar cases are of a more flat-arched structure or are only a minor segment of a circular structure. A strong positive correlation between n and h_{apex} with a CC of 0.76 is shown in Figure 3.5c. This should not be surprising, as the strapping magnetic field decays with height so that a low-lying/high-lying MFR is usually relevant to a stronger/weaker strapping effect.

3.1.3 Summary and Discussion

The previous laboratory experiment reveals that the eruptiveness of MFRs is dependent on the interplay between the TI and KI, as represented by the $n - T_w$ diagram. In this study, we intended to establish a solar counterpart to the diagram, by which we may be able to tell the likelihood of a CME based on the observed n and T_w parameters. The key results are summarized and discussed as follows:

First, the TI quantified by n appears to play an important role in differentiating between ejective and confined flares. However, the TI onset criteria ($n \geq n_{\mathrm{crit}} =\sim 0.75$) found here is not a necessary condition for CMEs. Some MFRs in the TI-stable regime still manages to break through the strong strapping field and evolve into CMEs. It, therefore, implies that an additional trigger and driving mechanism may be involved in solar eruptions. A very likely candidate for the alternative process is magnetic reconnection during solar flares. Actually, there are a number of analytical/numerical models invoking magnetic reconnection in the mechanism of CMEs. For instance, in the magnetic breakout model [3], magnetic reconnection leads to the progressive transformation of the magnetic configuration, allowing an MFR to burst open. In the tether-cutting reconnection model [89], magnetic reconnection below an MFR "cut"s the "tether"s of the strapping field to unleash CMEs. Such
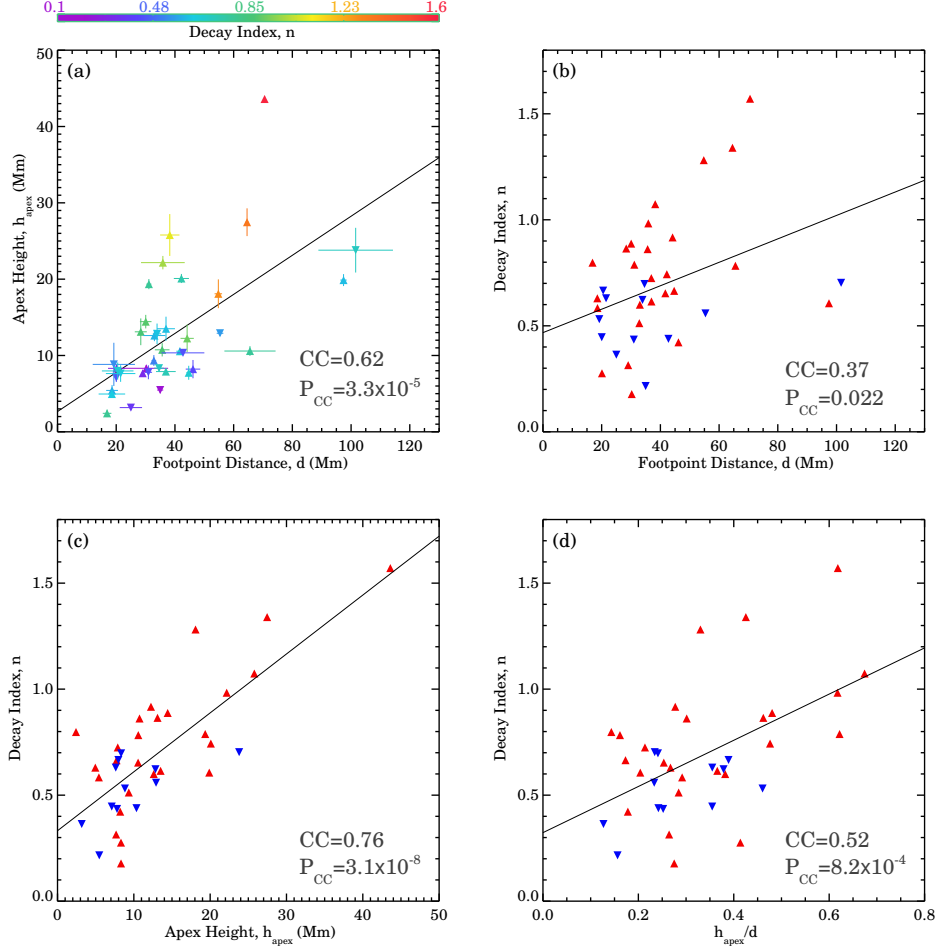
Figure 3.5 Scatter diagrams of (a) apex height $h_{\rm apex}$ vs. footpoint distance d of MFRs, (b) n vs. d, (c) n vs. $h_{\rm apex}$, and (d) n vs. $h_{\rm apex}/d$. Triangles and up-side-down triangles represent ejective and confined flares, respectively. The color is assigned either according to the value of n (panel a) indicated by the color code, or red/blue for ejective/confined flares (panels b-c). The linear Pearson correlation coefficient (CC) and the probability of obtaining a certain CC by chance (P_{CC}) are shown in each panel. The solid lines denote the least-squares fits to data pairs, which are $h_{\rm apex} = 2.65 + 0.26 \times d$, $n = 0.47 + 0.0055 \times d$, $n = 0.33 + 0.028 \times h_{\rm apex}$, and $n = 0.32 + 1.09 \times h_{\rm apex}/d$.

non-ideal MHD processes are absent in the laboratory experiment which was designed to simulate eruptions solely in terms of an ideal MHD process.

Second, it is unclear in this study whether the KI represented by T_w is a major factor for solar eruption. Two MFRs with the highest value of $T_w > 1.2$ erupted, but many other MFRs with smaller values of T_w were also able to erupt, and we tend to believe that KI is less influential. We consider two possible caveats. The first concerns the ongoing debate whether a helical magnetic structure pre-exists before an eruption [86, 17, 26] or is formed in the course of an eruption via magnetic reconnection [119, 2, 87]. There are observational evidence in favor of each scenario [25, 99, 82, 107, 124, 140, 38]. In the latter case, it is not surprising that T_w derived from the pre-eruption magnetic field may be underestimated and can not correctly predict the eruptiveness. The second possibility is that helical KI could result in the deformation of an MFR, but may not allow a huge expansion of the MFR to produce a CME [41]. In this sense, we may consider that KI might be capable of initiating a filament eruption and a flare, but may not be the key factor in driving a CME into the heliosphere.

Third, the laboratory experiment by Myers et al., 2015 [92] shows that there can be both failed TI and failed KI events. Namely, MFRs have more difficulty in eruption than the solar community believed. This is contrary to our results that even the TI-stable ($n < 0.75$) ones can erupt and CMEs can occur regardless of the KI parameter T_w. As mentioned earlier, we speculate that magnetic reconnection, which was absent in the laboratory experiment, maybe the factor causing the differences between the laboratory and the present solar observations, if it alleviates the difficulties in eruption.

The differences between the laboratory results and our results may also arise from multiple sources of assumptions and approximations of this study in contrast to the lab experiment. In the present study, the TI and KI parameters n and

T_w are not directly measured in observations, but rather estimated from MFRs in NLFFF models. The identification of MFRs relies on the quality of NLFFF extrapolation. Although the up-to-date NLFFF extrapolation technique employed here was evaluated thoroughly in comparison with a 3D radiative MHD model and was found to offer reasonably high accuracy of the coronal field reconstruction [138, 136, 30], the direct validation of NLFFF still cannot be performed due to the lack of the coronal magnetic field diagnostics. We'd like to add a caution that NLFFF extrapolation has intrinsic limitations associated with the force-free assumption and is subject to numerous uncertainties in the data reduction and modeling process which are not reflected in our results. It may be that n and/or T_w could not be accurately calculated under the observational limits. In addition, the KI parameter T_w is derived from and averaged over individual field lines, assuming that it's related to the winding of field lines around the axis, but actually, the twist of an MFR could be underestimated by its built-in assumption.

Finally, we would like to mention that the present statistical study is a step forward to access the role of the TI and KI in solar eruptions. Detailed studies of the pre-to-post flare magnetic configuration are also needed to better understand the underlying physics, which will be conducted in particular seperate events with/without magnetic field reconnection in the future.

3.2 Multi-instrument Precursor Study

In this study, we focus on the thermal behaviors of the precursors over one hour before the flare. These two precursors show simple emission structures which are mostly confined to a small area at magnetic PIL (see Figure 3.7).

3.2.1 Emission Mechanism in Multi-wavelengths

In general, energy in the form of non-thermal emissions is released in HXR and MW during the solar flares. The dominant emission mechanism of HXR is bremsstrahlung with electrons precipitating at the footpoints and loop top of a magnetic flux rope structure, which can be approximated by the thick-target model [14]. On the other hand, MWs are emitted by gyrosynchrotron (non-thermal) emission and Free-free bremsstrahlung (thermal) emission mechanism [5]. During this process, thermalization of the precipitated nonthermal electrons results in the formation of hot dense plasma, which evaporates into the corona and leads to the EUV, HXR, and SXR emissions via thermal bremsstrahlung [4, 16, 52]. The emission mechanisms at HXR, MW, SXR, and EUV during the precursor phase of a flare are not different from that during the main flare. The multi-instrument study of thermal emissions will provide a meaningful comparison of different wavelengths in a large temperature range.

3.2.2 Observation of the Precursors

The main phase of the M6.5 flare (SOL2015-06-22T18:23) occurred in NOAA active region (AR) 12371, located at (223", 183"). In Figure 3.6a, the light curve of GOES SXR flux shows two episodes of small-magnitude emissions within one hour before the M6.5 flare. The onset times of the two precursors are 17:24 UT and 17:42 UT, which are denoted as P1 and P2, respectively. The n, T, and EM maps at P1 and P2 derived from AIA data are shown in panels (b) - (g) of Figure 3.6. As mentioned earlier, the two precursors are well confined locally near the PIL (see Figure 3.7 for

more details), enabling a direct comparison of different wavelengths. As shown in Figure 3.6(f-i), there is a spatial correlation among AIA EUV, RHESSI HXR, and GST Hα emissions.

Figure 3.7 further demonstrates their spatial correlation and confinement with the magnetic field. The top and bottom panels of Figure 3.7 show the emission maps of four wavelengths at the precursor times P1 and P2, respectively. A slit is set across the emissions, and the cross-sectional photo-metric intensity profiles of these emissions are plotted and compared with the magnetic field over the slit. Based on the comparison of extrapolated magnetic fields and those derived from spectrum fitting of MW [126], it was found that the precursors in MW occurred in a strong magnetic field region (1200 G) around the flaring PIL. As shown in the middle panels of Figure 3.7, the emissions of AIA EUV, RHESSI HXR, and GST Hα are also confined in similar local areas, while the SXR emission from GOES 15 Solar X-ray Imager (SXI, [45]; Pizzo et al., 2005 [97] extends to a substantially larger region.

3.2.3 Thermal Behavior during Flaring Precursors: Temperature (T), Emission Measure (EM), Electron Number Density (n)

Figure 3.8 shows the temporal variations of T, derived from four data sets using different methodologies, during the precursor phase. The RHESSI result is only partially shown for the first precursor, as the spectrum before 17:25 UT is not qualified to perform a reliable fitting, due to RHESSI night time. At a glance, these T curves show a large discrepancy in the order of magnitude, but, as a general trend, they all reach their maxima around the two precursor times. Specifically, of the four instruments, EOVSA MW exhibits the highest temperature value and changes most rapidly during the precursor times, while GOES SXR and AIA EUV show the lowest temperatures, changing more gradually. The temperature of 15 MK is a clear line of demarcation between EOVSA and AIA/GOES. The range of 10 to 24 MK is where the temperature variation of RHESSI HXR is located. For the first precursor, T of
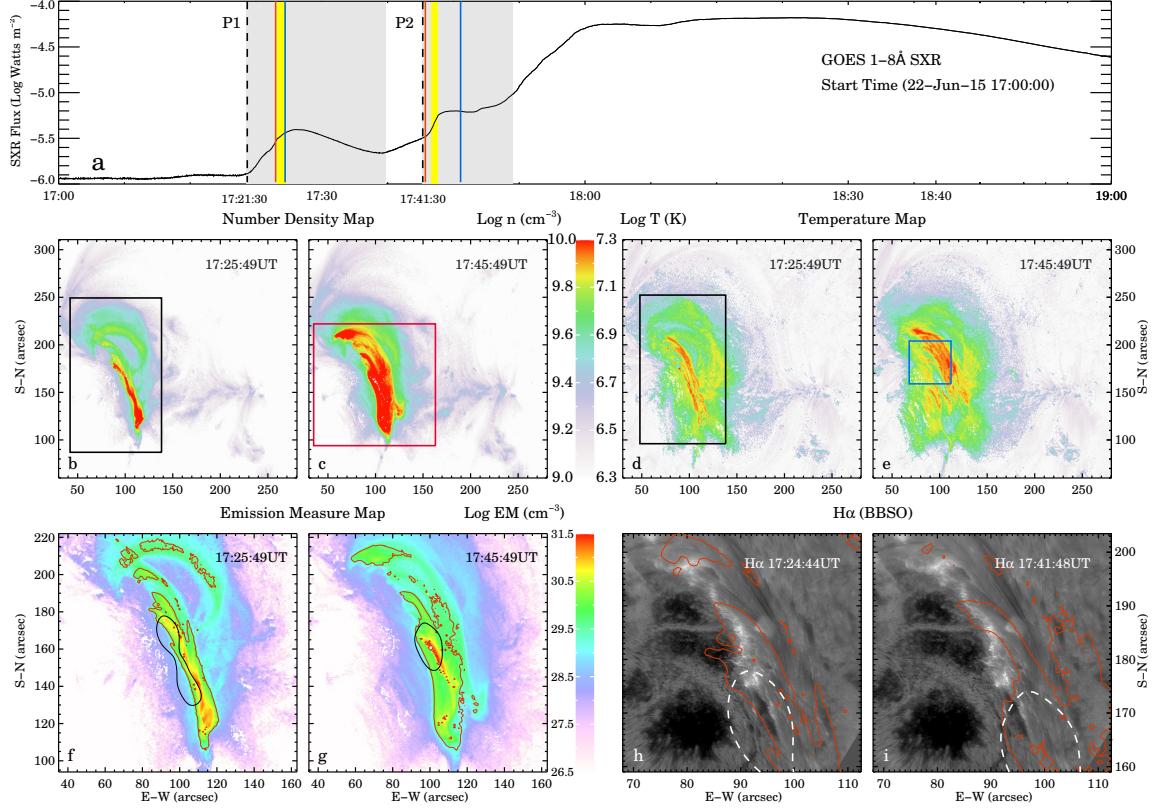
Figure 3.6 Thermal parameter maps at precursor peaks.(a) GOES SXR flux light curve, with the gray shaded area P1 and P2 denoting two precursor periods. The red and blue line marks the time of n and T maps in (b)-(e), respectively. The yellow shaded areas indicate the time of HXR imaging integration time in (f)-(g). (b)-(c) n maps, derived from AIA DEM analysis, at the selected times of P1 and P2. (d)-(e) T maps, derived from AIA DEM analysis, at the selected times of P1 and P2. The black rectangular boxes in panels (b) and (d) are drawn to define the area used in the calculation of average n and T (shown in Figures 6 and 4). The red square box in panel (c) is drawn to mark the field-of-view (FOV) of panels (f)-(g), and the small blue square box in (e) indicates the FOV of (h)-(i). (f)-(g) The close-up view of DEM maps of logT =[6.85, 7.35], superimposed with the red contours of 30% density maximum and the black contours of 80% of RHESSI HXR intensity maximum in 6-12 KeV. The HXR imaging time ranges of the two precursors are 17:25:00-17:26:00UT and 17:42:38-17:43:20UT, respectively. (h)-(i) Two snapshots of GST Hα+0.6Å images showing the two precursor brightenings. The red contours show 30% of the density maximum, the same as in (f)-(g). The white dashed contours show 80% of the RHESSI HXR intensity maximum, the same as black contours in (f)-(g).
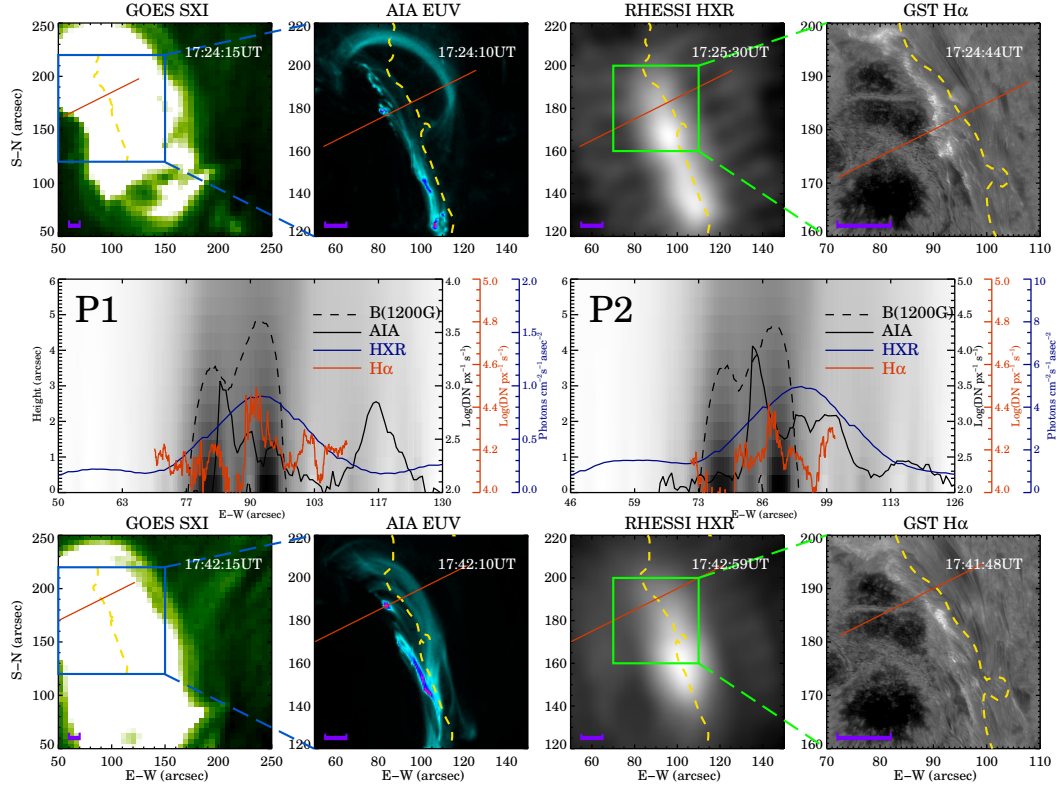
Figure 3.7 Confinement of magnetic field. The top and bottom panels show the precursor emission maps from four wavelengths (GOES/SXR, AIA 131 Å RHESSI HXR, and GST Hα) at the two precursor times P1 and P2, respectively. The blue boxes in the GOES SXI panels mark the FOV of AIA EUV and RHESSI HXR images. The green boxes in the RHESSI HXR images mark the FOV of GST Hα images. The yellow dashed lines in each image mark the location of PIL of the corresponding precursors, the PIL was defined by the zero value contour of vertical magnetic field obtained by SDO/HMI. For each precursor, the slits are centered on the same location, but the lengths of the slits are not necessarily equal. The purple segments in each top and bottom panels indicate the estimated D values. The middle panel shows the photometric intensity profiles along the slit and the spatial distribution of magnetic field strength calculated from the extrapolated 3D NLFFF. The dashed line marks the magnetic field of 1200 G.

EOVSA peaks earliest, followed by T of AIA and GOES. The T peak of RHESSI is unknown due to the incomplete temporal coverage of the RHESSI fitting results. Such an order is not surprising considering the empirical tendency for the HXR (or MW) emission temporally coincide with the time derivative of the SXR emission of a solar flare, known as the Neupert effect [121]. For the second precursor, however, the T peak of EOVSA is lagging behind that of RHESSI by ∼100 seconds. We plotted the time derivative of the GOES SXR light curve (grey line in the top panel of Figure 3.6) and found that its peak coincides in time with the peak of RHESSI HXR emission, as the Neupert effect indicates. The temporal delay of MW to HXR emissions has been reported before in some events, but often in the order of magnitude of seconds [106]. The 100-second delay presented here is certainly not expected. The possible reasons are discussed in Section 3.2.4.

Likewise, Figure 3.9 shows the temporal variation of EM, derived from AIA EUV, GOES SXR, and RHESSI HXR data, during the precursor phase. The peak EM of RHESSI HXR is at the same level as the peak EM of AIA EUV and GOES for the first precursor ($10^{48}cm^{-3}$), at almost the same time. However, the second peak of the AIA EUV is hard to distinguish because EM is constantly increasing. Likewise, the second peak of RHESSI HXR is unknown because of the data gap. There is a striking similarity between the EM curve obtained from the AIA EUV data and that from the GOES SXR data, especially during the period of the first precursor. Starting from 2 $\times 10^{48}cm^{-3}$, the EM profiles of AIA EUV and GOES SXR reach 5 $\times 10^{48}cm^{-3}$ during the precursor times. The EM curves obtained from the RHESSI HXR data, however, change more rapidly over a wide range (1.5 $\times 10^{47}cm^{-3}$ to $3\times 10^{48}cm^{-3}$), but are always less than AIA and GOES.

Figure 3.10 shows the temporal variation of n, derived from AIA EUV and EOVSA MW data, during the precursor phase. Despite their significant difference in magnitude, both n curves show peaks at the two precursor times, and EOVSA MW
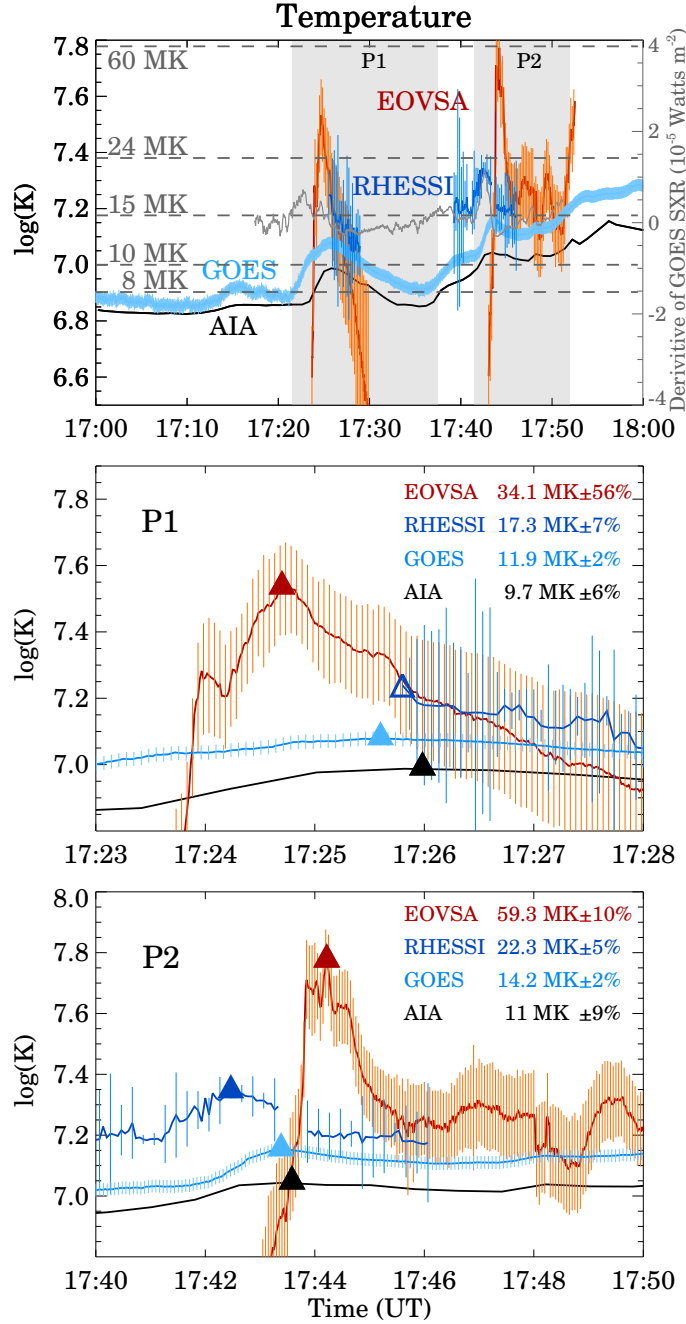
Figure 3.8 Temporal variations of temperature. Top panels are temporal variations of temperature, derived from AIA (black), GOES (light blue), RHESSI (dark blue), EOVSA (red), and the derivative for GOES SXR (gray) during the precursor phase. The gray shaded areas P1 and P2 indicate two precursor periods. Middle and Bottom panels are the magnified view of the temporal variation of T during the two precursor periods. The solid triangle symbols mark the peaks of corresponding curves. Their values and uncertainties are listed in each panel. The hollow dark blue triangle in the middle panel indicates that RHESSI's peak of the first precursor is unknown because of the data gap before 17:25:00UT.
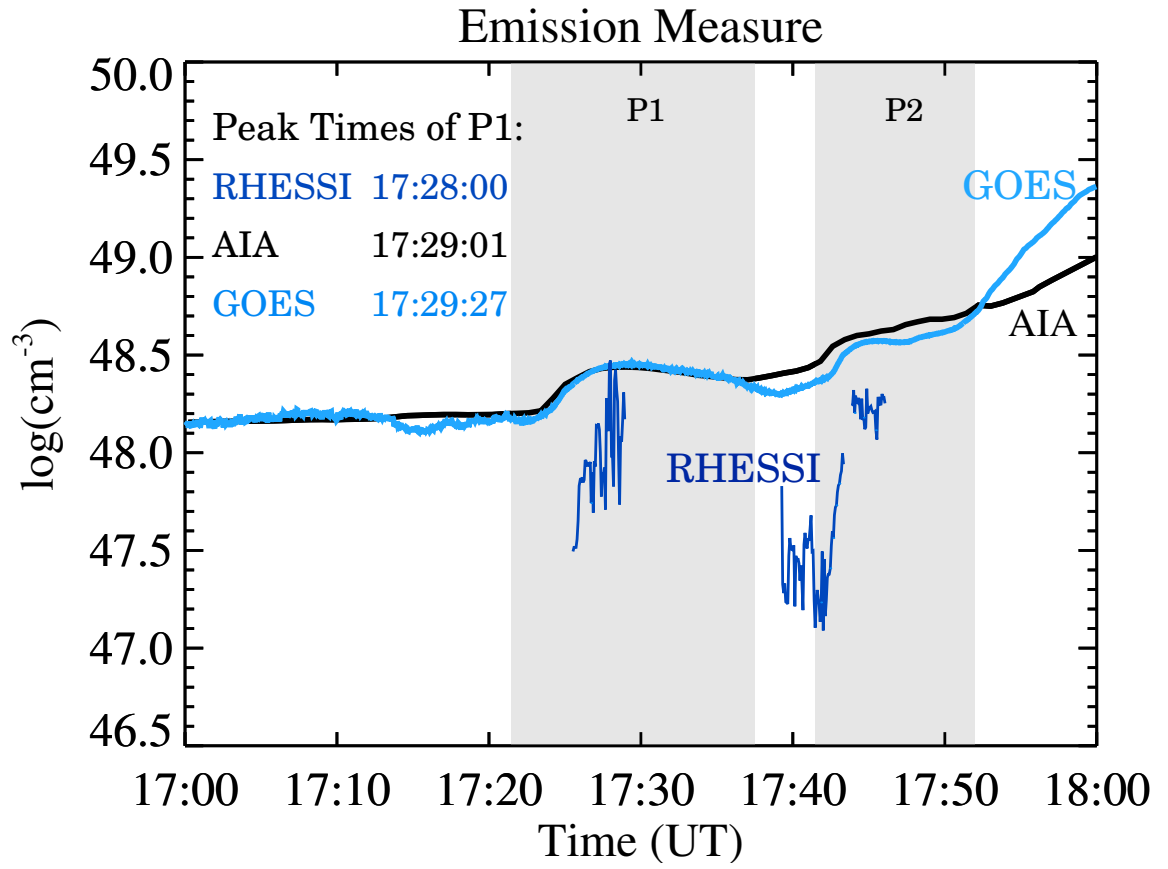
Figure 3.9 Temporal variations of emission measure ($\log cm^{-3}$) and peak times of AIA(black), GOES(light blue) and RHESSI(dark blue) during 17:00UT to 18:00UT. The gray shaded areas P1 and P2 indicate two precursor periods.
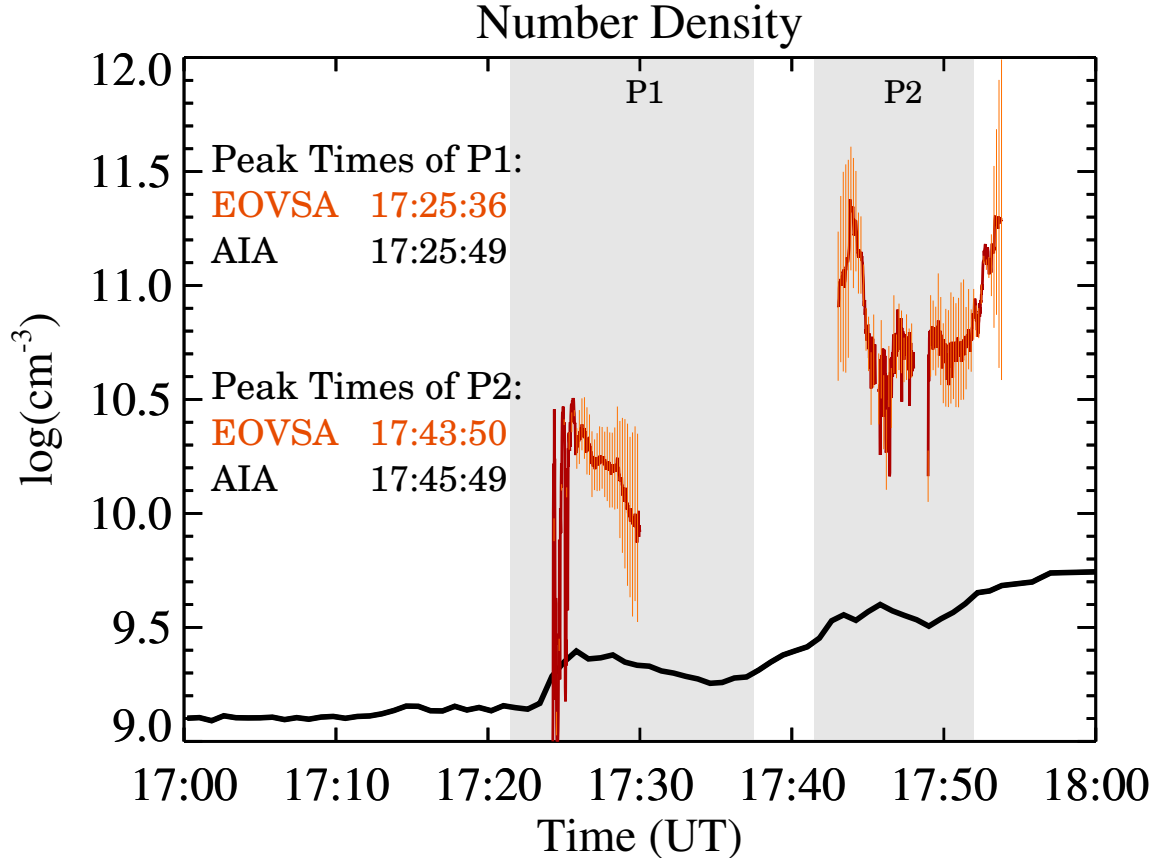
Figure 3.10 Temporal variations of number density (n) and peak times of AIA (black) and EOVSA (red) during 17:00UT to 18:00UT. The gray shaded areas P1 and P2 indicate two precursor periods.

emission always peaks ahead of AIA EUV emission. It is not surprising, considering that the temporal variations of AIA EUV and GOES SXR are almost identical.

Figure 3.11 shows the time variations of AIA ΔEMs integrated over different temperature ranges of log(T)=0.1. Concerning the two flare precursors, there are generally two types of curves in the figure: the ones with two clear peaks at the precursor times and the ones without. For the former ones, the higher the temperature level, the clearer the peaks are observed during the precursor times, except for the black curve which shows the lowest Δ EM at the lowest T. It partially explains why AIA's T peaks always come before the peaks of EM or n (Figures 3.8-3.10). Another type is that curves with the temperature of log(T) <6.65 (T <4.5 MK). The
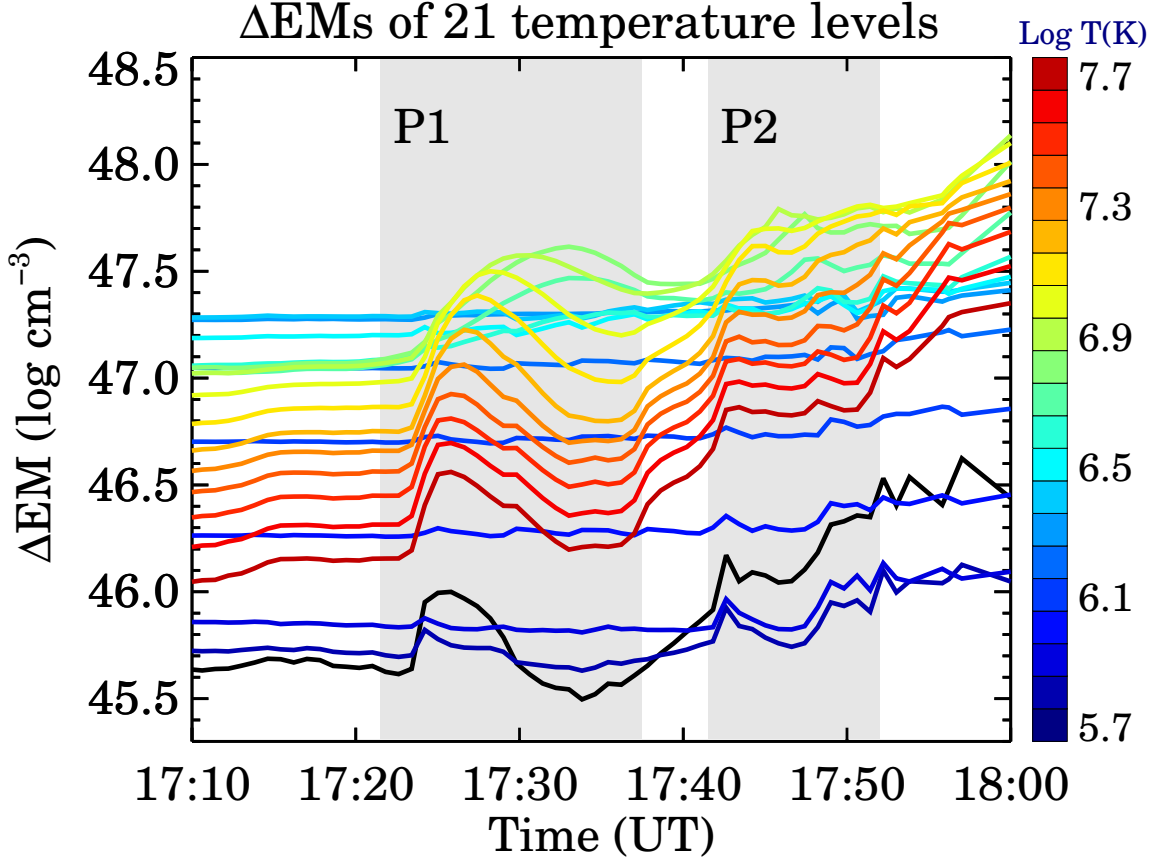
Figure 3.11 Time profiles of AIA ΔEMs integrated over 21 temperature ranges of log(T)=0.1. Each curve shows the temporal variation of differential emission measure at the corresponding temperature level. High temperature levels (log(T) >6.65) show clear peaks at two precursor times. Low temperature levels (log(T) <6.65) do not have clear peaks except for the curve with lowest temperature (log(T) = 5.65).

magnitudes of Δ EMs are greater at higher temperature levels, but they do not have clear chances during the precursor times.

Table 3.1 summarizes the numerical interval of T, EM, and n of two precursors derived from different data sets as shown in Figures 3.8-3.10. As a response to precursors, the values of these parameters vary depending on different instruments. Specifically, the temperature measured by AIA and GOES increases by ∼3 MK and ∼5 MK, respectively, during both of the two precursor times. The temperature measured by RHESSI increases by ∼10 MK, from 14 to 24 MK for the second precursor, while the temperature measured by EOVSA increases even more, by more than 50% as much as that of RHESSI, from 25 to 59 MK. On the other hand, EM

and number density measured by RHESSI and EOVSA respectively increase at least 10 times during both two precursor phases, while these two parameters measured by AIA and GOES increase only with the same order of magnitude. In general, the measurements by AIA and GOES show the similar lowest numerical values and the least variations, even though their results were obtained independently by two different methodologies. To conclude, the increases of the thermal parameters detected by AIA and GOES are at the same level. EOVSA's thermal parameter changes at least 10 times as much as that by AIA in the measurements of n and T. As for HXR emission, the temperature increase detected by RHESSI is at least twice as much as that by AIA and GOES.

Table 3.1 GST High Resolution Data

	Log(T) unit K	Log(n) unit cm^{-3}	Log(EM) unit cm^{-3}
AIA	$6.75\pm6\% - 7.05\pm9\%$	$9.20\pm57\% - 9.60\pm68\%$	$48.20\pm1\% - 48.60\pm2\%$
DOES	$6.90\pm2\%) - 7.15\pm2\%$	N/A^a	$48.15\pm5\% - 48.58\pm5\%$
RHESSI	$7.05\pm40\% - 7.35\pm5\%$	N/A	$47.09\pm63\% - 48.47\pm27\%$
EOVSA	$6.50\pm56\% - 7.79\pm10\%$	$9.85\pm81\% - 11.4\pm31\%$	N/A

^{a}'N/A' means that this parameter was not obtained from the corresponding method.

3.2.4   Summary and Discussion

To summarize, we present a case study of the temporal variation of T, n, and EM derived from different data sets during a flare precursor period. The results from different data sets show apparent temporal consistency among the thermal parameters in multi-wavelengths, as well as significant quantitative differences, which is likely due to different emission mechanisms as well as different methodologies applied in the

data analysis of different instruments. During the precursor phase, the temperature measured by AIA/GOES, RHESSI, and EOVSA varies over the ranges of 8-15 MK, 10-24 MK, and 15-60 MK, respectively.

Of all the available measurements, RHESSI has the smallest EM value which varies from $1.5 \times 10^{47} cm^{-3}$ to $3 \times 10^{48} cm^{-3}$ and EOVSA has the largest number density variation from 1 to 3 $\times 10^{10} cm^{-3}$. AIA/GOES has the most gentle variations in EM of 1.5 to $4 \times 10^{48} cm^{-3}$ and n of 2 to 4 $\times 10^{9} cm^{-3}$.

Note that EM and n have the following relationship:

$$EM = \int n^2 dV \qquad (3.1)$$

Our results are summarized as follows:

1. GOES SXR and AIA EUV have almost identical EM variations (especially before 17:52 UT), and very similar T variations (especially after 17:23UT). During the precursor phase, both EM and T measured by GOES SXR and AIA EUV passbands are raised to twice their initial values (T increases from 8 to 15 MK, and EM increases from 1.5 to $3 \times 10^{48} cm^{-3}$).

2. Compared to GOES SXR and AIA EUV, RHESSI HXR shows greater temperature changes at the 15 MK level and above. EM measured by RHESSI HXR during the precursor phase is 10 times higher than it was before the precursors. For the first precursor, they have very close peaks no matter in magnitude or temporal sequence.

3. The T peak measured by EOVSA MW (59 MK) is almost 3 times higher than the T peak measured by the AIA EUV and GOES SXR (15 MK). The n peak of EOVSA MW (3 $\times 10^{10} cm^{-3}$) is more than 10 times higher than the n peak of AIA EUV (3 $\times 10^{9} cm^{-3}$). EOVSA MW exhibits high thermal variations of T and n, and it has the greatest uncertainties in its measurements as well.

It is clear that AIA and GOES, compared to RHESSI and EOVSA, show lower temperatures and smoother variations. Such a result is not very surprising, as different instruments, operating at different wavelengths, inherently are sensitive to different temperature ranges. Moreover, the difference is also the result of different emission

mechanisms at play as well as the result of different emitting area selections used in the temperature calculation. For AIA and GOES, the temperature measurements are averaged over a large area. Specifically, AIA temperature is averaged within the black boxes in Figure 3.6b,d, and GOES receives emissions from the whole solar disk. On the other hand, the temperature derived from EOVSA MW data reflects the instantaneous thermal behavior within a small area of precursor brightening, and the temperature derived from RHESSI HXR data is calculated within the footpoints and loop top of the HXR emission.

The variations of temperature for AIA and GOES are in good agreement with each other. However, there is a constant difference of about 3-5 MK in their magnitudes. As shown in Figure 3.11, the hot components (>4.5 MK) of AIA DEM are increasing from 17:13UT, whereas the cold components (<4.5 MK) remain unchanged. Considering AIA EUV and GOES SXR have almost identical EM variations (Figure 3.9), the difference in temperature between AIA EUV and GOES SXR is probably due to the unchanging cold components of AIA emissions. It also explains why the difference is not so obvious until 17:13 UT, which is when the hot components start to increase.

The temperature derived from EOVSA MW data shows a larger variation and a higher maximum value than that from RHESSI HXR data. This is probably because the emitting area used in calculating MW temperature is much smaller than that in calculating RHESSI temperature, i.e., 10"$\times$30" vs. $\sim$ 30"$\times$50" according to HXR images.

Besides the difference in magnitudes, we notice a significant long time delay (100s) between the temperature peak of RHESSI HXR and that of EOVSA MW observed from the second precursor. The time delay of MW flux peaks relative to HXR flux peaks has been known for a long time. For example, a statistical study of 57 bursts from 27 solar flares shows that such delays are 6$\pm$5s for impulsive flares and

54

15±6s for non-impulsive ones [106], which are, however, much shorter than the time delay under the present discussion. Several ideas were adopted for interpreting time delays: the delay is either due to the trapping effect of non-thermal electrons in the loop top and the energy-dependence of Coulomb collisions [68] or to other generic loss mechanisms [62, 67]. The trapping of non-thermal electrons in the loop top may arise due to the magnetic mirroring and the energy-dependent Coulomb collisions because it is more difficult for higher-energy electrons to be scattered into the loss cone than lower-energy electrons [68]. This scenario can explain the observed time delay if the high-energy (>300keV) electrons are responsible for the MW emissions and the low energy (20-200 keV) electrons for the HXR emissions. However, the time delay (100s) that we found for the second precursor is unusually long. In a more general approach, Lee et al., 2005 [66] suggested that the trapping effect can be severe for strongly converging magnetic fields and extended electron ejection time, in which case our observation may be explained. We anticipate that the present observation would motivate theoretical modeling of magnetic evolution combined with the participation of thermal processes in the future.
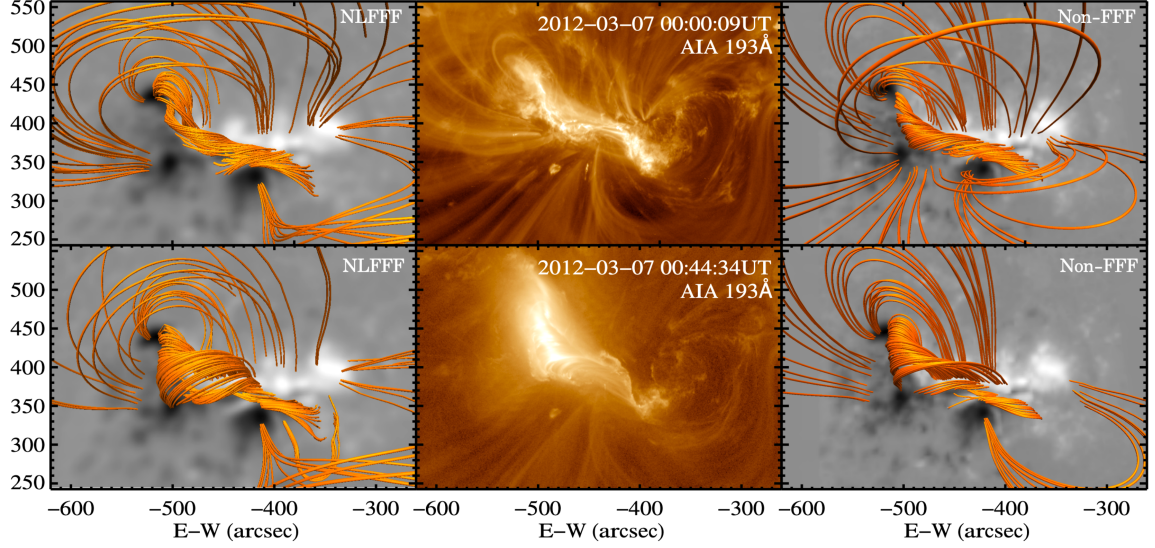
Figure 3.12 3D visualized magnetic field lines of NLFFF and Non-FFF. The upper panels and lower panels show the extrapolation results one hour before and after the flare, respectively. The middle panels show the AIA/EUV 193Å channel images 2 minutes before and 40 minutes after the flare start time.

3.3   Initiation and Back-reaction Study

In this study, we investigate the initiation and back-reaction of the X5.4 flare (SOL205-03-07T00:02) in NOAA AR 11429. The nonlinear force-free field (NLFFF, [133, 135]) model and the newly developed non-force field (Non-FFF, [48, 98]) model are used to help us understand the 3D coronal magnetic field.

Figure 3.12 shows the coronal magnetic fields extrapolated from both NLFFF (left column) and Non-FFF (right column) models before and after the flare, in comparison with the AIA/EUV 193 Å observation (middle column). The AIA observations show the sigmoid-to-arcade evolution, which is consistent with the tether-cutting reconnection scenario. Both models generally agree well with the AIA 193Å observations.

3.3.1   Initiation Mechanism

In order to identify the possible initiation mechanisms of the flare, we study the pre-flare magnetic field conditions. The pre-flare NLFFF model clearly exhibits the presence of a current-carrying MFR prior to the flare, as shown in Figure 3.13. The

MFR is oriented along the PIL and co-spatial with the bright emission in the AIA 304 Å image. The critical threshold of decay index n_{crit} for TI is 1.5 [9, 61]. In this case, however, only n at the top of the MFR is close to 1, while the vast majority of the MFR is in the region where the n value is below 1. This suggests that the external strapping magnetic field has a strong constraining effect on the MFR and that TI is unlikely to be the main triggering/driving mechanism for this eruption.

On the other hand, this MFR is moderate to highly twisted, with T_w values mostly in the range of 0.5 to 1. Some magnetic field lines have T_w values even up to 2 (see Figure 3.14), which adequately exceeds the critical value ($T_{w,crit}$=1.25) of KI [10, 117]. However, in the AIA/EUV observations, we did not find any indication corresponding to the occurrence of KI.

Instead, we found signs of tether-cutting reconnection. We mentioned earlier that the transition of the coronal magnetic field from sigmoid to arcade, as shown in Figure 3.12, is consistent with the tether-cutting reconnection scenario. In addition, as shown in Figure 3.14a, four small flare brightenings (denoted by p1, p2, n1, n2) are distributed on two sides of the PIL, which is also an important observational feature of the tether-cutting reconnection. The magnetic lines coming out of EUV emission brightenings are divided into four groups, according to the position of their footpoints, p1n1, p2n1, p1n2, and p2n2, respectively. Figure 3.14b,c show the variation of the four groups of the MFR before and after the flare starts. It appears that the loops of p1n1 and p2n2 increase, suggesting that some of the magnetic field lines of n1p2 and n2p1 are reconnected to form p1n1 and p2n2.

DAI is a trigger mechanism recently proposed by Ishiguro & Kusano (references). The topology of the DAI scene is the same as that of the tether-cutting reconnection. It shows that when the κ parameter exceeds a threshold value of 0.1, the double-arc loop structure due to the tether-cutting reconnection becomes unstable in the joint region bridging the two reconnected sheared loops systems. A previous study by
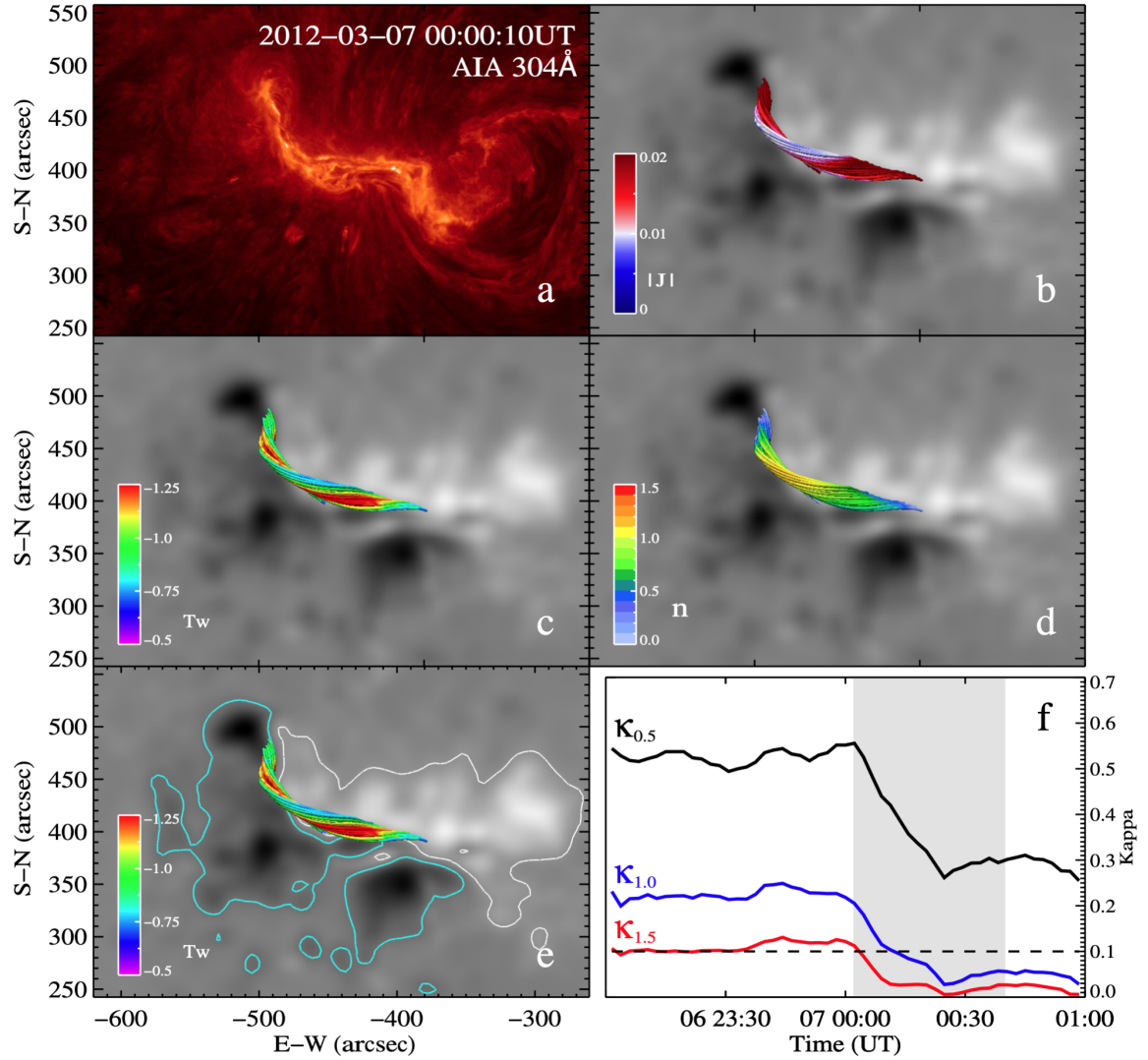
Figure 3.13 NLFFF results of the internal magnetic field at one hour before the flare. Panel (a) shows the chromospheric AIA/EUV observation of 304Å at 2 minutes before the flare. Panel (b)-(d) show the internal field lines with different colors showing the intensity of current density $(A \times m^{-2})$, twist number, and decay index, respectively. Panel (e) shows the MFR of high twist values and the white and cyan contours indicate the areas selected in the calculation of κ where the vertical magnetic field intensity is greater than 300G. Panel (f) shows the time variations of κ values with different threshold twist numbers (T_c). The shaded area in panel (f) indicates the flare period.
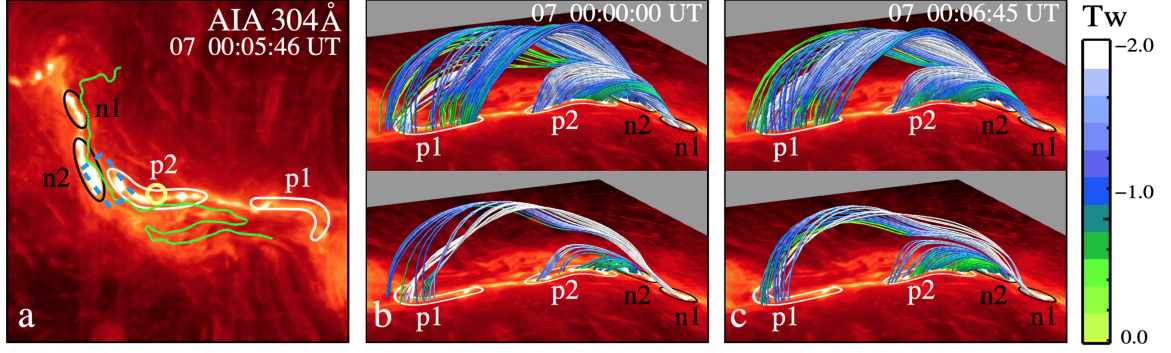
Figure 3.14 The high-resolution NLFFF MFRs overplotted on the AIA/EUV 304Å images. The green curve in panel (a) indicates the PILs. The white and black contours donated as p1 and p2, n1, and n2 in all panels show the four footpoints of MFRs of positive and negative polarity, respectively. The blue boxes and yellow circles in penal (a) mark the position of the ROI in this study and the initiation location determined in [64], respectively. The MFRs in panels (b), and (c) are colored with the intensity of the twist number values.

Kusano et al., 2020 [64] used the κ-scheme method to predict the initiation location of this flare, which is located on one of the brightenings and marked by the small circle in Figure 3.14a. Here we investigate the possibility of DAI triggering this flare by estimating the κ in Equation 1.3.

We use Equation 2.6 introduced in Section 2.1.4 to calculate three κ_{Tc} time variations, corresponding to three values of T_c of 0.5, 1.0, and 1.5, respectively, are presented in Figure 3.13f. All three profiles declined significantly after the flare onset. Except for $\kappa_{0.5}$, $\kappa_{1.0}$ and $\kappa_{1.5}$ both drop below the DAI threshold $\kappa_{crit} \sim= 0.1$. This suggests that DAI may be responsible for triggering the flare.

3.3.2 Back-reaction

As the result of the back reaction by the coronal field evolution required to release energy with conservation of momentum, the photospheric magnetic fields are expected to become more horizontal after flares [53]. Previous observational evidence for back-reaction is abundant, such as the enhancement of the photospheric horizontal magnetic field after the flare onset [125, 132, 130]. Here, we investigate the evolution of horizontal magnetic fields with a time series of NLFFF models. Figure 3.15 shows the

enhancement of the horizontal magnetic field after this flare, with the most significant changes occurring around the PIL. As shown in Figure 3.15a, the B_h profiles start to rise within 5 minutes after the flare start time. Even after the flare, soft X-ray emission reached its peak indicated by the purple line, but the B_h time profiles still show an enhancement at a slower rate until one hour after the flare. The enhancement in B_h is not only seen in the photospheric layer, but also in a certain height range above the photosphere. As an example, the variations of the horizontal magnetic field in the Non-FFF and NLFFF models at a height of 1.5 Mm above the photosphere are shown in Figure 3.15(c1-c2) and NLFFF Figure 3.15(d1-d2), respectively. A similar B_h enhancement is evident in both the NLFFF and Non-FFF models, but the latter shows weaker changes.

Figure 3.16a shows the temporal evolution of the vertical Lorentz force (F_z) at three selected altitudes, averaged over a small region of interest (ROI) marked by the rectangle in the middle and bottom panels. This ROI is along with the PIL and mainly at the location of brightenings p2 and n2. The average value of F_z at all three altitudes shows a significant decrease after the onset of the flare, suggesting the enhancement of downward Lorentz force. The higher the altitude, the smaller the magnitude of the change and the later the change appears. In the middle and bottom panels, we can see a decrease in the area of the upward F_z and an increase in the area of the downward F_z in the ROI.

Figure 3.17 further shows the variation of F_z, B_h and inclination angle Φ (the angle between the magnetic field and the horizontal direction) with time and altitude. The consequences of back-reaction are clearly shown in both NLFFF and Non-FFF models, i.e., an increase in B_h and a decrease in Φ. In addition, Non-FFF shows an obvious increasing downward F_z in the near-surface region.

However, there are non-negligible differences between the two models in the range of altitudes affected by the back reaction. The NLFFF exhibits distinguishable
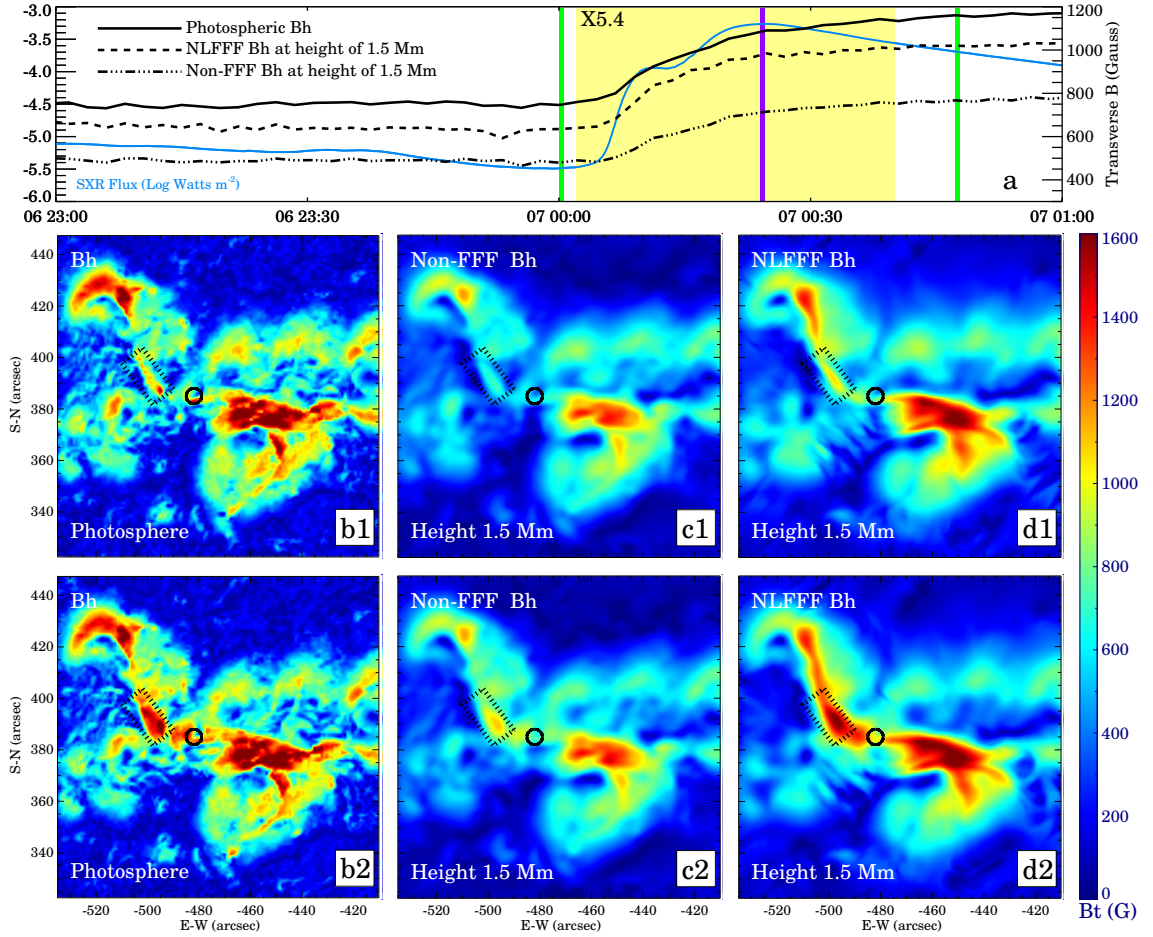
Figure 3.15 Horizontal magnetic field variations on the photosphere and at the height of 1.5 Mm of NLFFF and Non-FFF results, before and after the flare. Panel (a) shows the time profiles of GOES SXR and B_h variations within the ROI. The yellow shaded area indicates the flare period. Two green vertical lines show the times of penal (b1)-(d1) and panel (b2)-(d2), respectively. The purple line indicates the flare peak time. The black boxes and circles in penal (b1)-(d2) mark the position of the ROI in this study and the initiation location determined in [64], respectively.
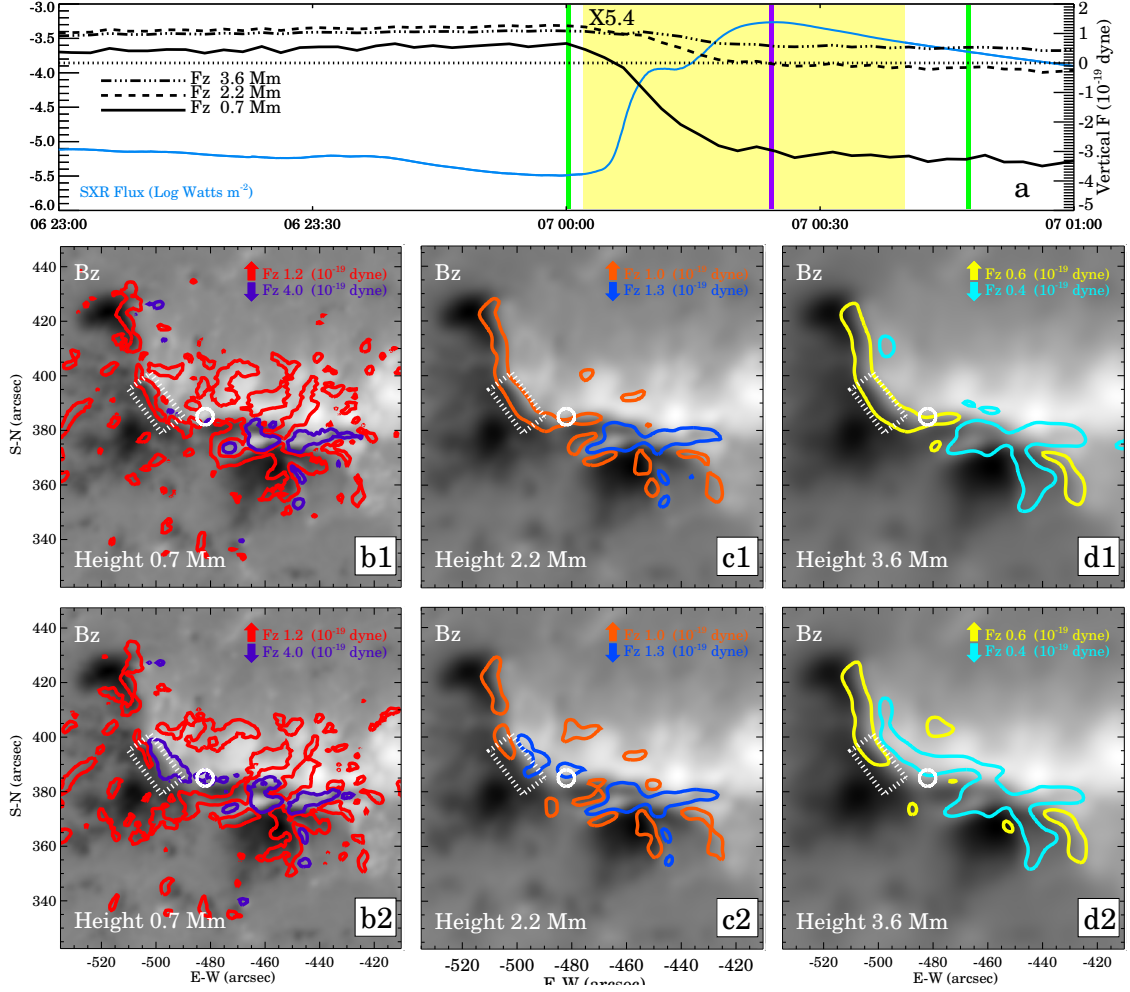
Figure 3.16 Vertical Lorentz force variations at the heights of 0.7 Mm, 2.2 Mm, and 3.6 Mm of Non-FFF results, before and after the flare. Panel (a) shows the time profiles of GOES SXR and F_z variations within the ROI. The yellow shaded area indicates the flare period. Two green vertical lines show the times of penal (b1)-(d1) and panel (b2)-(d2), respectively. The purple line indicates the flare peak time. The white boxes and circles in penal (b1)-(d2) mark the position of the ROI in this study and the initiation location determined in [64], respectively. The different colors of the contours in penal (b1)-(d2) indicated the different directions and magnitudes of F_z.
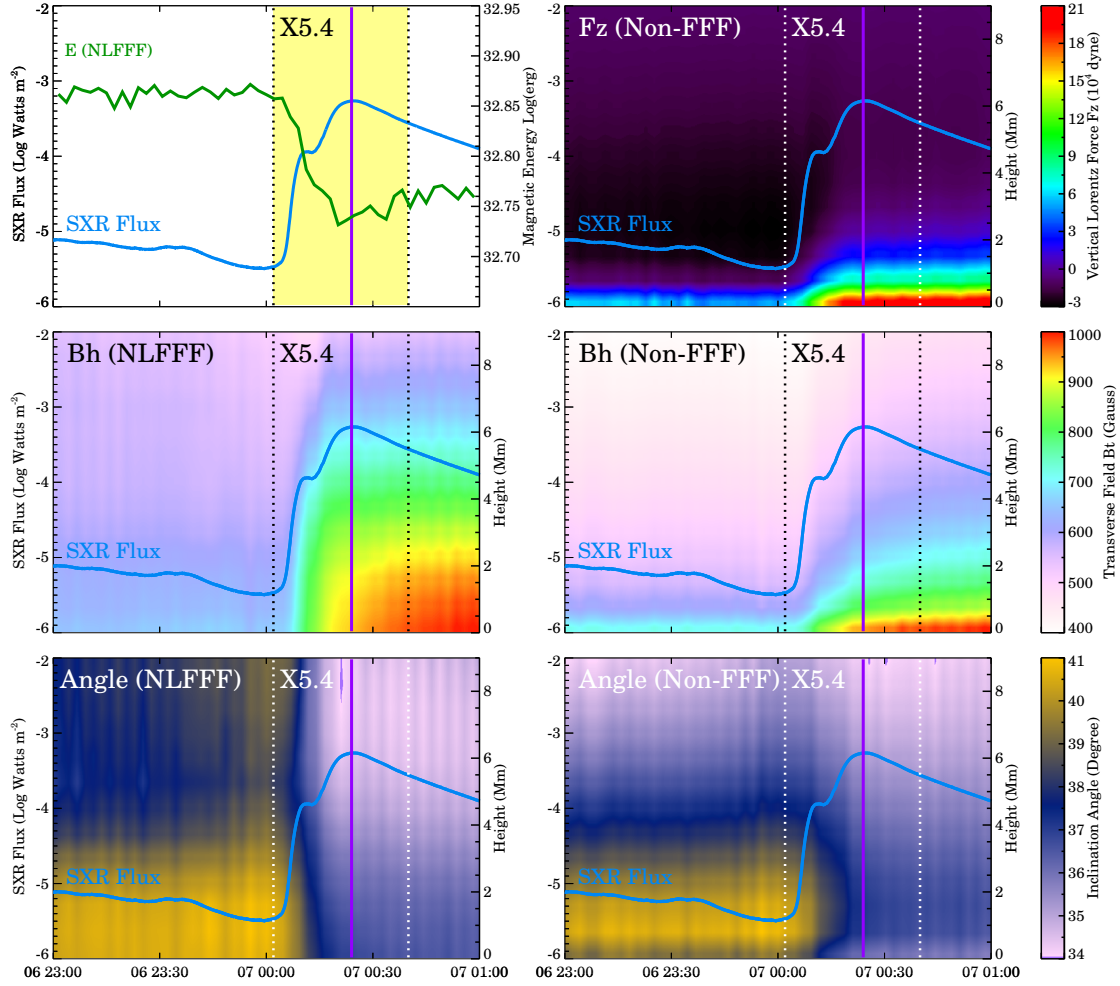
Figure 3.17 The time variations of F_z from Non-FFF, B_h, and Φ from both NLFFF and Non-FFF within the height limit of 10 Mm of ROI. The upper left panel shows the time profiles of GOES SXR and the magnetic free energy of NLFFF. The yellow shaded area indicates the flare period. The vertical dashed lines and purple lines in each panel mark the flare start time, end time, and peak time, respectively.

back-reaction at ~ 8 Mm and below, while in the non-FFF model, the back-reaction is affected in the range below 5 Mm. More discussion about the differences between NLFFF and Non-FFF is presented in Section 4.

3.3.3 Summary and Discussion

In summary, we investigated the initiation and back-reaction of the X5.4 flare on March 7, 2012, and our main results are as follows.

1. The X5.4 flare eruption is triggered by the tether-cutting reconnection and the subsequent DAI.

2. The back-reaction effects, manifested as enhancement of horizontal field and decrease of inclination angle, are observed over a certain altitude range, which is 0–8 Mm for the NLFFF model and 0–5 Mm for the Non-FFF model. In addition, the Non-FFF model shows an increased downward Lorentz force at low altitudes, 0–2 Mm.

We find that the MFR is torus stable, but there are strongly twisted field lines ($T_w \sim 2$) as early as 2 h before the flare, which is sufficient to cause KI. However, there is no observational evidence from the AIA/EUV to support the occurrence of KI. Instead, we find the evolution of "four footpoints to two ribbons", which is a key feature of the tether-cutting reconnection. In the NLFFF, the 3D magnetic configuration is also consistent with the magnetic configuration in the tether-cutting reconnection. The long loops connecting the two far ends of the sigmoid appear to be an MFR with enhanced strong current density, as the result of the tether-cutting reconnection in DAI. Such MFR is a typical meta-stable double-arc shaped MFR in DAI with a concave in the middle part of the MFR, which is more prone to instability than toroidal loops. It is evident that the κ parameter characterizing DAI exceeds the critical threshold of DAI before the flare and then drops below the threshold after the flare starts. These indicate that the tether-cutting reconnection and the subsequent DAI are responsible for initiating the flare. In this study, we identify the

initiation location to be where tether-cutting reconnection happens, which should cover the PIL between n2 and p2 in Figure 3.14a. On the other hand, Kusano et al., 2020 [64] predicted the location of the flare onset using the κ scheme in DAI shown by the circles in Figures 3.14-3.16, which overlapped with the n2 region in this study. In general, these two studies show consistent results in terms of finding the tether-cutting reconnection location.

The Lorentz force in the corona has rarely been studied before, as the coronal magnetic field is not available from observations and the NLFFF model, which is usually used to study the coronal magnetic field, is inherently not applicable to the calculation of the Lorentz force. In this study, we use the Non-FFF model to derive the 3D spatial distribution of the Lorentz force and find an increase in the downward Lorentz force, which, together with the enhanced horizontal magnetic field and decreased inclination angle, confirms the concept of back-reaction of coronal restructuring. To the best of our knowledge, this is the first application of the Non-FFF model to the analysis of the Lorentz force in the 3D solar magnetic field. In addition to the unique advantage of calculating Lorentz forces, the Non-FFF model also reproduces reasonably well the magnetic field in the near-surface region.

It is worth noting that the location of the flare initiation is also the location where the back-reaction is particularly significant. As shown in Figures 3.14-3.16, the most significant back-reaction occurs in the dashed box, which is overlapping part of p2 and n2 and the PIL between. In the tether-cutting reconnection scenario, the magnetic field becomes more horizontal near the PIL and the surface, due to the newly formed short loops there. In that same area, the vertical Lorentz force changes accordingly. This result is in agreement with the expectations of the back-reaction theory and has been demonstrated with the evolution of 3D magnetic fields in this study.

3.4 Light-bridges Study

Although the thermodynamic properties of LBs are well understood taking advantage of the high-resolution observation, the fine-scale magnetic structure of LBs has not been well demonstrated so far besides some basic characteristics, i.e., weaker magnetic field and more horizontal orientation compared to the nearby umbra [11, 76, 103, 69].

In this study, we focus on the high-resolution 3D magnetic structure of the LBs in NOAA AR 12371 using the nonlinear force-free field (NLFFF) models extrapolated from the high-resolution GST photospheric vector magnetograms. Together with the multi-instrument thermal analysis of precursors in this AR, the high-resolution magnetic field analysis may change the view of the ARs.

3.4.1 At the Photosphere

Figure 3.18a presents a GST TiO snapshot of the sunspot group taken on June 22, 2015, at 17:36 UT in AR 12371. The two LBs of interest, labeled LB 1 and LB 2, and their host sunspots were close to the disk center. Soon, a few minutes later, an M6.5 flare (SOL2015-06-22T18:23) initiated in this AR, which has been a subject of intense research due to the complete GST observations of the flare process [59, 79, 126, 129, 139], etc. Although understanding magnetic field structure can help us understand flares, this study is not directly related to the flare. We only use the pre-flare GST data to investigate the magnetic field of LBs.

Figure 3.18d shows the cross-sectional continuum intensity profiles of the two LBs (along the colored slits in Figure 3.18a) and the average of these curves as well as its Gaussian fit curve. The Gaussian full widths at half maximum (FWHM) of LB1 and LB2 are 810 km and 2475 km, respectively. The solid rectangle boxes in Figure 3.18a correspond to the close-up regions of the two LBs, as shown in Figure 3.18b. The high-resolution TiO observation reveals a long central dark lane, intersected with short intergranular lanes, running through the long axis of the narrow
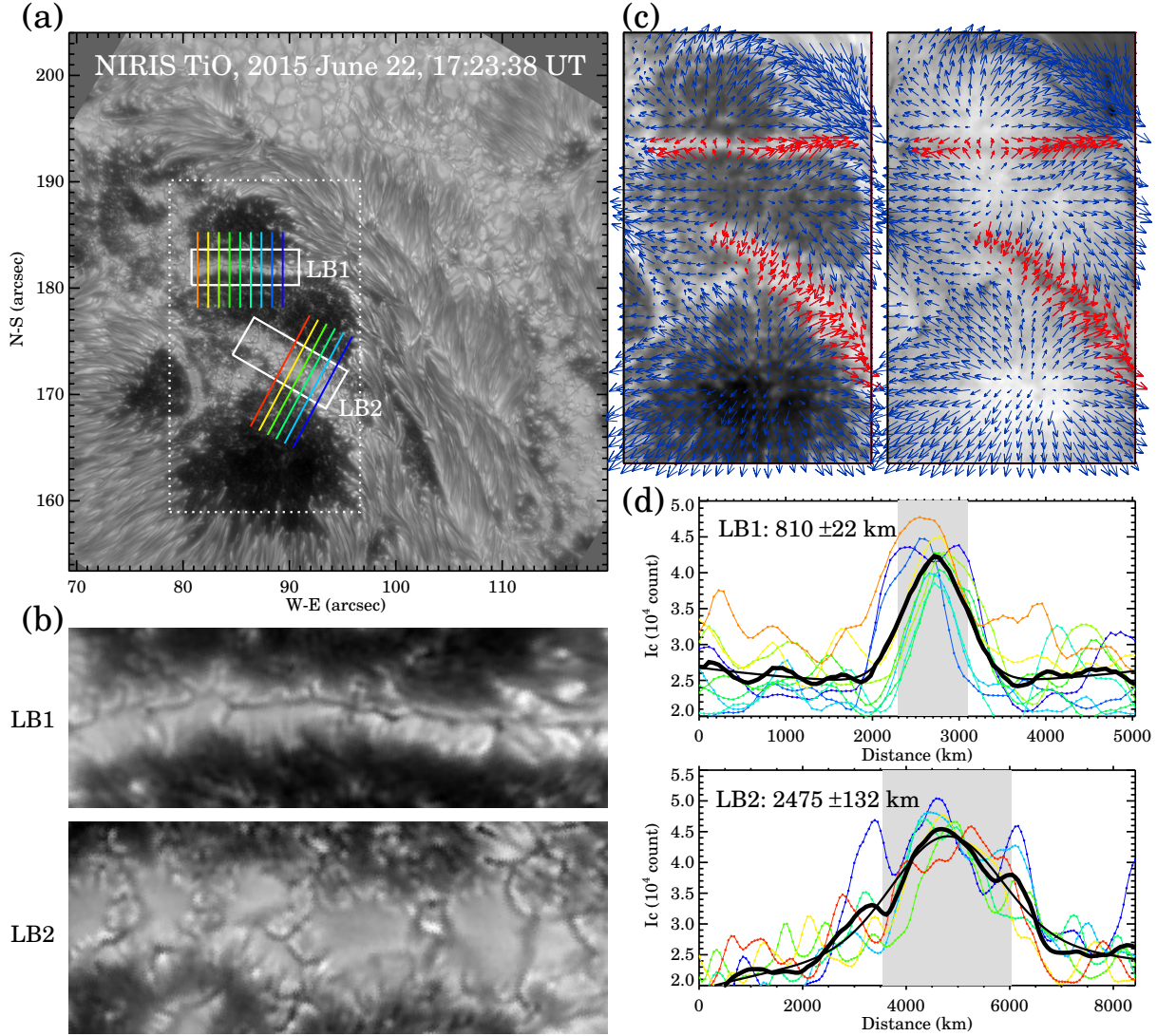
Figure 3.18 GST observation of two LBs. (a) A GST TiO snapshot of AR 12371 that shows the sunspot group and two LBs of interest (labeled LB1 and LB2, respectively). The two solid rectangle boxes are defined for the zoom-in TiO images of the two LBs shown in (b), and the slits cross-cutting LB1 and LB2 show where the cross-sectional continuum intensity were measured. The large dotted rectangle box is drawn to mark the region of interest for the GST continuum and B_z images shown in (c). (b) The zoom-in TiO images of LB1 and LB2. (c) GST continuum and B_z images, superimposed with arrows representing horizontal magnetic field vectors. The arrows in the two LBs are highlighted in red. (d) GST continuum intensity (I_c) profiles (with different colors) along the slits in (a), the mean intensity profile (thick black curve) and the Gaussian fit (thin black curve). For reference, the color of each profile is the same as the color of the slit (see panel a). The Gaussian FWHM and $\pm 3\sigma$ of LB1 and LB2 are provided.

LB1. Such long and short lanes are regarded as manifestations of convective upflows and downflows, respectively [142]. The broader LB2, on the other hand, exhibits a discernible photospheric granulation pattern, suggesting a deeper anchoring in the convection zone [100]. Figure 3.18c shows the NIRIS photospheric horizontal magnetic field vectors superimposed on the continuum and B_z images, with the portion on the two LBs highlighted in red. The two LBs are sandwiched between the sunspot umbrae of positive magnetic polarity, and magnetic field vectors fanning out from the neighboring umbrae converge at LBs. We see a distortion in azimuth at the LB regions, i.e., field vectors in and around the LBs are somewhat sheared to the long axis of the LBs, indicating a disruption of magnetic field there.

We measured magnetic parameters along the colored slits across the two LBs (see Figure 3.18a), and the results are shown in Figures 3.19 and 3.20. The black curve in each panel represents the average of the profiles measured in multiple slits for each LB. There are distinctions between the LBs (shaded area) and umbrae. Compared to the umbrae, the magnetic fields on the two LBs are weaker (in both vertical and horizontal components, B_z and B_h), more horizontally orientated (shown as a larger inclination angle between the magnetic field vector and the local vertical direction), and more sheared (shown as a larger shear angle between the magnetic field vector and the local potential vector). This trend is particularly evident for the wider LB2. Our results are in good agreement with previous observations of the LB magnetic field at the photosphere summarized by Leka et al, 1997. [69].

3.4.2   At the Low Atmosphere

The main goal of this study is to investigate the 3D magnetic characteristics of LBs, which are not directly observable. Therefore, we extrapolate two NLFFF models (Model 1 and Model 2) from the photospheric vector magnetograms of 17:36 UT using the weighted optimization method [135]. Model 1 is extrapolated from the full
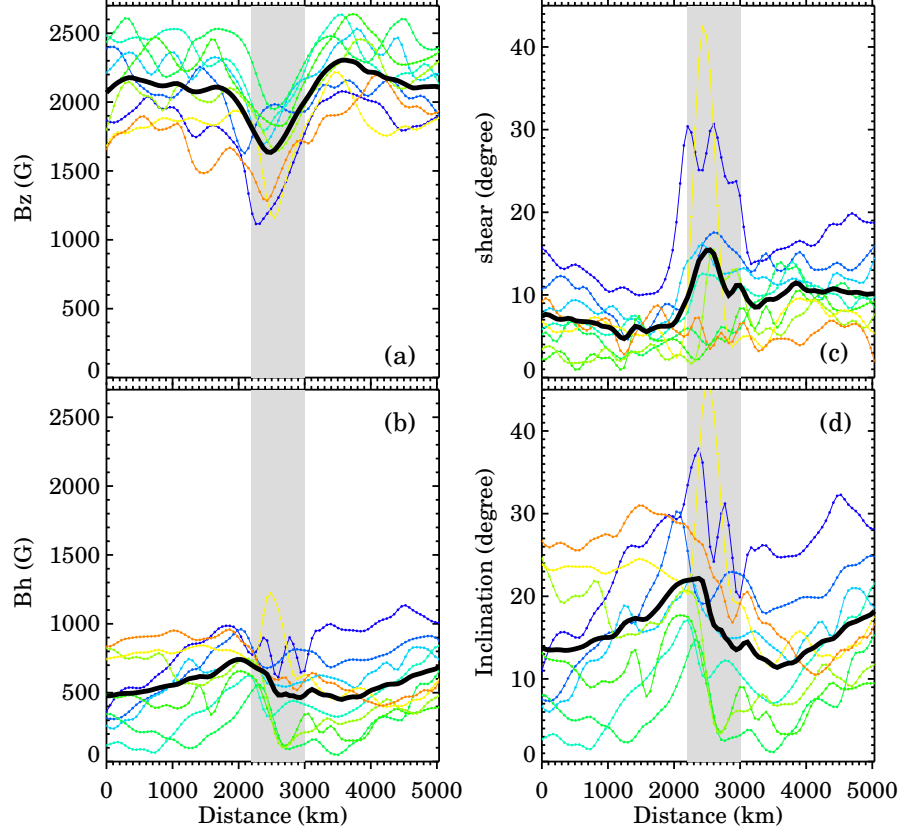
Figure 3.19 Cross-sectional profiles of vertical and horizontal components of magnetic field (panels a and b, respectively), magnetic shear angle (panel c) and inclination angle with respect to the local vertical (panel d), along the slits cutting across LB1 in Figure 3.18a. The profiles of different colors represent the measurements at different locations (see Figure 3.18a), and their averages are shown as the black curves. The shaded region in each panel indicates the approximate position of the LB1, estimated from the Gaussian FWHM of continuum intensity (see Figure 3.18d).
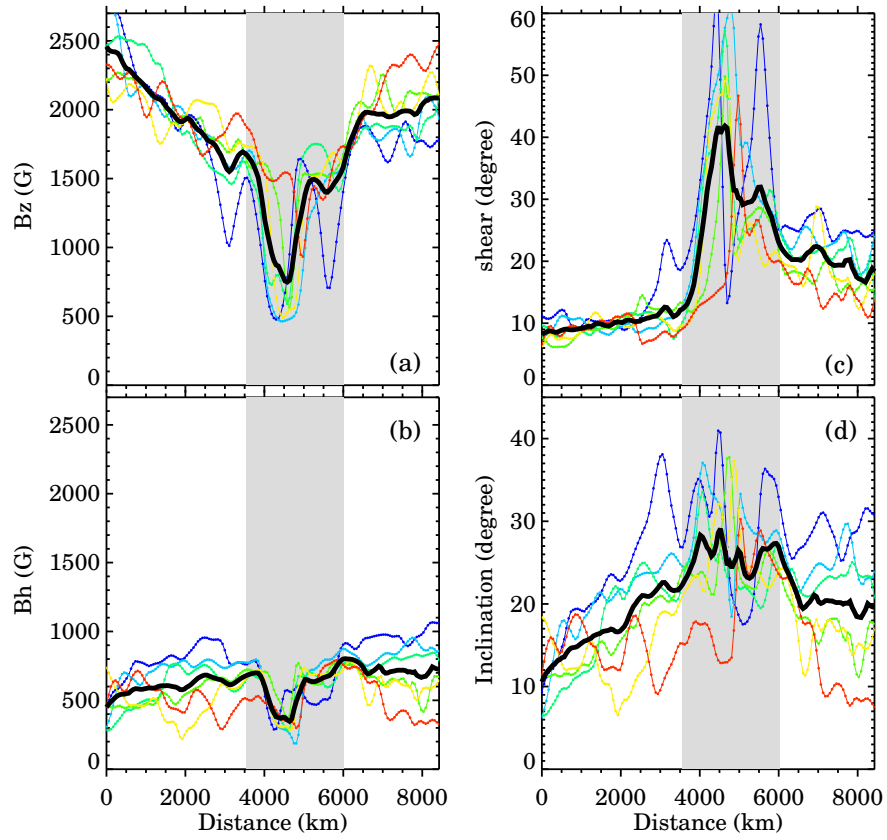
Figure 3.20 Cross-sectional profiles of LB2. Same as for Figure 3.19, but for LB2.

resolution NIRIS magnetograms to show the magnetic structure at fine scales. Since the field of view (FOV) of the NIRIS magnetogram is small (shown as the square area surrounded by the white box in Figure 3.21a) and positive and negative fluxes are not well balanced, which may have an impact on the extrapolation results, Model 2 is extrapolated from the expanded FOV (shown as the entire FOV of Figure 3.21a) but lower resolution HMI magnetograms with the NIRIS magnetograms of reduced-resolution embedded in the middle. Model 2 serves to demonstrate the large-scale magnetic topology and to examine the impacts of small FOV and unbalanced flux on Model 1. Prior to the extrapolation, the bottom boundaries of both models are pre-processed toward the force-free conditions [137].

Table 3.2 Properties and Extrapolation Metrics of Models

Models	Pixel Scale	Dimensions	CWsinθ^a	$\|\nabla \cdot \mathbf{B}\|$
NLFFF model 1	0.057 Mm	$648{\times}648{\times}160^b$ $\sim 37{\times}37{\times}9$ Mm^3	0.26	$8.4{\times}10^{-11}$ (G cm^{-1})
NLFFF model 2	0.28 Mm	$512{\times}512{\times}512$ $\sim 145{\times}145{\times}145$ Mm^3	0.24	$4.9{\times}10^{-11}$ (G cm^{-1})
Potential model	0.28 Mm	$512{\times}512{\times}512$ $\sim 145{\times}145{\times}145$ Mm^3	N/A	$3.6{\times}10^{-11}$ (G cm^{-1})

^{a}the current-weighted average of sinθ [133], where θ is the angle between the current density **J** and **B**
^{b}uniform grid points, same in NLFFF model 2 and Potential model

Table 3.2 lists the properties and the domain-averaged extrapolation metrics, CW$sin\theta$, and $|\vec{\nabla} \cdot \vec{B}|$, of the two models, along with that of a potential field model extrapolated from the same boundary conditions as that of Model 2. Both the NLFFF models show very similar metrics, which are typical for the weighted optimization algorithm and suggest a moderately satisfied force-free and divergence-free condition. The overall magnetic topology obtained from the NLFFF model 2 (Figure 3.21c)

offers a truthful reconstruction of observations in comparison with the AIA 94 Å image (Figure 3.21d). We then compared the B_x, B_y, and B_z components of the two NLFFF models in the same small volume as that of Model 1, and found a very strong correlation between the two models (Figure 3.21b), indicating that the small FOV and the unbalanced flux of Model 1 do not have a serious impact on the extrapolation in this case. Therefore, we are confident in using NLFFF model 1 to characterize the fine-scale 3D magnetic structures.

Before showing the fine-scale magnetic structures, Figure 3.22 obtained from the large-FOV NLFFF Model 2 displays the overall connectivity of magnetic field lines emanating from LB1 (top), LB2 (middle), and the umbra in between (bottom), respectively. The color of field lines indicates the value of twist number ($T_w = \frac{1}{4\pi} \int_L \alpha dl$). Although not on a fine scale, this figure gives us an overall impression of the LB magnetic fields. Apparently, the magnetic field lines from the two LBs exhibit a stronger nonpotentiality, shown in a greater degree of twist and complexity, than the magnetic lines from the umbra.

The following results are all from the high-resolution NLFFF Model 1.

Figures 3.23 and 3.24 show the stratification of the same magnetic parameters of LB1 and LB2 as analyzed in Figures 3.19 and 3.20 at geometrical heights. The curves at each height layer represent the average of magnetic parameters at multiple slits at this layer. At the low layers near the surface, the magnetic field on LBs shows a lower field strength, a larger inclination angle, and shear angle compared to the umbrae, as noted before. As height increases, such differences become less and less conspicuous until a certain height where the gap disappears. It is worth noting that the field strength at the non-bridge umbral regions decreases monotonically with height, while magnetic field strength at the center of the LBs (especially the wider LB2) increases with height in a certain range close to the surface. Specifically, the field strength at the center of LB2 is ~800 Gauss at z = 0 km and increases to
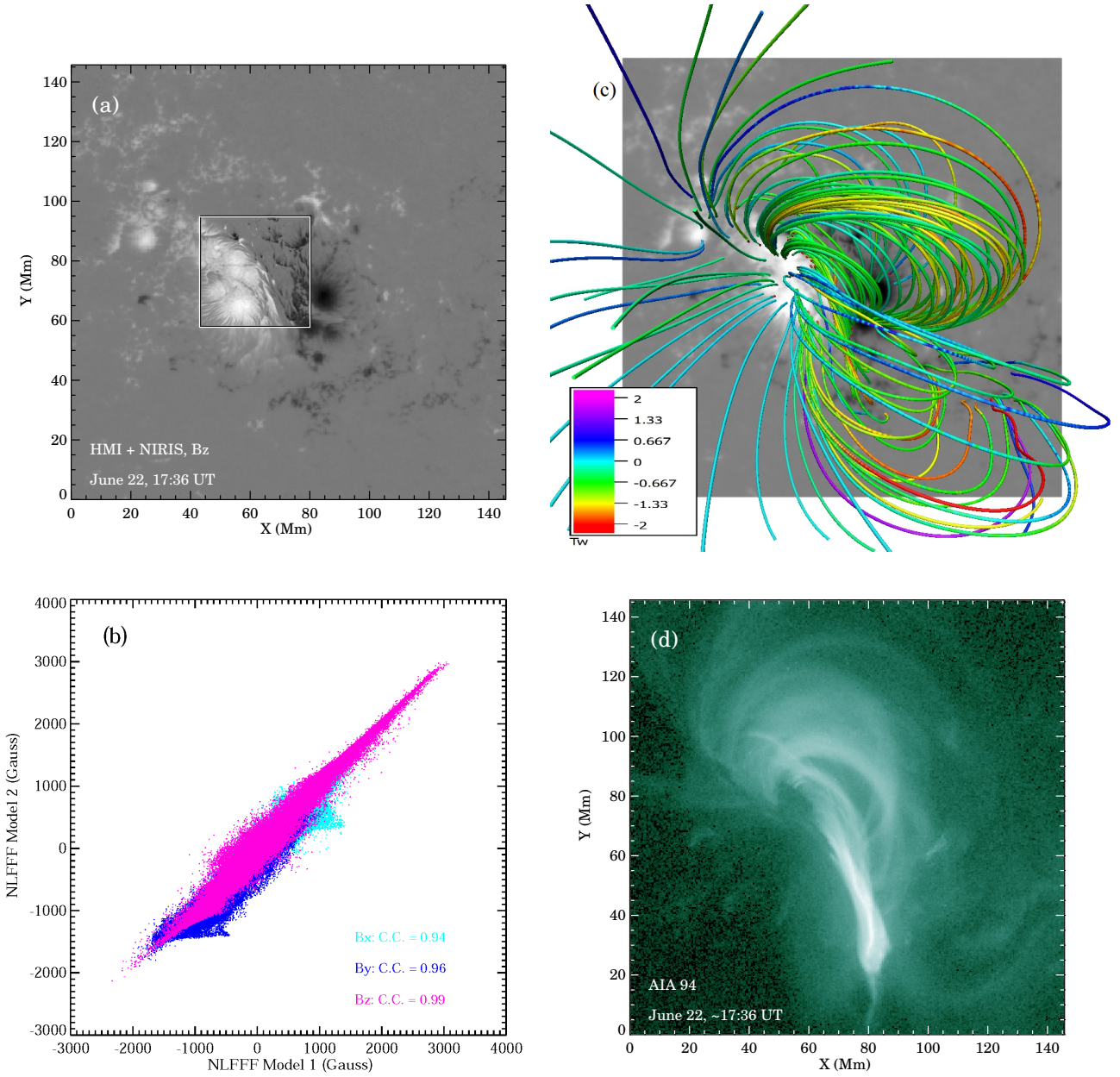
Figure 3.21 HMI NLFFF results and AIA 94ÅImage. (a) The large field-of-view (FOV) HMI magnetogram B_z ($\sim$145 Mm $\times$ 145 Mm) at 17:36 UT, 2015 June 22, with the small FOV NIRIS B_z ($\sim$37 Mm $\times$ 37 Mm) of the same time embedded in the middle (enclosed by the square box). The small and large FOVs define the bottom boundaries of NLFFF models 1 and 2, respectively. (b) Scatter plots of NLFFF model 1 vs. NLFFF model 2 in the same volume as NLFFF model 1, in three components B_x (cyan), B_y (navy) and B_z (pink). The linear Pearson correlation coefficients are shown in the panel. (c) Magnetic field lines obtained from NLFFF model 2, with color indicating the twist number T_w. (d) An EUV 94 Å image taken by SDO/AIA at 17:36 UT.
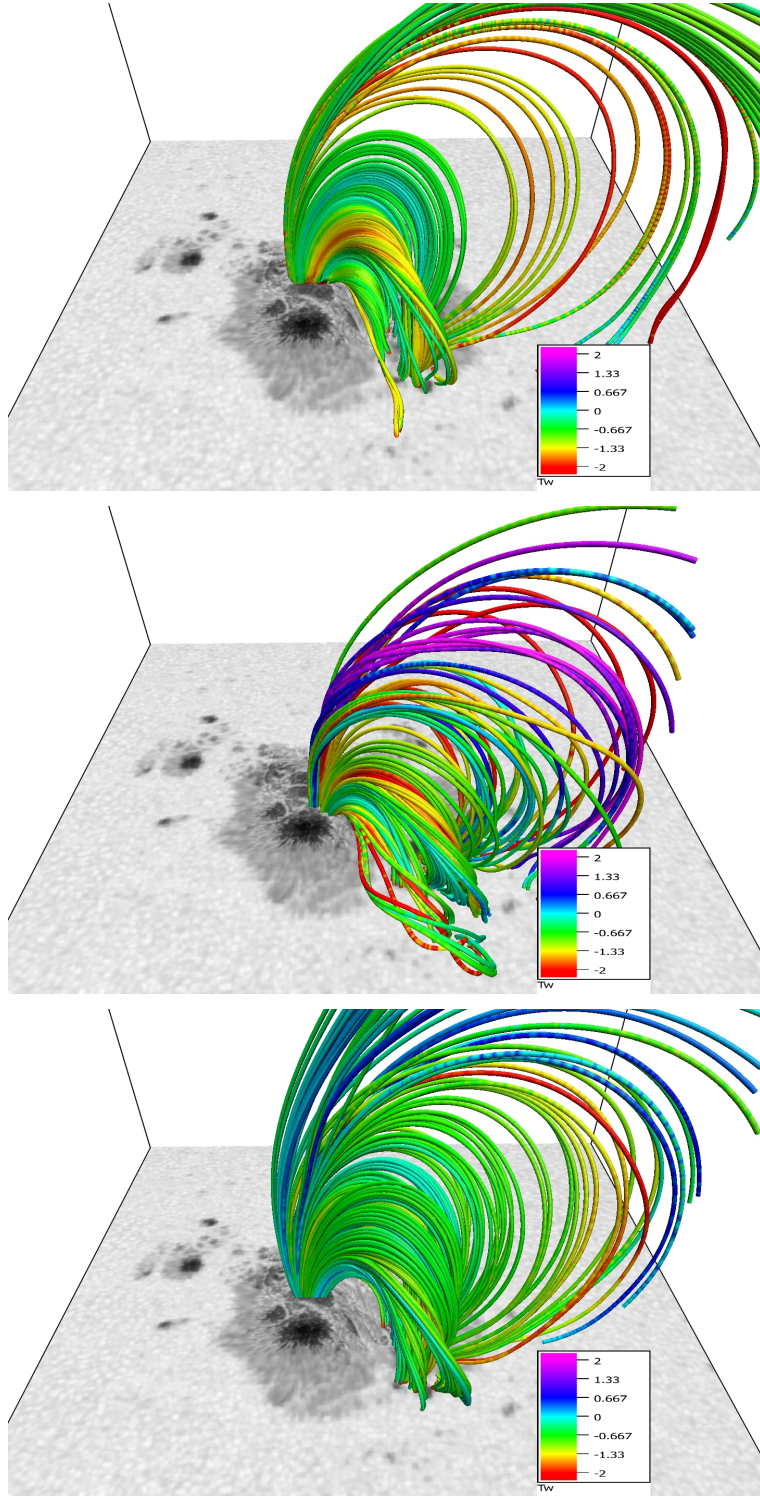
Figure 3.22 Magnetic field lines obtained from the NLFFF model 2, with field lines originating from the locations of LB1 (top), LB2 (middle) and the middle umbra (bottom), respectively, superimposed over the continuum image. The color of field lines indicates the value of twist number T_w.

~1400 Gauss at z = 1000 km, and then decreases with height. The narrower LB1 shows a much higher field strength at z = 0 km, 1800 Gauss, and a much lower range of variation (less than 100 Gauss increase over a range of 400 km), but exhibits the same trend. Correspondingly, the inclination of both LBs decreases sharply compared to the neighboring umbrae, especially LB2 which decreases by at least 10 degrees over a height range of 600 km. This implies that the magnetic lines above the LBs shift to a more vertical direction in the low atmosphere layers. Such changes in field strength and inclination are in accordance with the expected behavior of a low-lying magnetic canopy structure above LBs. At the same time, not surprisingly as shown in Figure 3.18c, we see an increased shear at the two LBs, and this shear decreases with height.

Figure 3.26 shows vertical slices of the magnetic field strength $|B|$, current density $|J|$, and inclination angle. The positions of the two cuts through LB1 and LB2 are indicated by the lines in Figure 3.25a. Clearly, there is a weak-field region inside the wide LB2 that separates the two umbrae, and at the top of this region, magnetic field lines away from both umbrae converge to a more vertical direction and hence form a cusp-like configuration. The height of this cusp is less than 500 km, which can be better seen in the superimposed vectors in the $|B|$ slice and in the low-lying, more horizontal region in the inclination slice. The presence of such a configuration above LB must cause a disruption of the magnetic field, so there must be a large amount of current there. As shown in the vertical slice of $|J|$, currents extend vertically from the surface to 2500 km. The strongest current density on LB2 is 0.4 A m^{-2}, which is comparable to those found previously, e.g., 0.04-0.1 A m^{-2} in Leka et al., 1997 [69], 0.2 A m^{-2} in Jurcak et al., 2006 [60] and 0.3 A m^{-2} in Louis et al., 2021 [85], but at the high end. It is remarkable that $|J|$ at LB2 shows two current sheets near the visible surface which then become closer together at higher
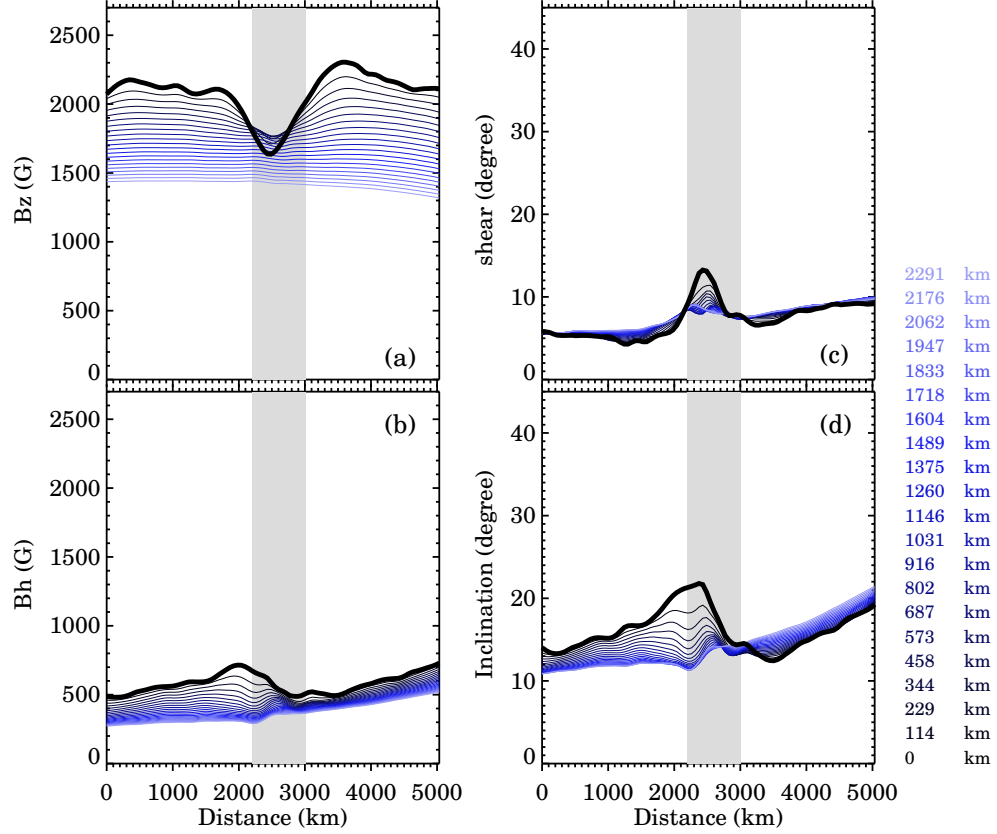
Figure 3.23 The stratification of magnetic parameters of LB1 at different layers, vertical and horizontal components of magnetic field (panels a and b, respectively), magnetic shear (panel c) and inclination (panel d). The curves at each layer represent the average of these magnetic parameters at multiple slit positions in this layer of the NLFFF Model 1. The height information of the averaged profiles is given on the right, corresponding by color. The shaded region in each panel indicates the approximate position of the LB1, estimated from the Gaussian FWHM of continuum intensity.
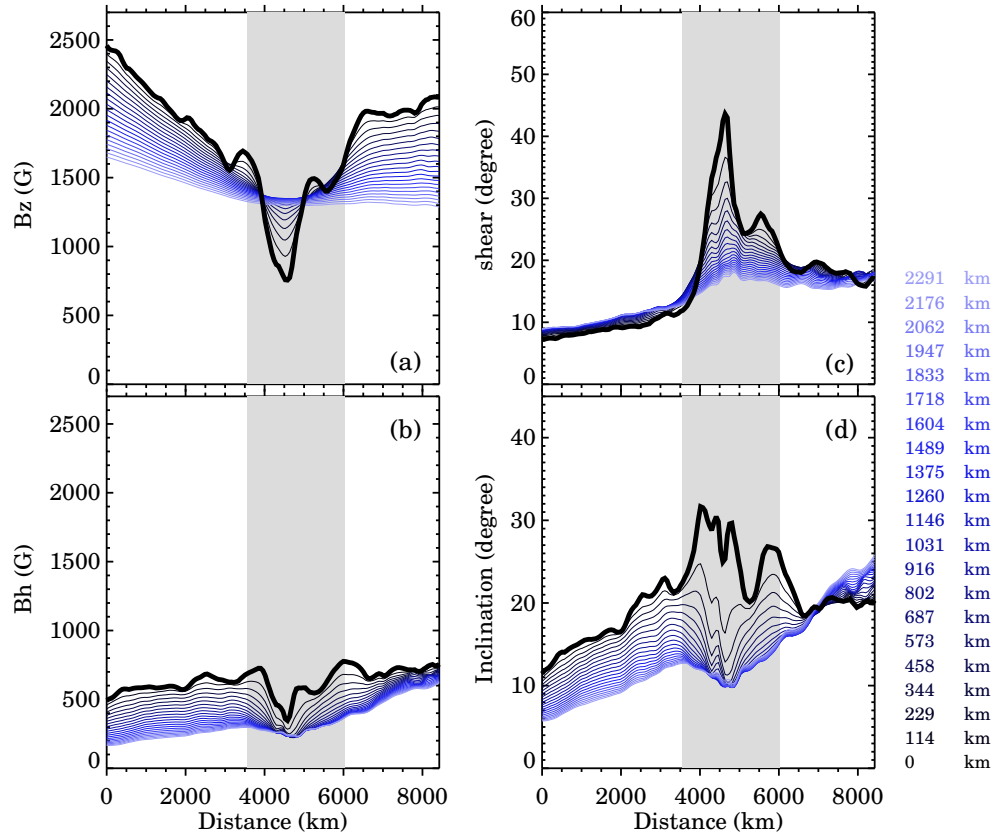
Figure 3.24 The stratification of magnetic parameters of LB2 at different layers. Same as for Figure 3.23, but for LB2.
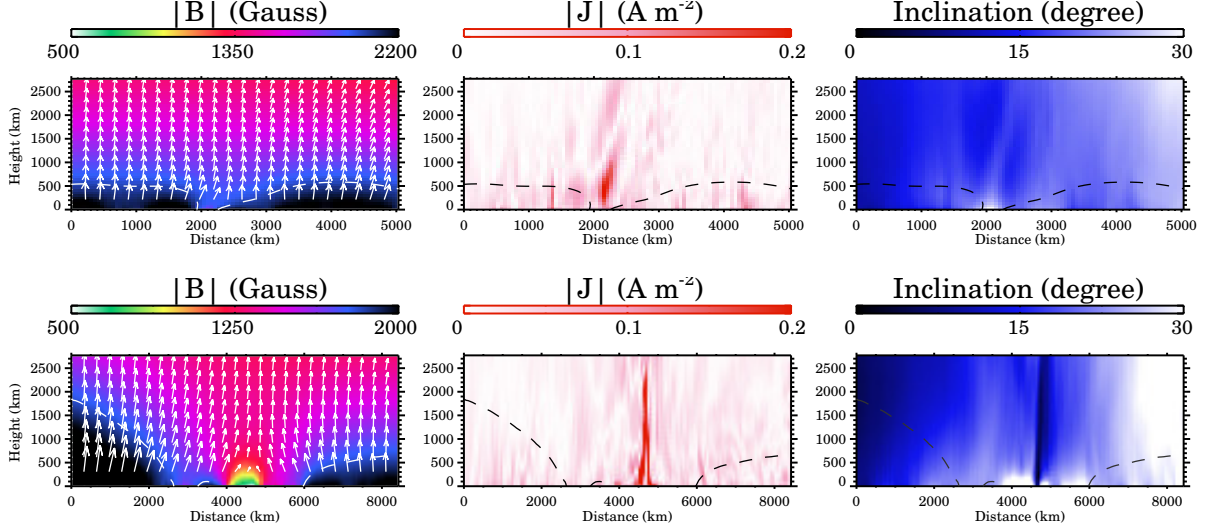
Figure 3.25 Cross-sectional vertical slices through the two slits of LB1 and LB2 (see Figure 8a). Panels show from left to right magnetic field strength superimposed with the magnetic field vectors, electric current density, and magnetic field inclination. A 1800 Gauss contour line is over-plotted.

altitudes to form the cusp shape. In the narrow LB1, the weak field region and canopy structure are very insignificant compared to LB2, but still discernible.

3.4.3   Summary and Discussion

In this study, we use the 3D NLFFF model to study the 3D magnetic field of the two LBs, with special attention to the magnetic canopy structure in the conventional view of sunspots.

Magnetic canopy represents an upward intrusion of field-free plasma from beneath the sunspot umbra. With very high-resolution data we demonstrate the presence of a field-free, or more precisely weak-field, region inside the LBs, covered by the canopy of a stronger and more vertical magnetic field and accompanied by substantial currents extending up to the upper atmosphere. This canopy structure is subtle in the narrow LB1 and more evident in the granular-looking wide Lb2. This may be because the wide LB2 is deeply rooted in the convection zone with a large-scale convective upflow, and hence more readily transports weak fields to

the surface. Our results allow us to get a glimpse of the canopy structure and obtain quantitative measurements about it (shape, size, $|J|$, etc.), which would be important in the context of studying magnetic reconnection and heating mechanism at the chromosphere because this magnetic canopy could be a preferred location for fast magnetic reconnection and responsible for various dynamic phenomena of activity observed in the LBs.

On large scales, we find a substantial difference between the LBs and umbrae in the overall topology of magnetic field lines, i.e., the field lines emanating from the two LBs are more twisted than that from the neighboring umbrae, which is clearly visible in Figure 3.22. This difference may be related to the formation of LBs. A numerical MHD simulation simulates the rise of a buoyant magnetic flux bundle from a convective zone to the photospheric layer during the formation phase of an AR [20]. It shows that magnetic field lines in the LB are highly twisted with a serpentine structure below the visible surface, and are being continuously transported to the surface by convective upflows [115]. Although these magnetic field lines undergo unraveling due to reduced tension force as they rise into the corona, some of the twist may be still retained and is shown in our NLFFF model. Future simulations can help to clarify the topology of the magnetic field as they evolve.

3.5 Joint Study: Generating Photospheric Vector Magnetograms of Solar Active Regions via Deep Learning

This dissertation also includes a joint study of the application of a deep learning tool called the **MagNet** in predicting photospheric vector magnetograms using LOS magnetograms, B_x and B_y taken by SDO/HMI, and full-disk Hα observations collected by BBSO. The purpose of the **MagNet** is to generate vector components B'_x and B'_y which would form vector magnetograms with observed LOS data.

In this study, we mainly provided the high-quality Hα data as the ground truth of the model to train their temporarily closest full disk HMI LOS magnetograms and HMI vector magnetograms

BBSO produces over 4000 full-disk Hα images per year. we excluded low-quality Hα images with an incomplete field of view (FOV) and cloud shades as well as other out-of-focus images. Finally, we selected 2874 Hα images from 2014-01-01 to 2017-08-04.

The conditions to select Halpha images during the selecting process are listed as follows:

1. The image should be intact and clear. Some images are incomplete because of operating issues (including the angle of the telescope, loss of focus, sudden shaking of the telescope, etc), and external blocking items (birds, airplanes, leaves, etc). These problematic images are mostly easy to find and would be removed from the database.

2. The image should be showing the healthy appearance of the solar disk. Because of the issue of the cloud, some of the thick clouds could be identified more easily, but high and thin clouds are well hidden sometimes. This issue would influence the brightness unity of the image. The images with a clear unbalanced brightness are removed from the database.

3. For the images with very close appearances, that the identifiable items on the solar disk do not have observable changes, the clearest one is selected. If the items like active regions and filaments are close to the limb where it is darker than the solar center, then evaluate the corresponding "fr" image to check if the items are clear. The images with a very close appearance but less clearness are also removed from the database.

Finally, about 400-500 images could be left for every year's data. Doing such a selection is to unify the quality of the images in the deep learning algorithm.

Experimental results demonstrate the good performance of the proposed method. To our knowledge, this is the first time that deep learning has been used to generate photospheric vector magnetograms of solar active regions. With this **MagNet** and the LOS magnetogram provided by Michelson Doppler Imager (MDI) on board the Solar and Heliospheric Observatory (SOHO), we can expand the availability of vector magnetograms to the period from 1996 to the present.

3.6 Future Work: Data-driving MHD Simulation

This undergoing study aims to numerically drive the eruption of the X5.4 flare of AR11429 and the NLFFF extrapolation of the $hmi.sharp.cea\_720s$ magnetogram as the initiation condition.

The Data-driving MHD simulation are basically according to following equations:

$$\frac{\partial \rho}{\partial t} = -\nabla \cdot (\rho \boldsymbol{v}) \tag{3.2}$$

$$\frac{\partial \boldsymbol{v}}{\partial t} = -(\boldsymbol{v} \cdot \nabla)\boldsymbol{v} + \frac{1}{\rho}\boldsymbol{J} \times \boldsymbol{B} + \nu\nabla^2\boldsymbol{v} \tag{3.3}$$

$$\frac{\partial \boldsymbol{B}}{\partial t} = \nabla \times (\boldsymbol{v} \times \boldsymbol{B}) + \eta\nabla^2\boldsymbol{B} - \nabla\phi \tag{3.4}$$

$$\boldsymbol{J} = \nabla \times \boldsymbol{B} \tag{3.5}$$

$$\frac{\partial \phi}{\partial t} + c_h^2 \nabla \cdot \boldsymbol{B} = -\frac{c_h^2}{c_p^2}\phi \tag{3.6}$$

where the ρ is plasma density, $\boldsymbol{B}$ is the magnetic flux density, $\boldsymbol{v}$ is the velocity, $\boldsymbol{J}$ is the electric current density, and ϕ is the convenient potential to remove errors derived from $\nabla \cdot \boldsymbol{B}$ [23].

The NLFFF is performed with the weighted optimization method [135] with preprocessing [137] at 22:22 UT, 6 March 2012, which is $\sim$ 2 h before the X5.4 flare.

3.6.1 Current Results

In order to trigger the flare, an anonymous resistivity is introduced to the simulation in terms of the turbulence of $\boldsymbol{J}$ at the bottom boundary of the initiation condition. The value and the range of the application of $\boldsymbol{J}$ depend on the NLFFF results. Figure 3.28 shows the NLFFF results and the $|J|$ distribution on the photosphere.
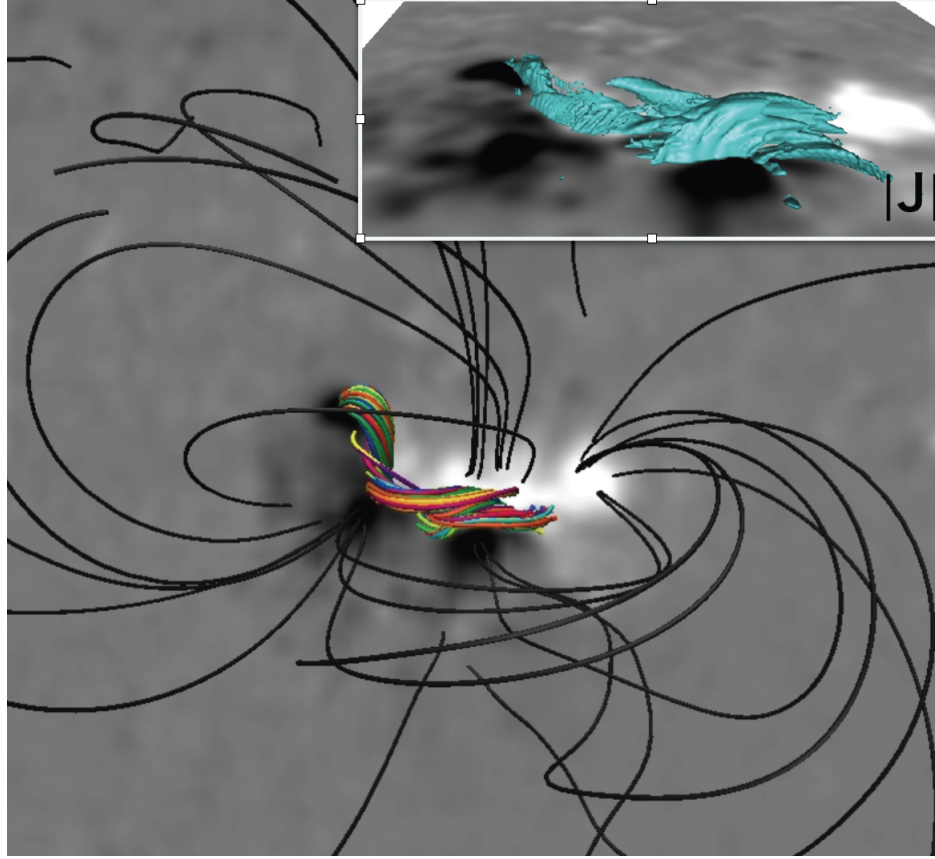
Figure 3.26 Simulation of the magnetic field and current density. The magnetic field lines and the MFR in the core region (colored) of the NLFFF as the initiation condition of the simulation. The isosurface of the $\boldsymbol{J}$ is 0.03 A/M^2

So far, we have tried the simulation with anonymous resistivity applied in the restricted area of the region of interest in the Initiation and Back-reaction Study. Equation 3.7 shows the expression of the $\boldsymbol{J}$ turbulence:

$$\eta = 10^{-5} + 5 \times 10^{-4} \times \left(\frac{J - J_{cri}}{J_{cri}}\right)^2 \tag{3.7}$$

where $J_{cri} = 0.03$ is the threshold to determine the area of anonymous resistivity, and η is the electrical conductivity. Unfortunately, this attempt failed to make an eruption. Thus we remove the limit of the area that applies the anonymous resistivity, and we successfully triggered a flare.

3.6.2 Future Plans

Even though we numerically derived a flare eruption, many questions still don't have a proper answer except for the fact that this AR is fully energized and very flare productive. One successful simulation doesn't answer the questions of "when", "where" and "how" the solar flares.

In future work, we are proposed to do a series of simulations based on the different magnetic field evolution statuses. The steps are briefly described here:

1. Use the relaxation code to drive the magnetic field evolution without triggering anonymous resistivity.

2. Select candidate initiation conditions from the relaxation code results to derive eruptions with anonymous resistivity ("when").

3. Repeat the last step with different turbulence areas ("where").

4. Initiation analysis of successful simulations and compare with observations ("how").

CHAPTER 4

SUMMARY

This dissertation presents four innovative studies regarding the initiation mechanism and evolution of flare eruptions. The M6.5 flare in AR12371 and the X5.4 flare in AR 11429 have been well analyzed with multi-wavelength data processed by various analyzing methods.

Specifically, in the statistical study including 38 flare events, we find that the TI plays an important role in distinguishing eruptive and confined events, but the KI is not a major factor in the type of eruptions. It is the first time to use real event observations to study the role played by MHD instabilities in the CME association with solar flares. This study also shows the difference between the observational result for solar eruptions with that of the laboratory result in terms of the role played by magnetic reconnection.

In the multi-instrument precursor study, we quantitatively analyzed the variation of thermal parameters (i.e, temperature T, emission measure EM, and number density n) at the precursor phase of the M6.5 flare, measured by multi instruments operating at different wavelength regimes with different emission mechanisms. The uniqueness of this study is that it presents a comprehensive thermal analysis, in terms of both spectrum wavelengths and the variety of thermal parameters, of flare precursors which share the same magnetic field conditions with their subsequent events.

In the Initiation and Back-reaction Study, we investigate the 3D magnetic structure and MHD kink instability (KI), torus instability (TI), and double arc instability (DAI), and conclude that the X5.4 in AR 11429 flare is most likely triggered by the tether-cutting reconnection and the subsequent DAI. We also find clear back-reactions in both NLFFF and Non-FFF in terms of an increase of horizontal

magnetic field (B_h) and a decrease of inclination angle (Φ) of the magnetic field near the PIL. In addition, the Non-FFF model shows an enhancement of the downward Lorentz force acting on the photosphere, and the location of the enhancement spatially coincides with the location of the flare onset. To the best of our knowledge, it is the first application of Non-FFF in the calculation of Lorentz force in back-reaction studies. This study draws a clear picture of how the magnetic field evolution could lead to a flare eruption and the other way around, the influence of the occurrence of solar eruptions on magnetic field changes. From another field of view, this study helps us understand the evolution of ARs, especially the highly flare productive ones.

In the light-bridges study, we investigated the three-dimensional (3D) magnetic structure of the two light bridges over the sunspots in AR 12371. High-resolution magnetogram analysis shows the fine structure of enhanced electric currents and magnetic shear in greater detail. The 3D NLFFF model shows a low-lying 3D magnetic canopy as well as a 3D current system. The highlight of this study is the application of the high-resolution which is the most visual picture of the magnetic canopy obtained by observation to date.

In addition, a joint study with computer science researchers aiming at generating photospheric vector magnetograms using deep learning tools is partially included. In the end, We briefly introduce an undergoing study aiming to numerically drive the eruption of the X5.4 flare of AR11429 and our future plans. We also introduce the cyberinfrastructure for advancing space weather research named SolarDB and its flare database.

This dissertation presents a systematical study of the magnetic field evolution and flare initiation-related topics. Combining the multi-wavelength thermal analysis in the initiation phase of the flare and a more realistic magnetic field boundary condition with the presence of Lorentz force, the potential of this dissertation may lead to the development of more advanced modeling techniques.

APPENDIX

LIST OF 38 EVENTS IN STATISTICAL STUDY

This list of 38 event consists of 26 ejective flares and 12 confined flares selected in the statistical study in Section 3.1. See Jing et al., 2018[57] for more detailed information of the flares in this list.

Table A.1 Event List

No.	SXR Peak Time	Class	AR	Position	Type[a]	n[b]	$|T_w|$[c]
1	SOL2011-02-13T17:38	M6.6	11158	S20E04	E	0.58 ± 0.16	0.39 ± 0.03
2	SOL2011-02-15T01:56	X2.2	11158	S20W10	E	0.86 ± 0.46	0.62 ± 0.04
3	SOL2011-03-09T23:23	X1.5	11166	N08W09	C	0.62 ± 0.04	0.73 ± 0.21
4	SOL2011-07-30T02:09	M9.3	11261	S20W10	C	0.45 ± 0.12	0.47 ± 0.14
5	SOL2011-08-03T13:48	M6.0	11261	N16W30	E	1.28 ± 0.12	0.73 ± 0.16
6	SOL2011-09-06T01:50	M5.3	11283	N14W07	E	0.86 ± 0.14	0.63 ± 0.09
7	SOL2011-09-06T22:20	X2.1	11283	N14W18	E	0.98 ± 0.33	0.98 ± 0.20
8	SOL2011-10-02T00:50	M3.9	11305	N12W26	C	0.63 ± 0.08	0.55 ± 0.09
9	SOL2012-01-23T03:59	M8.7	11402	N28W21	E	0.79 ± 0.11	1.08 ± 0.20
10	SOL2012-03-07T00:24	X5.4	11429	N17E31	E	0.89 ± 0.11	0.62 ± 0.06
11	SOL2012-03-09T03:53	M6.3	11429	N15W03	E	0.78 ± 0.09	0.78 ± 0.15
12	SOL2012-07-02T10:52	M5.6	11515	S17E08	E	0.60 ± 0.18	1.44 ± 0.16
13	SOL2012-07-12T16:49	X1.4	11520	S15W01	E	0.51 ± 0.06	0.81 ± 0.09
14	SOL2013-04-11T07:16	M6.5	11719	N09E12	E	0.61 ± 0.12	0.92 ± 0.17
15	SOL2013-10-24T00:30	M9.3	11877	S09E10	E	0.18 ± 0.20	0.99 ± 0.12
16	SOL2013-11-01T19:53	M6.3	11884	S12E01	C	0.70 ± 0.23	1.15 ± 0.21
17	SOL2013-11-03T05:22	M4.9	11884	S12W17	C	0.53 ± 0.12	0.81 ± 0.14

Table A.1 Event List (Continued)

No.	SXR Peak Time	Class	AR	Position	Type	n	$|T_w|$
18	SOL2013-11-05T22:12	X3.3	11890	S12E44	E	0.31 ± 0.18	0.54 ± 0.14
19	SOL2013-11-08T04:26	X1.1	11890	S12E13	E	0.28 ± 0.19	0.59 ± 0.08
20	SOL2014-01-07T18:32	X1.2	11944	S15W11	E	0.61 ± 0.07	0.84 ± 0.15
21	SOL2014-02-02T09:31	M4.4	11967	S10E13	C	0.43 ± 0.05	0.66 ± 0.09
22	SOL2014-02-04T04:00	M5.2	11967	S14W06	C	0.67 ± 0.09	0.67 ± 0.11
23	SOL2014-03-29T17:48	X1.1	12017	N10W32	E	0.73 ± 0.19	1.26 ± 0.09
24	SOL2014-04-18T13:03	M7.3	12036	S20W34	E	1.07 ± 0.10	0.75 ± 0.12
25	SOL2014-09-10T17:45	X1.6	12158	N11E05	E	0.42 ± 0.06	0.49 ± 0.09
26	SOL2014-10-22T14:28	X1.6	12192	S14E13	C	0.22 ± 0.04	0.72 ± 0.03
27	SOL2014-10-24T21:41	X3.1	12192	S22W21	C	0.70 ± 0.08	0.97 ± 0.26
28	SOL2014-11-07T17:26	X1.6	12205	N17E40	E	0.66 ± 0.13	1.03 ± 0.11
29	SOL2014-12-04T18:25	M6.1	12222	S20W31	C	0.56 ± 0.10	1.05 ± 0.17
30	SOL2014-12-17T04:51	M8.7	12242	S18E08	E	1.34 ± 0.10	0.71 ± 0.12
31	SOL2014-12-18T21:58	M6.9	12241	S11E15	E	1.57 ± 0.10	1.08 ± 0.14
32	SOL2014-12-20T00:28	X1.8	12242	S19W29	E	0.65 ± 0.06	0.91 ± 0.09
33	SOL2015-03-12T14:08	M4.2	12297	S15E06	C	0.36 ± 0.15	0.54 ± 0.08
34	SOL2015-06-22T18:23	M6.5	12371	N13W06	E	0.92 ± 0.06	1.14 ± 0.05
35	SOL2015-06-25T08:16	M7.9	12371	N12W40	E	0.74 ± 0.20	0.93 ± 0.07
36	SOL2015-09-28T14:58	M7.6	12422	S20W28	C	0.44 ± 0.13	0.74 ± 0.21
37	SOL2017-09-04T20:33	M5.5	12673	S10W11	E	0.80 ± 0.27	0.70 ± 0.08
38	SOL2017-09-06T12:02	X9.3	12673	S09W34	E	0.63 ± 0.09	0.79 ± 0.14

[a] Flare type: (E)jective or (C)onfined;
[b] Decay index with $\pm 1\sigma$ uncertainty calculated over the FPIL mask;
[c] Twist number with $\pm 1\sigma$ uncertainty calculated over the NLFF field lines forming the MFRs.

REFERENCES

[1] V. E. Abramov-Maximov, V. N. Borovik, L. V. Opeikina, and A. G. Tlatov. Precursors of the solar X flare on march 29, 2014, in the active region NOAA 12017 based on microwave radiation and magnetographic data. *Geomagnetism and Aeronomy*, 55(8):1097–1103, 2015.

[2] T. Amari, J. F. Luciani, Z. Mikic, and J. Linker. A twisted flux rope model for coronal mass ejections and two-ribbon flares. *The Astrophysical Journal Letters*, 529:L49–L52, January 2000.

[3] S. K. Antiochos, C. R. DeVore, and J. A. Klimchuk. A model for solar coronal mass ejections. *The Astrophysical Journal*, 510(1):485–493, January 1999.

[4] M. J. Aschwanden. The differential emission measure distribution in the multiloop corona. *The Astrophysical Journal*, 580(1):L79–L83, November 2002.

[5] M. J. Aschwanden. Particle acceleration and kinematics in solar flares: a synthesis of recent observations and theoretical concepts (invited review). *Space Science Reviews*, 101(1):1–227, 2002.

[6] A. K. Awasthi, R. Jain, P. D. Gadhiya, M. J. Aschwand en, W. Uddin, A. K. Srivastava, R. Chandra, N. Gopalswamy, N. V. Nitta, S. Yashiro, P. K. Manoharan, D. P. Choudhary, N. C. Joshi, V. C. Dwivedi, and K. Mahalakshmi. Multiwavelength diagnostics of the precursor and main phases of an M1.8 flare on 2011 April 22. *Monthly Notices of the Royal Astronomical Society*, 437(3):2249–2262, January 2014.

[7] Y. Bamba and K. Kusano. Evaluation of Applicability of a Flare Trigger Model Based on a Comparison of Geometric Structures. *The Astrophysical Journal*, 856(1):43, March 2018.

[8] Y. Bamba, K. Lee, S. Imada, and K. Kusano. Study on Precursor Activity of the X1.6 Flare in the Great AR 12192 with SDO, IRIS, and Hinode. *The Astrophysical Journal*, 840(2):116, May 2017.

[9] G. Bateman. *MHD instabilities*. Cambridge, Mass., MIT Press, 1978. 270 p.

[10] H. Baty. On the MHD stability of the vec m = 1 kink mode in solar coronal loops. *Astronomy and Astrophysics*, 367:321–325, February 2001.

[11] J. M. Beckers and E. H. Schröter. The Intensity, velocity and magnetic structure of a sunspot region. IV: properties of a unipolar sunspot. *Solar Physics*, 10(2):384–403, December 1969.

[12] M. A. Berger and C. Prior. The writhe of open and closed curves. *Journal of Physics A Mathematical General*, 39(26):8321–8348, June 2006.

[13] L. Bharti. Fine structure above a light bridge in the transition region and corona. *Monthly Notices of the Royal Astronomical Society*, 452(1):L16–L20, September 2015.

[14] J. C. Brown. The deduction of energy spectra of non-thermal electrons in flares from the observed dynamic spectra of hard x-ray bursts. *Solar Physics*, 18(3):489–502, 1971.

[15] V. Bumba and L. Křivský. Chromospheric pre-flares. *Bulletin of the Astronomical Institutes of Czechoslovakia*, 10:221, January 1959.

[16] G. R. Carruthers. Ultraviolet space astronomy. In Robert A. Meyers, editor, *Encyclopedia of Physical Science and Technology (Third Edition)*, pages 289–315. Academic Press, New York, NY, third edition, 2003.

[17] J. Chen. Effects of toroidal forces in current loops embedded in a background plasma. *The Astrophysical Journal*, 338:453–470, March 1989.

[18] X. Chen, Y. Yan, B. Tan, J. Huang, W. Wang, L. Chen, Y. Zhang, C. Tan, D. Liu, and S. Masuda. Quasi-periodic Pulsations before and during a Solar Flare in AR 12242. *The Astrophysical Journal*, 878(2):78, June 2019.

[19] M. C. M. Cheung, P. Boerner, C. J. Schrijver, P. Testa, F. Chen, H. Peter, and A. Malanushenko. Thermal Diagnostics with the Atmospheric Imaging Assembly on board the Solar Dynamics Observatory: A Validated Method for Differential Emission Measure Inversions. *The Astrophysical Journal*, 807(2):143, July 2015.

[20] M. C. M. Cheung, M. Rempel, A. M. Title, and M. Schüssler. Simulation of the Formation of a Solar Active Region. *The Astrophysical Journal*, 720(1):233–244, September 2010.

[21] A. R. Choudhuri. The Dynamics of Magnetically Trapped Fluids. I. Implications for Umbral Dots and Penumbral Grains. *The Astrophysical Journal*, 302:809, March 1986.

[22] S. Clark. Astronomical fire: Richard carrington and the solar flare of 1859. *Endeavour*, 31(3):104–109, 2007.

[23] A. Dedner, F. Kemm, D. Kröner, C.-D. Munz, T. Schnitzer, and M. Wesenberg. Hyperbolic divergence cleaning for the mhd equations. *Journal of Computational Physics*, 175(2):645–673, 2002.

[24] P. Démoulin and G. Aulanier. Criteria for flux rope eruption: Non-equilibrium versus torus instability. *The Astrophysical Journal*, 718(2):1388–1399, July 2010.

[25] K. P. Dere, G. E. Brueckner, R. A. Howard, D. J. Michels, and J. P. Delaboudiniere. LASCO and EIT Observations of Helical Structure in Coronal Mass Ejections. *The Astrophysical Journal*, 516:465–474, May 1999.

[26] Y. Fan and S. E. Gibson. Numerical Simulations of Three-dimensional Coronal Magnetic Fields Resulting from the Emergence of Twisted Magnetic Flux Tubes. *The Astrophysical Journal*, 609:1123–1133, July 2004.

[27] T. Felipe, M. Collados, E. Khomenko, C. Kuckein, A. Asensio Ramos, H. Balthasar, T. Berkefeld, C. Denker, A. Feller, M. Franz, A. Hofmann, J. Joshi, C. Kiess, A. Lagg, H. Nicklas, D. Orozco Suárez, A. Pastor Yabar, R. Rezaei, R. Schlichenmaier, D. Schmidt, W. Schmidt, M. Sigwarth, M. Sobotka, S. K. Solanki, D. Soltau, J. Staude, K. G. Strassmeier, R. Volkmer, O. von der Lühe, and T. Waldmann. Three-dimensional structure of a sunspot light bridge. *Astronomy and Astrophysics*, 596:A59, November 2016.

[28] F. Fernandes, R. Cunha-Silva, M. Galdino, and Z. Sodré. Radio Emissions Precursors of Impulsive Phase of Solar Flares Recorded by CALLISTO-BR. In *41st COSPAR Scientific Assembly*, volume 41, pages S.1–19–16, July 2016.

[29] G. H. Fisher, D. J. Bercik, B. T. Welsch, and H. S. Hudson. Global forces in eruptive solar flares: The lorentz force acting on the solar atmosphere and the solar interior. *Solar Physics*, 277(1):59–76, 2012.

[30] G. D. Fleishman, S. Anfinogentov, M. Loukitcheva, I. Mysh'yakov, and A. Stupishin. Casting the Coronal Magnetic Field Reconstruction Tools in 3D Using the MHD Bifrost Model. *The Astrophysical Journal*, 839:30, April 2017.

[31] G. D. Fleishman and A. Kuznetsov. Fast gyrosynchrotron codes. *The Astrophysical Journal*, 721:1127, 09 2010.

[32] G. D. Fleishman, G. M. Nita, and D. E. Gary. New interactive solar flare modeling and advanced radio diagnostics tools. *Proceedings of the International Astronomical Union*, 6(S274):280–283, 2010.

[33] G. D. Fleishman, G. M. Nita, and D. E. Gary. Energy partitions and evolution in a purely thermal solar flare. *The Astrophysical Journal*, 802(2):122, April 2015.

[34] J. I. Garcia de La Rosa. Umbral Dots - a Case of Penetrative Convection Between Sunspot Fragments. *Solar Physics*, 112(1):49–58, March 1987.

[35] D. E. Gary, B. Chen, B. R. Dennis, G. D. Fleishman, G. J. Hurford, S. Krucker, J. M. McTiernan, G. M. Nita, A. Y. Shih, S. M. White, and S. Yu. Microwave and hard x-ray observations of the 2017 september 10 solar limb flare. *The Astrophysical Journal*, 863(1):83, August 2018.

[36] D. E. Gary, G. D. Fleishman, and G. M. Nita. Magnetography of solar flaring loops with microwave imaging spectropolarimetry. *Solar Physics*, 288(2):549–565, 2013.

[37] D. E. Gary and G. J. Hurford. Coronal Temperature, Density, and Magnetic Field Maps of a Solar Active Region Using the Owens Valley Solar Array. *The Astrophysical Journal*, 420:903, January 1994.

[38] N. Gopalswamy, S. Yashiro, S. Akiyama, and H. Xie. Estimation of Reconnection Flux Using Post-eruption Arcades and Its Relevance to Magnetic Clouds at 1 AU. *Solar Physics*, 292:65, April 2017.

[39] N. Gopalswamy, S. Yashiro, G. Michalek, G. Stenborg, A. Vourlidas, S. Freeland, and R. Howard. The SOHO/LASCO CME Catalog. *Earth Moon and Planets*, 104:295–313, April 2009.

[40] S. Gosain. Evidence for collapsing fields in the corona and photosphere during the 2011 February 15 x2.2 flare:iSDO/i/AIA and HMI observations. *The Astrophysical Journal*, 749(1):85, March 2012.

[41] L. M. Green, T. Török, B. Vršnak, W. Manchester, and A. Veronig. The origin, early evolution and predictability of solar eruptions. *Space Science Reviews*, 214(1):46, 2018.

[42] A. B. Griñón-Marín, A. Pastor Yabar, R. Centeno, and H. Socas-Navarro. Long-term evolution of three light bridges developed on the same sunspot. *Astronomy and Astrophysics*, 647:A148, March 2021.

[43] N. Gyenge, I. Ballai, and T. Baranyi. Statistical study of spatio-temporal distribution of precursor solar flares associated with major flares. *Monthly Notices of the Royal Astronomical Society*, 459(4):3532–3539, 04 2016.

[44] A. Hernandez-Perez, Y. Su, A. M. Veronig, J. Thalmann, P. Gömöry, and B. Joshi. Pre-eruption Processes: Heating, Particle Acceleration, and the Formation of a Hot Channel before the 2012 October 20 M9.0 Limb Flare. *The Astrophysical Journal*, 874(2):122, April 2019.

[45] S. M. Hill, V. J. Pizzo, C. C. Balch, D. A. Biesecker, P. Bornmann, E. Hildner, L. D. Lewis, R. N. Grubb, M. P. Husler, K. Prendergast, J. Vickroy, S. Greer, T. Defoor, D. C. Wilkinson, R. Hooker, P. Mulligan, E. Chipman, H. Bysal, J. P. Douglas, R. Reynolds, J. M. Davis, K. S. Wallace, K. Russell, K. Freestone, D. Bagdigian, T. Page, S. Kerns, R. Hoffman, S. A. Cauffman, M. A. Davis, R. Studer, F. E. Berthiaume, T. T. Saha, G. D. Berthiume, H. Farthing, and F. Zimmermann. The noaa goes-12 solar x-ray imager (sxi) 1. instrument, operations, and data. *Solar Physics*, 226(2):255–281, 2005.

[46] J. Hirzberger, J. A. Bonet, M. Sobotka, M. Vázquez, and A. Hanslmeier. Fine structure and dynamics in a light bridge inside a solar pore. *Astronomy and Astrophysics*, 383:275–282, January 2002.

[47] G. Van Hoven and G.J. Hurford. Solar flare precursors. *Advances in Space Research*, 6(6):83 – 91, 1986.

[48] Q. Hu and B. Dasgupta. An Improved Approach to Non-Force-Free Coronal Magnetic Field Extrapolation. *Solar Physics*, 247(1):87–101, January 2008.

[49] Q. Hu, B. Dasgupta, D. P. Choudhary, and J. Büchner. A practical approach to coronal magnetic field extrapolation based on the principle of minimum dissipation rate. *The Astrophysical Journal*, 679(1):848–853, May 2008.

[50] Q. Hu, B. Dasgupta, M.L. DeRosa, J. Büchner, and G.A. Gary. Non-force-free extrapolation of solar coronal magnetic field using vector magnetograms. *Journal of Atmospheric and Solar-Terrestrial Physics*, 72(2):219–223, 2010.

[51] Q. Hu and Brahmananda Dasgupta. A new approach to modeling non-force free coronal magnetic field. *Geophysical Research Letters - GEOPHYS RES LETT*, 331, 08 2006.

[52] H. S. Hudson. Global properties of solar flares. *Space Science Reviews*, 158(1):5–41, 2011.

[53] H. S. Hudson, G. H. Fisher, and B. T. Welsch. Flare Energy and Magnetic Field Variations. In R. Howe, R. W. Komm, K. S. Balasubramaniam, and G. J. D. Petrie, editors, *Subsurface and Atmospheric Influences on Solar Activity*, volume 383 of *Astronomical Society of the Pacific Conference Series*, page 221, January 2008.

[54] G. J. Hurford, R. B. Read, and H. Zirin. A frequency-agile interferometer for solar microwave spectroscopy. *Solar Physics*, 94(2):413–426, 1984.

[55] G. J. Hurford, E. J. Schmahl, R. A. Schwartz, A. J. Conway, M. J. Aschwanden, A. Csillaghy, B. R. Dennis, C. Johns-Krull, S. Krucker, R. P. Lin, J. Mctiernan, T. R. Metcalf, J. Sato, and D. M. Smith. *The RHESSI Imaging Concept*, pages 61–86. Springer Netherlands, Dordrecht, 2003.

[56] N. Ishiguro and K. Kusano. Double arc instability in the solar corona. *The Astrophysical Journal*, 843(2):101, July 2017.

[57] J. Jing, C. Liu, J. Lee, H. Ji, N. Liu, Y. Xu, and H. Wang. Statistical analysis of torus and kink instabilities in solar eruptions. *The Astrophysical Journal*, 864(2):138, September 2018.

[58] J. Jing, R. Liu, M. C. M. Cheung, J. Lee, Y. Xu, C. Liu, C. Zhu, and H. Wang. Witnessing a large-scale slipping magnetic reconnection along a dimming channel during a solar flare. *The Astrophysical Journal*, 842(2):L18, June 2017.

[59] J. Jing, Y. Xu, W. Cao, C. Liu, D. Gary, and H. Wang. Unprecedented Fine Structure of a Solar Flare Revealed by the 1.6 m New Solar Telescope. *Scientific Reports*, 6:24319, April 2016.

[60] J. Jurčák, V. Martínez Pillet, and M. Sobotka. The magnetic canopy above light bridges. *Astronomy and Astrophysics*, 453(3):1079–1088, July 2006.

[61] B. Kliem and T. Török. Torus instability. *Physical Review Letters*, 96(25), June 2006.

[62] M. R. Kundu, S. M. White, K. Shibasaki, T. Sakurai, and V. V. Grechnev. Spatial structure of simple spiky bursts at microwave/millimeter wavelengths. *The Astrophysical Journal*, 547(2):1090–1099, February 2001.

[63] K. Kusano, Y. Bamba, T. T. Yamamoto, Y. Iida, S. Toriumi, and A. Asai. Magnetic Field Structures Triggering Solar Flares and Coronal Mass Ejections. *The Astrophysical Journal*, 760(1):31, November 2012.

[64] K. Kusano, T. Iju, Y. Bamba, and S. Inoue. A physics-based method that can predict imminent large solar flares. *Science*, 369(6503):587–591, 2020.

[65] A. Lagg, S. K. Solanki, M. van Noort, and S. Danilovic. Vigorous convection in a sunspot granular light bridge. *Astronomy and Astrophysics*, 568:A60, August 2014.

[66] J. Lee. *Electron Transport During Solar Flares*, pages 179–202. Springer Netherlands, Dordrecht, 2005.

[67] J. Lee, D. E. Gary, J. Qiu, and P. T. Gallagher. Electron transport during the 1999 august 20 flare inferred from microwave and hard x-ray observations. *The Astrophysical Journal*, 572(1):609–625, June 2002.

[68] J. Lee and Dale E. Gary. Solar microwave bursts and injection pitch-angle distribution of flare electrons. *The Astrophysical Journal*, 543(1):457–471, November 2000.

[69] K. D. Leka. The Vector Magnetic Fields and Thermodynamics of Sunspot Light Bridges: The Case for Field-free Disruptions in Sunspots. *The Astrophysical Journal*, 484(2):900–919, July 1997.

[70] D. Li, S. Feng, W. Su, and Y. Huang. Preflare very long-periodic pulsations observed in Hα emission before the onset of a solar flare. *Astronomy and Astrophysics*, 639:L5, July 2020.

[71] D. Li, L. Lu, Z. Ning, L. Feng, W. Gan, and H. Li. Quasi-periodic Pulsation Detected in Lyα Emission During Solar Flares. *The Astrophysical Journal*, 893(1):7, April 2020.

[72] E. Lim, H. Yang, V. Yurchyshyn, J. Chae, D. Song, and M. S. Madjarska. Detection of Opposite Magnetic Polarity in a Light Bridge: Its Emergence and Cancellation in Association with LB Fan-shaped Jets. *The Astrophysical Journal*, 904(2):84, December 2020.

[73] J. Lin. Energetics and propagation of coronal mass ejections in different plasma environments. *Chinese Journal of Astronomy and Astrophysics*, 2(6):539–556, December 2002.

[74] R. P. Lin, B. R. Dennis, G. J. Hurford, D. M. Smith, A. Zehnder, P. R. Harvey, D. W. Curtis, D. Pankow, P. Turin, M. Bester, A. Csillaghy, M. Lewis, N. Madden, H. F. van Beek, M. Appleby, T. Raudorf, J. McTiernan,

R. Ramaty, E. Schmahl, R. Schwartz, S. Krucker, R. Abiad, T. Quinn, P. Berg, M. Hashii, R. Sterling, R. Jackson, R. Pratt, R. D. Campbell, D. Malone, D. Landis, C. P. Barrington-Leigh, S. Slassi-Sennou, C. Cork, D. Clark, D. Amato, L. Orwig, R. Boyle, I. S. Banks, K. Shirey, A. K. Tolbert, D. Zarro, F. Snow, K. Thomsen, R. Henneck, A. Mchedlishvili, P. Ming, M. Fivian, John Jordan, Richard Wanner, Jerry Crubb, J. Preble, M. Matranga, A. Benz, H. Hudson, R. C. Canfield, G. D. Holman, C. Crannell, T. Kosugi, A. G. Emslie, N. Vilmer, J. C. Brown, C. Johns-Krull, M. Aschwanden, T. Metcalf, and A. Conway. The reuven ramaty high-energy solar spectroscopic imager (rhessi). *Solar Physics*, 210(1):3–32, 2002.

[75] R. P. Lin, B. R. Dennis, G. J. Hurford, D. M. Smith, A. Zehnder, P. R. Harvey, D. W. Curtis, D. Pankow, P. Turin, M. Bester, A. Csillaghy, M. Lewis, N. Madden, H. F. van Beek, M. Appleby, T. Raudorf, J. Mctiernan, R. Ramaty, E. Schmahl, R. Schwartz, S. Krucker, R. Abiad, T. Quinn, P. Berg, M. Hashii, R. Sterling, R. Jackson, R. Pratt, R. D. Campbell, D. Malone, D. Landis, C. P. Barrington-Leigh, S. Slassi-Sennou, C. Cork, D. Clark, D. Amato, L. Orwig, R. Boyle, I. S. Banks, K. Shirey, A. K. Tolbert, D. Zarro, F. Snow, K. Thomsen, R. Henneck, A. Mchedlishvili, P. Ming, M. Fivian, John Jordan, Richard Wanner, Jerry Crubb, J. Preble, M. Matranga, A. Benz, H. Hudson, R. C. Canfield, G. D. Holman, C. Crannell, T. Kosugi, A. G. Emslie, N. Vilmer, J. C. Brown, C. Johns-Krull, M. Aschwanden, T. Metcalf, and A. Conway. *The Reuven Ramaty High-Energy Solar Spectroscopic Imager (Rhessi)*, pages 3–32. Springer Netherlands, Dordrecht, 2003.

[76] B. W. Lites, T. A. Bida, A. Johannesson, and G. B. Scharmer. High-Resolution Spectra of Solar Magnetic Features. II. Magnetic Fields of Umbral Brightenings. *The Astrophysical Journal*, 373:683, June 1991.

[77] C. Liu, N. Deng, J. Lee, T. Wiegelmann, R. L. Moore, and H. Wang. Evidence for solar tether-cutting magnetic reconnection from coronal field extrapolations. *The Astrophysical Journal*, 778(2):L36, November 2013.

[78] C. Liu, J. Lee, D. E. Gary, and H. Wang. The ribbon-like hard x-ray emission in a sigmoidal solar active region. *The Astrophysical Journal*, 658(2):L127–L130, February 2007.

[79] C. Liu, Y. Xu, W. Cao, N. Deng, J. Lee, H. S. Hudson, D. E. Gary, J. Wang, J. Jing, and H. Wang. Flare differentially rotates sunspot on Sun's surface. *Nature Communications*, 7:13104, October 2016.

[80] H. Liu, Y. Xu, J. Wang, J. Jing, C. Liu, J. T. L. Wang, and H. Wang. Inferring vector magnetic fields from stokes profiles of GST/NIRIS using a convolutional neural network. *The Astrophysical Journal*, 894(1):70, May 2020.

[81] R. Liu, B. Kliem, V. S. Titov, J. Chen, Y. Wang, H. Wang, C. Liu, Y. Xu, and T. Wiegelmann. Structure stability and evolution of magnetic flux ropes from

the perspective of magnetic twist. *The Astrophysical Journal*, 818(2):148, February 2016.

[82] R. Liu, C. Liu, S. Wang, N. Deng, and H. Wang. Sigmoid-to-flux-rope Transition Leading to a Loop-like Coronal Mass Ejection. *The Astrophysical Journal Letters*, 725:L84–L90, December 2010.

[83] G. Livadiotis and D. J. McComas. Understanding kappa distributions: A toolbox for space science and astrophysics. *Space Science Reviews*, 175(1):183–214, 2013.

[84] R. E. Louis, L. R. Bellot Rubio, J. de la Cruz Rodríguez, H. Socas-Navarro, and A. Ortiz. Small-scale magnetic flux emergence in a sunspot light bridge. *Astronomy and Astrophysics*, 584:A1, December 2015.

[85] R. E. Louis, A. Prasad, C. Beck, D. P. Choudhary, and M. S. Yalim. Heating of the solar chromosphere in a sunspot light bridge by electric currents. *Astronomy and Astrophysics*, 652:L4, August 2021.

[86] B. C. Low. Magnetohydrodynamic processes in the solar corona: Flares, coronal mass ejections, and magnetic helicity. *Physics of Plasmas*, 1:1684–1690, May 1994.

[87] P. MacNeice, S. K. Antiochos, A. Phillips, D. S. Spicer, C. R. DeVore, and K. Olson. A numerical study of the breakout model for coronal mass ejection initiation. *The Astrophysical Journal*, 614(2):1028–1041, October 2004.

[88] S. Martin. Preflare conditions, changes and events. *Solar Physics*, 68:217–236, 12 1980.

[89] R. L. Moore, A. C. Sterling, H. S. Hudson, and J. R. Lemen. Onset of the magnetic explosion in solar flares and coronal mass ejections. *The Astrophysical Journal*, 552(2):833–848, May 2001.

[90] J. Muhamad, K. Kusano, S. Inoue, and Y. Bamba. A study of magnetic field characteristics of the flaring active region based on nonlinear force-free field extrapolation. *The Astrophysical Journal*, 863(2):162, August 2018.

[91] J. Muhamad, K. Kusano, S. Inoue, and D. Shiota. Magnetohydrodynamic simulations for studying solar flare trigger mechanism. *The Astrophysical Journal*, 842(2):86, June 2017.

[92] C. E. Myers, M. Yamada, H. Ji, J. Yoo, W. Fox, J. Jara-Almonte, A. Savcheva, and E. E. Deluca. A dynamic magnetic tension force as the cause of failed solar eruptions. *Nature*, 528:526–529, December 2015.

[93] G. M. Nita, G. D. Fleishman, A. A. Kuznetsov, E. P. Kontar, and D. E. Gary. Three-dimensional radio and x-ray modeling and data analysis software: Revealing flare complexity. *The Astrophysical Journal*, 799(2):236, February 2015.

[94] E. N. Parker. Sunspots and the physics of magnetic flux tubes. IX. Umbral dots and longitudinal overstability. *The Astrophysical Journal*, 234:333–347, November 1979.

[95] G. J. D. Petrie. The abrupt changes in the photospheric magnetic and lorentz force vectors during six major neutral-line flares. *The Astrophysical Journal*, 759(1):50, October 2012.

[96] G. J. D. Petrie. Abrupt changes in the photospheric magnetic field, lorentz force, and magnetic shear during 15 x-class flares. *The Astrophysical Journal Supplement Series*, 240(1):11, January 2019.

[97] V. J. Pizzo, S. M. Hill, C. C. Balch, D. A. Biesecker, P. Bornmann, E. Hildner, R. N. Grubb, E. G. Chipman, J. M. Davis, K. S. Wallace, K. Russell, S. A. Cauffman, T. T. Saha, and G. D. Berthiume. The noaa goes-12 solar x-ray imager (sxi) 2. performance. *Solar Physics*, 226(2):283–315, 2005.

[98] A. Prasad, R. Bhattacharyya, and Sanjay Kumar. Magnetohydrodynamic modeling of solar coronal dynamics with an initial non-force-free magnetic field. *The Astrophysical Journal*, 840(1):37, May 2017.

[99] J. Qiu, Q. Hu, T. A. Howard, and V. B. Yurchyshyn. On the Magnetic Flux Budget in Low-Corona Magnetic Reconnection and Interplanetary Coronal Mass Ejections. *The Astrophysical Journal*, 659:758–772, April 2007.

[100] M. Rempel. Penumbral Fine Structure and Driving Mechanisms of Large-scale Flows in Simulated Sunspots. *The Astrophysical Journal*, 729(1):5, March 2011.

[101] M. Rempel, M. Schüssler, and M. Knölker. Radiative Magnetohydrodynamic Simulation of Sunspot Structure. *The Astrophysical Journal*, 691(1):640–649, January 2009.

[102] C. Robustini, J. Leenaarts, J. de la Cruz Rodriguez, and L. Rouppe van der Voort. Fan-shaped jets above the light bridge of a sunspot driven by reconnection. *Astronomy and Astrophysics*, 590:A57, May 2016.

[103] I. Rueedi, S. K. Solanki, and W. Livingston. Infrared lines as probes of solar magnetic features. XI. Structure of a sunspot umbra with a light bridge. *Astronomy and Astrophysics*, 302:543, October 1995.

[104] K. Shibata. Theories of eruptive flares. *Proceedings of the International Astronomical Union*, 2004(IAUS226):241–249, 2004.

[105] T. Shimizu. Long-term Evolution of Magnetic and Dynamical Properties in A Sunspot Light Bridge. *The Astrophysical Journal*, 738(1):83, September 2011.

[106] A. V. R. Silva, Haimin Wang, and Dale E. Gary. Correlation of microwave and hard x-ray spectral parameters. *The Astrophysical Journal*, 545(2):1116–1123, December 2000.

[107] H. Q. Song, J. Zhang, Y. Chen, and X. Cheng. Direct Observations of Magnetic Flux Rope Formation during a Solar Coronal Mass Ejection. *The Astrophysical Journal Letters*, 792:L40, September 2014.

[108] T. J. Spirock, V. B. Yurchyshyn, and H. Wang. Rapid changes in the longitudinal magnetic field related to the 2001 april 2 x20 flare. *The Astrophysical Journal*, 572(2):1072–1076, June 2002.

[109] H. C. Spruit and G. B. Scharmer. Fine structure, magnetic field and heating of sunspot penumbrae. *Astronomy and Astrophysics*, 447(1):343–354, February 2006.

[110] A. C. Sterling, R. L. Moore, and L. K. Harra. Lateral Offset of the Coronal Mass Ejections from the X-flare of 2006 December 13 and Its Two Precursor Eruptions. *The Astrophysical Journal*, 743(1):63, December 2011.

[111] X. Sun, J. Todd Hoeksema, Y. Liu, T. Wiegelmann, K. Hayashi, Q. Chen, and J. Thalmann. Evolution of magnetic field and energy in a major eruptive active region based oniSDO/i/HMI observation. *The Astrophysical Journal*, 748(2):77, March 2012.

[112] B. Tan, Z. Yu, J. Huang, C. Tan, and Y. Zhang. Very Long-period Pulsations before the Onset of Solar Flares. *The Astrophysical Journal*, 833(2):206, December 2016.

[113] R. StarrC. J. Thomas, R. J.; Crannell. Expressions to determine temperatures and emission measures for solar x-ray events from goes measurements. *Solar Physics*, 95:323–329, Feb 1985.

[114] H. Tian, V. Yurchyshyn, H. Peter, S. K. Solanki, P. R. Young, L. Ni, W. Cao, K. Ji, Y. Zhu, J. Zhang, T. Samanta, Y. Song, J. He, L. Wang, and Y. Chen. Frequently Occurring Reconnection Jets from Sunspot Light Bridges. *The Astrophysical Journal*, 854(2):92, February 2018.

[115] S. Toriumi, M. C. M. Cheung, and Y. Katsukawa. Light Bridge in a Developing Active Region. II. Numerical Simulation of Flux Emergence and Light Bridge Formation. *The Astrophysical Journal*, 811(2):138, October 2015.

[116] S. Toriumi, Y. Katsukawa, and M. C. M. Cheung. Light Bridge in a Developing Active Region. I. Observation of Light Bridge and its Dynamic Activity Phenomena. *The Astrophysical Journal*, 811(2):137, October 2015.

[117] T. Török and B. Kliem. The evolution of twisting coronal magnetic flux tubes. *A&A*, 406(3):1043–1059, 2003.

[118] T. Török, B. Kliem, and V. S. Titov. Ideal kink instability of a magnetic loop equilibrium. *Astronomy &amp Astrophysics*, 413(3):L27–L30, January 2004.

[119] A. A. van Ballegooijen and P. C. H. Martens. Formation and eruption of solar prominences. *The Astrophysical Journal*, 343:971–984, August 1989.

[120] M. Vazquez. A Morphological Study of the Light-Bridges in Sunspots. *Solar Physics*, 31(2):377–387, August 1973.

[121] A. Veronig, J. Brown, B. Dennis, R. Schwartz, L. Sui, and Tolbert. Physics of the neupert effect: Estimates of the effects of source energy, mass transport, and geometry using rhessi and goes data. *The Astrophysical Journal*, 621:482, 12 2008.

[122] A. Vourlidas, R. A. Howard, E. Esfandiari, S. Patsourakos, S. Yashiro, and G. Michalek. Comprehensive Analysis of Coronal Mass Ejection Mass and Energy Properties Over a Full Solar Cycle. *The Astrophysical Journal*, 722:1522–1538, October 2010.

[123] H. Wang. Rapid changes of photospheric magnetic fields around flaring magnetic neutral lines. *The Astrophysical Journal*, 649(1):490–497, September 2006.

[124] H. Wang, W. Cao, C. Liu, Y. Xu, R. Liu, Z. Zeng, J. Chae, and H. Ji. Witnessing magnetic twist with high-resolution observation from the 1.6-m New Solar Telescope. *Nature Communications*, 6:7008, April 2015.

[125] H. Wang and C. Liu. Observational evidence of back-reaction on the solar surface associated with coronal magnetic restructuring in solar eruptions. *The Astrophysical Journal*, 716(2):L195–L199, June 2010.

[126] H. Wang, C. Liu, K. Ahn, Y. Xu, J. Jing, N. Deng, N. Huang, R. Liu, K. Kusano, G. D. Fleishman, D. E. Gary, and W. Cao. High-resolution observations of flare precursors in the low solar atmosphere. *Nature Astronomy*, 1(5):0085, 2017.

[127] H. Wang, J. Qiu, J. Jing, T. J. Spirock, V. Yurchyshyn, V. Abramenko, H. Ji, and P. R. Goode. Evidence of rapid flux emergence associated with the m8.7 flare on 2002 july 26. *The Astrophysical Journal*, 605(2):931–937, April 2004.

[128] H. Wang, T. J. Spirock, J. Qiu, H. Ji, V. Yurchyshyn, Y. Moon, C. Denker, and P. R. Goode. Rapid changes of magnetic fields associated with six x-class flares. *The Astrophysical Journal*, 576(1):497–504, September 2002.

[129] J. Wang, C. Liu, N. Deng, and H. Wang. Evolution of Photospheric Flow and Magnetic Fields Associated with the 2015 June 22 M6.5 Flare. *The Astrophysical Journal*, 853(2):143, February 2018.

[130] R. Wang, Y. D. Liu, Z. Yang, and H. Hu. Magnetic field restructuring associated with two successive solar eruptions. *The Astrophysical Journal*, 791(2):84, July 2014.

[131] S. Wang, C. Liu, R. Liu, N. Deng, Y. Liu, and H. Wang. Response of the photospheric magnetic field to the x2.2 flare on 2011 february 15. *The Astrophysical Journal*, 745(2):L17, January 2012.

[132] S. Wang, C. Liu, and H. Wang. The relationship between the sudden change of the lorentz force and the magnitude of associated flares. *The Astrophysical Journal*, 757(1):L5, August 2012.

[133] M. S. Wheatland, P. A. Sturrock, and G. Roumeliotis. An Optimization Approach to Reconstructing Force-free Fields. *The Astrophysical Journal*, 540(2):1150–1155, September 2000.

[134] R. J.; Schwartz R. A. White, S. M.; Thomas. Updated expressions for determining temperatures and emission measures from goes soft x-ray measurements. *Solar Physics*, 227:231–248, April 2005.

[135] T. Wiegelmann. Optimization code with weighting function for the reconstruction of coronal magnetic fields. *Solar Physics*, 219(1):87–108, 2004.

[136] T. Wiegelmann and B. Inhester. How to deal with measurement errors and lacking data in nonlinear force-free coronal magnetic field modelling? *Astronomy and Astrophysics*, 516:A107, June 2010.

[137] T. Wiegelmann, B. Inhester, and T. Sakurai. Preprocessing of vector magnetograph data for a nonlinear force-free magnetic field reconstruction. *Solar Physics*, 233(2):215–232, 2006.

[138] T. Wiegelmann, L. Yelles Chaouche, S. K. Solanki, and A. Lagg. Nonlinear force-free modelling: influence of inaccuracies in the measured magnetic vector. *Astronomy and Astrophysics*, 511:A4, February 2010.

[139] Y. Xu, W. Cao, K. Ahn, J. Jing, C. Liu, J. Chae, N. Huang, N. Deng, D. E. Gary, and H. Wang. Transient rotation of photospheric vector magnetic fields associated with a solar flare. *Nature Communications*, 9:46, January 2018.

[140] X. L. Yan, Z. K. Xue, G. M. Pan, J. C. Wang, Y. Y. Xiang, D. F. Kong, and L. H. Yang. The Formation and Magnetic Structures of Active-region Filaments Observed by NVST, SDO, and Hinode. *Astrophysical Journal Supplement Series*, 219:17, August 2015.

[141] S. Yang, J. Zhang, and R. Erdélyi. Enhancement of a Sunspot Light Wall with External Disturbances. *The Astrophysical Journal Letters*, 833(2):L18, December 2016.

[142] J. Zhang, H. Tian, S. K. Solanki, H. Wang, H. Peter, K. Ahn, Y. Xu, Y. Zhu, W. Cao, J. He, and L. Wang. Dark Structures in Sunspot Light Bridges. *The Astrophysical Journal*, 865(1):29, September 2018.

[143] I.V. Zimovets, M. Gros, and A.B. Struminsky. Evidence of the radio-quiet hard x-ray precursor of the 13 december 2006 solar flare. *Advances in Space Research*, 43(4):680 – 686, 2009. Solar Extreme Events: Fundamental Science and Applied Aspects.